LATTICE BOLTZMANN EQUATION SIMULATIONS OF TURBULENCE, MIXING, AND COMBUSTION

A Dissertation

by

HUIDAN YU

Submitted to the Office of Graduate Studies of
Texas A&M University
in partial fulfillment of the requirements for the degree of

DOCTOR OF PHILOSOPHY

December 2004

Major Subject: Aerospace Engineering

LATTICE BOLTZMANN EQUATION SIMULATIONS OF TURBULENCE, MIXING, AND COMBUSTION

A Dissertation

by

HUIDAN YU

Submitted to Texas A&M University
in partial fulfillment of the requirements
for the degree of

DOCTOR OF PHILOSOPHY

Approved as to style and content by:

Sharath S. Girimaji (Chair of Committee)	
Kalyan Annamalai (Member)	Paul Cizmas (Member)
Johnny Hurtado (Member)	Walter E. Haisler (Head of Department)

December 2004

Major Subject: Aerospace Engineering

ABSTRACT

Lattice Boltzmann Equation Simulations of Turbulence, Mixing, and Combustion.

(December 2004)

Huidan Yu, B.S., Zhejiang Normal University, P. R. China;

Ph.D., Peking University, P. R. China

Chair of Advisory Committee: Dr. Sharath S. Girimaji

We explore the capability of lattice Boltzmann equation (LBE) method for complex fluid flows involving turbulence, mixing, and reaction.

In the first study, LBE schemes for binary scalar mixing and multi-component reacting flow with reactions are developed. Simulations of initially non-premixed mixtures yield scalar probability distribution functions that are in good agreement with numerical data obtained from Navier-Stokes (NS) equation based computation. One-dimensional chemically-reacting flow simulation of a premixed mixture yields a flame speed that is consistent with experimentally determined value.

The second study involves direct numerical simulation (DNS) and large-eddy simulation (LES) of decaying homogenous isotropic turbulence (HIT) with and without frame rotation. Three categories of simulations are performed: (i) LBE-DNS in both inertial and rotating frames; (ii) LBE-LES in inertial frame; (iii) Comparison of the LBE-LES vs. NS-LES. The LBE-DNS results of the decay exponents for kinetic energy k and dissipation rate ε, and the low wave-number scaling of the energy spectrum agree well with established classical results. The LBE-DNS also captures rotating turbulence physics. The LBE-LES accurately captures low-wave number scaling, energy decay and large scale structures. The comparisons indicate that the

LBE-LES simulations preserve flow structures somewhat more accurately than the NS-LES counterpart.

In the third study, we numerically investigate the near-field mixing features in low aspect-ratio (AR) rectangular turbulent jets (RTJ) using the LBE method. We use D3Q19 multiple-relaxation-time (MRT) LBE incorporating a subgrid Smagorinsky model for LES. Simulations of four jets which characterized by AR, exit velocity, and Reynolds number are performed. The investigated near-field behaviors include: (1) Decay of mean streamwise velocity (MSV) and inverse MSV; (2) Spanwise and lateral profiles of MSV; (3) Half-velocity width development and MSV contours; and (4) Streamwise turbulence intensity distribution and spanwise profiles of streamwise turbulence intensity. The computations are compared against experimental data and the agreement is good. We capture both unique features of RTJ: the saddle-back spanwise profile of MSV and axis-switching of long axis from spanwise to lateral direction.

Overall, this work serves to establish the feasibility of the LBE method as a viable tool for computing mixing, combustion, and turbulence.

To my husband Jixiong Yu and our son Jack Yu

ACKNOWLEDGMENTS

I am eager to express my sincere and deep thanks and gratitude to Dr. Sharath S. Girimaji, my advisor and the chair of my Degree Advisory Committee, for providing me the opportunity to pursue this dissertation topic academically and financially. Many thanks to him for the guidance and encouragement both academically and personally through the years. This work would not have been possible without his constant nurturing with insight and wisdom.

I would like to sincerely thank Dr. Li-Shi Luo for providing technical expertise I needed to achieve my objectives. I take it as a treasure to have worked with him. His vision and direction is the strong technical support behind this work.

I would also like to thank my Committee members, Drs. Kalyan Annamalai, Paul Cizmas, and Johnny Hurtado for taking the time to work with me to fulfil all the requirements of the doctoral program.

I thank Drs. Lian-Ping Wang, Renwei Mei, Manfred Krafczyk, Jonas Tölke, and Daizhi Yu for their valuable discussions and their willingness to share useful references with me. I thank Dr. Jacques Richard and Professor Mengfen Xia for reviewing this dissertation and providing valuable comments. I also thank Drs. Rodney D. Bowersox, John C. Slattery, Walter E. Haisler, and Thomas W. Strganac for their care, advice, and help.

A special thank goes to Ms. Karen Knabe for her assistance. I also extend my thanks to the entire administrative staff of the Department of Aerospace Engineering which ensured my smooth stay at Texas A&M University. I am indeed grateful to my friends, Tau, Lin, Ravichandra (Ravi), and Steven for their help. Thanks also to my colleagues, Aditya, Joshua and Sunil for their help and support.

Finally, I would like to thank my family. First, to my parents, for giving me

life and endless love. Thanks to my sister and brother for their care and help. And most of all, special thanks to my husband Jixiong and our son Jack for their sacrifice, understanding, patience, encouragement, support, and love. For that, I am forever grateful.

This work is sponsored by the United States Air Force Office for Scientific Research (AFOSR) under Grant No. F49620-01-1-0142.

TABLE OF CONTENTS

CHAPTER Page

Page

LIST OF TABLES

LIST OF FIGURES

FIGURE Page

FIGURE Page

FIGURE Page

FIGURE Page

FIGURE Page

CHAPTER I

INTRODUCTION

Due to its fascinating complexity and ubiquitous presence in a variety of flows in nature and engineering, turbulence has attracted a great deal of attention over the last several decades. Examples include air-fuel mixing in engines of automobiles, aircrafts, and ships; the transport and dispersion of heat and pollutants in the atmosphere and the oceans. Turbulence also can cause undesirable consequences. For instance, it enhances energy consumption in pumping fluid through pipe lines, aircraft and ships, and automobiles; it distorts the propagation of electromagnetic signals; and so forth. A major goal of turbulence study is to predict the effects of turbulence and control them, suppress or enhance them depending on the circumstances, in various applications. Although turbulence is observed everywhere, it is hard to give a precise definition. As a matter of fact, turbulence is defined by its characteristics. Some of the important characteristics of turbulence are given as follows [1]:

- Irregularity or randomness: Turbulent motion appears chaotic. Turbulent flows become irregular even when initial and boundary conditions are very regular.
- Diffusivity: Turbulent flow enhances momentum, mass, and heat transfer and expedites mixing.
- High Reynolds number (Re): Turbulent flow occurs due to high inertia forces and relatively small viscous forces.
- Three dimensional vorticity fluctuations: Turbulent flows are characterized by high levels of vorticity and vortex stretching which is necessarily a 3D phe-

This dissertation follows the style and format of Computers & Fluids.

nomenon.

- Dissipation: Turbulence cannot sustain by itself. It needs continuous supply of energy.

- Continuum: Turbulence is not on molecular level but macroscopic level and the flow is governed by equations of fluid mechanics. In this study, we demonstrate that mesoscale description of turbulence is also very effective.

- Turbulent flows are flows: Turbulence is not a feature of the fluid but a fluid flow.

Because of these characteristics, turbulence has been regarded as a very challenging research subject. In fact, turbulence research has continuously expanded the horizons of modern fluid dynamics, mathematical theories, nonlinear physics, computation potentiality, fluid mechanical measurement techniques, and the like.

In any case, at sufficiently high Reynolds numbers, large-scale fluctuations produce finer and finer scales due to the nonlinear energy cascade process. Generally, in a developed turbulence the scale range of motion is of order $Re^{9/4}$ [2]. There are many interesting turbulent flows at $Re \sim 10^4 - 10^5$. In fact, most laboratory turbulence experiments fall within this range [3]. Hence, a typical turbulence contains order of $10^9 - 10^{10}$ scales of motion. Obviously, in such instances, it is practical to use statistic methods to describe turbulence and predict its consequences. A crucial challenge of turbulence study is the development of efficient computational tools.

A. Numerical computational tools to turbulence

Mathematically, the complex behavior of turbulence can be described with a fairly simple set of equations called Navier-Stokes (NS) equations. However, analytical

solutions of these equations are not easy to find even for the simplest turbulent flows since they are strongly influenced by boundary and initial conditions. Conventionally, a complete flow solution is a function of space and time and can only be obtained by numerically solving the NS equations. These numerical solutions are termed as direct numerical simulation (DNS) of the NS equations .

DNS (NS) resolves all the scales of the considered flow motion with given initial and boundary conditions. This entails solving the NS equations exactly without any modelling (see [4] for a review). As mentioned above, turbulence contains a very wide spectrum of scales: a typical turbulence in engineering applications with $Re = 10^5$ contains 10^{10} scales of motion. With increase of the Reynolds number, the size ratio of the largest to the smallest scales increases. The DNS approach was not feasible until the 1970s when computers of sufficient power became available. Conceptually, DNS is the most desirable approach because of its unrivalled simplicity and accuracy. However, its computational cost of both memory and speed requirements which are largely determined by the resolution requirements is extremely high [2]. For instance, a DNS of a flow past a complete airfoil would require a computer with exaflop (10^{18} flops[a]) [5] capacity to be practical, which is still not currently available. The instantaneous range of scales in turbulent flows increases rapidly with the Reynolds number and hence most practical engineering problems (e.g. flow around a car) have too wide a range scale to be directly computed using DNS. As a result, the applicability of the DNS approach is limited to flows of low or moderate Reynolds numbers.

For most high Reynolds number applications, approximate solutions like large-eddy simulation (LES) (see [6, 7] for reviews), Reynolds averaged Navier-Stokes (RANS) approaches (see [8] for a review) are more prevalent. LES only resolves those larger

[a]Short of *floating-point operations* per second, a common benchmark measurement for rating the speed of microprocessors

three-dimensional unsteady turbulent motions and the effects of the smaller-scale motions are filtered through modelling. While, in RANS, all the scales of motion are averaged such that only a mean velocity field and Reynolds stresses need to be solved. The Reynolds stresses introduced by the averaging process are determined by a turbulent closure model. In terms of computational expense, LES lies between RANS and DNS, and it is motivated by the limitations of each of these approaches. In other words, DNS can be thought of as the most desirable solution to a turbulent flow problem which is computationally most intensive, followed by LES which is less intensive and than RANS which is the least intensive (and also the crudest approximation).

B. Discrete (digital) fluid dynamics vs. continuum fluid dynamics

Conventionally, continuum fluid computation consists of three steps. The starting point is a set of nonlinear partial differential equations (PDEs), e.g. NS equations, which are obtained from physical laws such as mass conservation, momentum conservation and energy conservation. Then, these PDEs are discretized by various numerical schemes such as finite differences [9, 10], finite volume [11], finite elements [12, 13], or spectral methods [14, 15]. Finally, the resulting algebraic equations or systems of ordinary differential equations (ODEs) are solved by standard numerical methods. This process is usually referred to as computational fluid dynamics (CFD).

Although it seems straightforward and convenient to use the NS equations to most fluid problems, unfortunately, solving these equations can be very difficult or even impossible under some circumstances. An example is inhomogeneous multiphase or multi-component flows. In these flows, interfaces between different components or phases are dominated by thermodynamics effects due to molecular interactions. It is generally very hard to get a state equation at an interface although this

equation is required in order to solve the NS equations. Another instance is granular flow. It is even not clear whether or not there exists a set of PDEs analogous to the NS equations for a granular system. Apparently, continuum CFD approaches are not practical in these cases. Meanwhile, discretization from PDEs to ODEs not only introduces truncation error but also might destroy important conservation properties. Furthermore, numerical instability is always an important issue that requires careful consideration [16–18] in CFD approaches.

With the development of computational techniques, it is possible to formulate simple models for complex systems. The underlying idea of discrete or digital fluid dynamics (DFD) is the fact that fluid hydrodynamics is not sensitive to the underlying details in microscopic physics [19]. As a matter of fact, fluid hydrodynamics is the result of the collective behavior of numerous molecules in the system and the NS equations are merely macroscopic statements of conservation laws and constitutive relations. These conservation laws are the same as those in microscopic dynamics while the constitutive relations reflect the irreversible nature of the transport coefficients. Changes in molecular interactions can only affect the transport coefficients but do not alter the form of the macroscopic equations. As a result, it is possible to simulate the hydrodynamical behavior of fluids without accurately reproducing the details of the underlying microscopic or mesoscopic dynamics.

The computational philosophy of DFD approaches, lattice-gas automata (LGA) [20–22] or lattice Boltzmann equation (LBE) [23–25], is vastly different from continuum CFD approaches. Instead of macroscopic dynamic equations, DFD starts from a discrete mesoscopic equation, e.g. lattice Boltzmann equation. DFD is constructed from physics laws (mass, momentum, and energy conservation laws) plus necessary symmetry requirements [20]. It deals with the evolution of particle distribution functions. Interested macroscopic quantities such as density, momentum, and temperature

are computed from the moments of the distribution functions. DFD approaches are unconditionally stable (LGA) or show good stability properties (LBE). Meanwhile, these models only deal with simple arithmetic calculations so that no numerical error (as in LGA) or reduced numerical error (as in LBE) is introduced. The main source of error is the modelling error which is minimized by enforcing consistency conditions.

The important features that distinguish to DFD approaches from continuum CFD approaches are the following:

1. The viscous diffusion counterpart is a local relaxation process (collision operator) towards a local equilibrium state.

2. The linear convection operator recovers the nonlinear macroscopic advection through multi-scale expansions.

3. For incompressible flows, the particle distribution function is the only unknown variable to be determined. The pressure is calculated simply by a state equation.

4. Computation is purely local. The evolution of distribution functions depends only on their neighboring counterparts. Hence, the potential for parallelization is excellent.

The incompressible NS equations can be recovered in the nearly incompressible limit using Chapmann-Enskog technique [26]. There macroscopic quantities can be computed from the mesoscopic distribution functions via simple integration.

For applications to complex fluid systems such as turbulence, DFD is potentially a better hydrodynamic platform than CFD. The advantages lay both in improved physical accuracy and better computational characteristics. The main advantages of DFD are listed as follows:

1. LBE consists of simple arithmetic calculations, hence it is easy to program;

2. LBE is better suited for large-scale, especially, parallel computing;

3. LBE is ideally suited for handling multi-phase flow with phase transition and multi-species mixtures where diffusivity is important. CFD solvers can be computationally too expensive for these flows;

4. LBE can handle complex geometry with relative ease. Even computations with moving boundaries can be handled without loss of computational speed.

Over the last decade, LBE has experienced significant development and is currently a promising computational method with potential capability for simulating fluid flows with various physical features ([27–29] and references therein).

C. The objective of the dissertation

The objective of this dissertation is to apply DFD, i.e. LBE models, to compute turbulence, mixing and reaction. Our ultimate goal is to develop the LBE method as a reliable computational tool for turbulence and combustion simulations.

The focus areas of this dissertation are:

1. Scalar mixing, especially between species of different molecular weights.

2. Laminar reacting flow.

3. DNS and LES of decaying homogenous isotropic turbulence with and without frame rotation.

4. LES of turbulent flow issuing from low aspect-ratio rectangular jets at sufficiently high Reynolds numbers.

CHAPTER II

LATTICE BOLTZMANN METHOD

In this chapter, we first briefly introduce the kinetic theory. Specifically, we describe the fundamental ideas underlying the Boltzmann description of a fluid system: binary collision, the Boltzmann's H-theorem, the equilibrium distribution function, and the moments of the Boltzmann equation. Then, we introduce the lattice Boltzmann equation (LBE) models including single-relaxation-time (SRT) LBE model and multiple-relaxation-time (MRT) LBE model respectively. Finally, we present the numerical procedures for implementing SRT-LBE and MRT-LBE in implementation.

A. Introduction

It has been well established that a fluid can be described at three levels [20] . (i) Molecular Dynamics: It is based on Newtonian mechanics and deals with molecular positions and velocities. The system normally contains order of Avogadro's number of molecules. Molecular dynamics description involves tracking the trajectories which evolve according to Newton-Hamilton equation; (ii) Kinetic Theory: It is based on equilibrium and non-equilibrium statistical thermodynamics and deals with particle (mass) distribution functions, namely the density probability of finding a classical point-like particle (mass) at position $\vec{x}$ at time t with particle velocity $\vec{\xi}$. The classical kinetic equation is the celebrated Boltzmann equation; and (iii) Hydrodynamics: It is based on macroscopic physical conservation laws and deals with the continuum fluid behaviors through hydrodynamic variables such as density (ρ), velocity ($\vec{u}$), pressure (p), temperature (T), etc. The continuum variables result from the collective average over a large number of individual trajectories. This is the macroscopic level at which the fluid system is governed by continuity equation, Navier-Stoke (NS) equations, en-

ergy equation, etc. Kinetic theory plays as a bridge to relate the molecular properties to the transport coefficients in the continuum hydrodynamic level.

The Knudsen number, defined as $Kn = \lambda/L$, is a convenient measure for categorizing the flow regimes, see Fig. 1. Here, L is the characteristic dimension of the macroscopic flow and λ is the mean free path of the molecules. Continuum models based on NS equations and Euler equations are generally valid when $Kn < 0.01$, but can be extended into the slip-flow regime ($0.01 < Kn < 0.1$) by appropriate treatment of the wall boundary. While discrete particle model based on the Boltzmann equation governs almost all the flow regimes ($Kn < 100$). Without question, numerical approaches based on Boltzmann equation will be more fundamental and suitable for a wider range of practical applications.

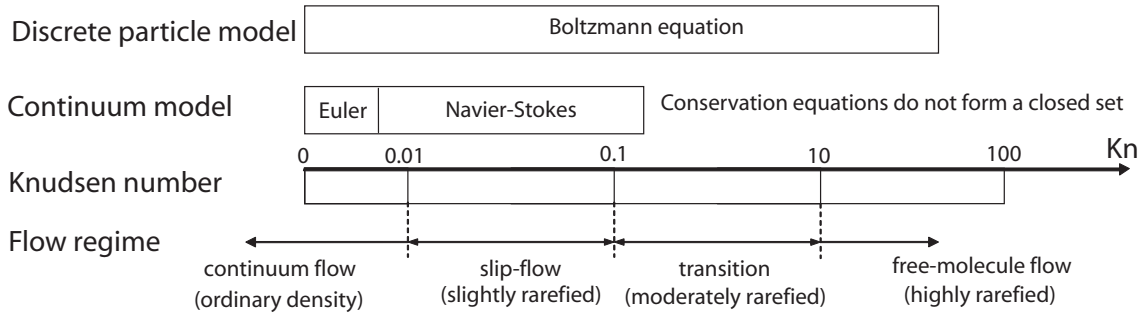

Fig. 1. Flow regimes in terms of Knudsen number and governing equations. Adapted from Anderson [30].

The remainder of this chapter is organized as follows: kinetic theory is briefly reviewed in Section B; Section C and D describe two lattice Boltzamm models, SRT-LBE and MRT-LBE, respectively; and Section E presents the numerical implementation of LBE models.

B. Background: Kinetic theory

On a macroscopic level, fluid is regarded as continuous and described with partial differential equations (PDEs) of hydrodynamics, e.g. NS equations. Nevertheless, at a microscopic level, it has been long known that fluid is indeed made of individual molecules and is amenable to be described by kinetic theory.

Kinetic theory is based on the following fundamental assumptions:

- The number of molecules is very large. Mean free-path of molecules is much larger than molecule size.
- Molecules move constantly and randomly with a distribution of velocities.
- Molecules undergo elastic collisions with other molecules and the walls, but otherwise exert no forces on each other.
- Molecules obey Newton's laws of motion.

Although the individual molecular motion obeys Newtonian mechanics, directly solving the fluid system is extremely difficult because of the large number of degrees of freedom which is in the order of the Avogadro's number (10^{23}). Fortunately such an approach is unnecessary. What one is really concerned with in most practical applications is the gross or bulk behaviors of the fluid which are represented by certain observable quantities such as density (ρ), velocity ($\vec{u}$), pressure (p), temperature (T), and so on. These macroscopic quantities are manifestations of the molecular motions averaged in space or time. In fact, the primary task of kinetic theory is to construct the relation between macroscopic quantities and molecular characteristics and explain macroscopic behaviors in terms of microscopic characteristics. Therefore, a statistical description of the system becomes imperative.

1. Boltzmann equation

Let x_i (or $\vec{x}$) be Cartesian coordinates of a physical space, and ξ_i (or $\vec{\xi}$) the molecular velocity. The crucial task of kinetic theory is the determination of the mass density distribution function $f(\vec{x}, \vec{\xi}, t)$ which represents the density weighted probability of finding a particle at position $\vec{x}$ at time t with particle velocity $\vec{\xi}$. Once the distribution function is known, the macroscopic variables, i.e. the density $\rho(\vec{x}, t)$, the momentum density $\vec{u}(\vec{x}, t)$, and the internal energy density $e(\vec{x}, t)$, the stress tensor $\sigma(\vec{x}, t)$, and the heat flux vector $\vec{q}(\vec{x}, t)$, are obtained by the following five moments of the mass density distribution function $f(\vec{x}, \vec{\xi}, t)$

$$\rho(\vec{x}, t) = \int f(\vec{x}, \vec{\xi}, t) d\vec{\xi}, \tag{2.1a}$$

$$\rho\vec{u}(\vec{x}, t) = \int \vec{\xi} f(\vec{x}, \vec{\xi}, t) d\vec{\xi}, \tag{2.1b}$$

$$\rho e(\vec{x}, t) = \frac{1}{2} \int \vec{\xi}_0^2 f(\vec{x}, \vec{\xi}, t) d\vec{\xi}, \tag{2.1c}$$

$$\sigma(\vec{x}, t) = -\int \vec{\xi}_0 \vec{\xi}_0 f(\vec{x}, \vec{\xi}, t) d\vec{\xi}, \tag{2.1d}$$

$$\vec{q}(\vec{x}, t) = \frac{1}{2} \int \vec{\xi}_0 (\vec{\xi}_0 \cdot \vec{\xi}_0) f(\vec{x}, \vec{\xi}, t) d\vec{\xi}, \tag{2.1e}$$

where $\vec{\xi}_0 = \vec{\xi} - \vec{u}$, the so-called peculiar velocity, is the particle velocity with respect to the macroscopic fluid flow velocity. It is important to note that $\vec{\xi}_0 \vec{\xi}_0 \neq \vec{\xi}_0 \cdot \vec{\xi}_0$. In deed, $\vec{\xi}_0 \vec{\xi}_0$ represents a second order tensor.

The principle of equipartition of energy gives the relation between temperature T and the energy density e as

$$e = \frac{D_0}{2} RT = \frac{D_0}{2m} k_B T \tag{2.2}$$

where D_0 is the degree of freedom of individual molecules and m is the mass of a single molecule. R is the ideal gas constant and k_B is the Boltzmann constant.

For monoatomic (single atom) molecules, $D_0 = 3$ since only translational degree of freedom is present. In what follows, we shall only consider monoatomic molecules.

The basic governing equation of kinetic theory is the evolution equation for the distribution function $f(\vec{x}, \vec{\xi}, t)$ in the presence of molecular collisions. This is the celebrated Boltzmann equation

$$\frac{\partial f}{\partial t} + \xi_i \frac{\partial f}{\partial x_i} = J(f) \tag{2.3}$$

where $J(f)$, a collision operator, models the rate of change of the distribution function f due to molecular collisions. We shall discuss the details of this operator shortly. If the collision is to conserve mass, momentum and energy, it is required that

$$\int d\vec{\xi} J(f) \begin{bmatrix} 1 \\ \vec{\xi} \\ \xi^2 \end{bmatrix} = 0 \tag{2.4}$$

2. Collision term and its property

Any solution of the Boltzmann equation (2.3) requires an expression of the collision operator $J(f)$. First, the following assumptions are invoked [31]

1. Only binary collisions between the constituent molecules are considered;
2. Collisions are local in the physical space;
3. The interaction of particles is of sufficiently short range.

Second, the medium is taken to be at the Boltzmann gas limit [31]

$$N \longrightarrow \infty \tag{2.5a}$$

$$m \longrightarrow 0 \tag{2.5b}$$

$$\vartheta \longrightarrow 0 \tag{2.5c}$$

$$N\sigma^2 = constant \tag{2.5d}$$

$$Nm = constant \tag{2.5e}$$

where N, m, and ϑ are the total number of constituent molecules, the molecular weight, and a parameter which characterizes the range of the inter-particle forces. Then, the form of the collision function $J(f)$ can be obtained as [32]

$$J(f) = \frac{1}{m}\int dSd\vec{\xi}_1|\vec{\xi}_1 - \vec{\xi}|(f'f_1' - ff_1) \tag{2.6}$$

with dS the collision cross section. f', f_1', f, and f_1 are defined as $f' \equiv f(\vec{x}, \vec{\xi}', t)$, $f_1' \equiv f(\vec{x}, \vec{\xi}_1', t)$, $f \equiv f(\vec{x}, \vec{\xi}, t)$, and $f \equiv f(\vec{x}, \vec{\xi}_1, t)$ respectively. $\vec{\xi}'$ and $\vec{\xi}_1'$ are the molecular velocities before a binary collision. After collision, the velocities become $\vec{\xi}$ and $\vec{\xi}_1$. $\vec{\xi}'$ and $\vec{\xi}_1'$ are related to $\vec{\xi}$ and $\vec{\xi}_1$ by momentum and energy conservation constraints.

The collision term has an important symmetry property which can be shown as follows [31]. Consider another representation of the collision term in Eq. (2.6)

$$\int d\vec{\xi}J(f)\psi(\vec{\xi}) = \frac{1}{m}\int dSd\vec{\xi}_1 d\vec{\xi}|\vec{\xi}_1 - \vec{\xi}|(f'f_1' - ff_1)\psi(\vec{\xi}) \tag{2.7}$$

where $\psi(\vec{\xi})$ is any arbitrary function of $\vec{\xi}$. It is obvious that a simple interchange of $\vec{\xi}$ and $\vec{\xi}_1$ doesn't change the value of the integral on the right-hand side of Eq. (2.7), such that

$$\int d\vec{\xi}J(f)\psi(\vec{\xi}) = \frac{1}{m}\int dSd\vec{\xi}_1 d\vec{\xi}|\vec{\xi}_1 - \vec{\xi}|(f'f_1' - ff_1)\psi(\vec{\xi}_1) \tag{2.8}$$

Further, replacing the dummy variables $\vec{\xi}$, $\vec{\xi}_1$ by $\vec{\xi}'$, $\vec{\xi}_1'$, tedious geometrical analysis of the binary collision process leads to a transformation of the dependent variables $\vec{\xi}'$, $\vec{\xi}_1'$ to $\vec{\xi}$, $\vec{\xi}_1$ and gives the following alternate form for this integral (for details see

Harris [31])

$$\begin{aligned}\int d\vec{\xi} J(f)\psi(\vec{\xi}) &= -\frac{1}{m}\int dS d\vec{\xi}_1' d\vec{\xi}' |\vec{\xi}_1' - \vec{\xi}'|(f'f_1' - ff_1)\psi(\vec{\xi}') \\ &= -\frac{1}{m}\int dS d\vec{\xi}_1 d\vec{\xi} |\vec{\xi}_1 - \vec{\xi}|(f'f_1' - ff_1)\psi(\vec{\xi}') \end{aligned} \tag{2.9}$$

Similarly,

$$\int d\vec{\xi} J(f)\psi(\vec{\xi}) = -\frac{1}{m}\int dS d\vec{\xi}_1 d\vec{\xi} |\vec{\xi}_1 - \vec{\xi}|(f'f_1' - ff_1)\psi(\vec{\xi}_1') \tag{2.10}$$

Combining Eqs. (2.7) - (2.10) to get, finally,

$$\begin{aligned}\int d\vec{\xi} J(f)\psi(\vec{\xi}) &= \frac{1}{4m}\int dS d\vec{\xi}_1 d\vec{\xi} |\vec{\xi}_1 - \vec{\xi}|(f'f_1' - ff_1)[\psi(\vec{\xi}) + \psi(\vec{\xi}_1) - \psi(\vec{\xi}') - \psi(\vec{\xi}_1')] \\ &= \frac{1}{4}\int d\vec{\xi}_1 d\vec{\xi} J(f)[\psi(\vec{\xi}) + \psi(\vec{\xi}_1) - \psi(\vec{\xi}') - \psi(\vec{\xi}_1')] \end{aligned} \tag{2.11}$$

Rewriting Eq. (2.4) according to Eq. (2.11),

$$\int d\vec{\xi} J(f) \begin{bmatrix} 1 \\ \vec{\xi} \\ \xi^2 \end{bmatrix} = \frac{1}{4}\int d\vec{\xi} J(f) \begin{bmatrix} 1+1-1-1 \\ \vec{\xi} + \vec{\xi}_1 - \vec{\xi}' - \vec{\xi}_1' \\ \xi^2 + {\xi_1}^2 - {\xi'}^2 - {\xi_1'}^2 \end{bmatrix} = 0 \tag{2.12}$$

where equality with zero reflects the consequence of the conservation of mass, momentum, and energy, respectively. In a binary collision, this means that if $\psi(\vec{\xi})$ is taken to be 1, $\vec{\xi}$, and ξ^2 corresponding to mass density, momentum, and energy density, the change in ψ for both molecules must be zero. For this reason, $\psi = 1$, $\vec{\xi}$, and ξ^2 are frequently called the elementary collision invariants. The most general form for any collision invariant is a linear combination of these five collision invariants which we will use later.

3. H–theorem and equilibrium

Any isolated system, after a long period of time, should reach an equilibrium state. This can be seen [26, 33] by considering the H function

$$H(\vec{x},t) = \int f \ln f d\vec{\xi} \tag{2.13}$$

Differentiating Eq. (2.13) with respect to time we get

$$\frac{\partial H}{\partial t} = \int (1+\ln f)\frac{\partial f}{\partial t} d\vec{\xi} \tag{2.14}$$

If we only consider a spatially uniform system, i.e., f depends on t only, the above equation can be written as

$$\frac{\partial H}{\partial t} = \int (1+\ln f) J(f) d\vec{\xi} \tag{2.15}$$

which can be further written as

$$\frac{\partial H}{\partial t} = \frac{1}{4m}\int dS d\vec{\xi} d\vec{\xi_1} |\vec{\xi_1} - \vec{\xi}| (f'f_1' - ff_1) \ln(\frac{ff_1}{f'f_1'}) \tag{2.16}$$

with the combination of the Boltzmann equation and the collision operator. Since $(f'f_1' - ff_1)\ln(ff_1/f'f_1') \leq 0$ and all the other terms in the above equation are positive, as a result,

$$\frac{\partial H}{\partial t} \leq 0 \tag{2.17}$$

This means that the H function can never increase as time goes and is known as Boltzmann's H–theorem. The H–theorem for a nonuniform system can be found in Harris [31].

The equality in Eq. (2.17) corresponds to the equilibrium state characterized by

$$ff_1 = f'f_1' \tag{2.18}$$

This condition can be expressed equivalently as

$$\ln f + \ln f_1 = \ln f' + \ln f_1' \tag{2.19}$$

The above description of the equilibrium state indicates that lnf in this state is a collisional invariant, so that

$$\ln f_M(\vec{\xi}) = A + \vec{B} \cdot \vec{\xi} + C\xi^2 \tag{2.20}$$

The five constants A, B_1, B_2, B_3, and C above are not arbitrary, since we have an equal number constraints relating the first five moments of f given in Eqs. (2.1). The resulting unique value of f obtained for the equilibrium state is

$$f_M(\vec{\xi}) = \frac{\rho}{(2\pi RT)^{3/2}} e^{-(\vec{\xi}-\vec{u})^2/2RT} \tag{2.21}$$

This equilibrium distribution function is well known as Maxwell-Boltzmann distribution function.

4. Moments of the Boltzmann equation

Starting from Eqs. (2.1) and using Eq. (2.4), we can derive the zeroth, the first, and the second moment equations by integrating Eq. (2.3) with respect to velocity $\vec{\xi}$. The integration results in the conservations of mass, momentum, and energy respectively.

It is important to note the fact that $\vec{x}$, $\vec{\xi}$, and t are independent variables. Hence $\vec{\xi}$ commutes with the operate ∇ and $\partial/\partial t$. However both $\vec{\xi_0}$ and $\vec{u}$ have no such commutation property.

- The zeroth order moment of the Boltzmann equation (Eq. (2.3))

$$\frac{\partial}{\partial t} \int f d\vec{\xi} + \nabla \cdot \int \vec{\xi} f d\vec{\xi} = \int J(f) d\vec{\xi} = 0, \tag{2.22}$$

which leads

$$\frac{\partial \rho}{\partial t} + \nabla \cdot (\rho \vec{u}) = 0. \tag{2.23}$$

- The first order moment of the Boltzmann equation (Eq. (2.3))

$$\frac{\partial}{\partial t} \int \vec{\xi} f d\vec{\xi} + \nabla \cdot \int \vec{\xi}\vec{\xi} f d\vec{\xi} = \int \vec{\xi} J(f) d\vec{\xi} = 0, \tag{2.24}$$

It should be reiterated that $\vec{\xi}\vec{\xi}$ represents a second order tensor. Since $\int \vec{\xi}_0 f d\vec{\xi} = 0$, the second term of the left-hand side can be written as

$$\nabla \cdot \int (\vec{\xi}_0 + \vec{u})(\vec{\xi}_0 + \vec{u}) f d\vec{\xi} = \nabla \cdot [(\rho \vec{u}\vec{u}) + \int \vec{\xi}_0 \vec{\xi}_0 f d\vec{\xi}] \tag{2.25}$$

Substitute the second term back and use Eq. (2.23) to obtain

$$\frac{\partial \vec{u}}{\partial t} = -(\vec{u} \cdot \nabla)\vec{u} - \frac{1}{\rho} \nabla \cdot \int \vec{\xi}_0 \vec{\xi}_0 f d\vec{\xi}. \tag{2.26}$$

- The second order moment of the Boltzmann equation (Eq. (2.3))

$$\frac{1}{2} \frac{\partial}{\partial t} \int \xi^2 f d\vec{\xi} + \frac{1}{2} \nabla \cdot \int \xi^2 \vec{\xi} f d\vec{\xi} = \frac{1}{2} \int \xi^2 J(f) d\vec{\xi} = 0 \tag{2.27}$$

The first term on the left-hand side of the above equation yields

$$\frac{\partial}{\partial t} (\frac{1}{2} \int (\vec{\xi}_0 + \vec{u})^2 f d\vec{\xi}) = \frac{\partial}{\partial t} [\int (\xi^2 + + u^2) f d\vec{\xi}] = \frac{\partial}{\partial t} (\frac{1}{2} \rho u^2 + \rho \varepsilon) \tag{2.28}$$

while the second term yields

$$\nabla \cdot \frac{1}{2} \int (\vec{\xi}_0 + \vec{u})^2 (\vec{\xi}_0 + \vec{u}) f d\vec{\xi} = \nabla \cdot [\rho \vec{u} (\frac{1}{2} u^2 + \varepsilon) + \vec{u} \cdot \int \vec{\xi}_0 \vec{\xi}_0 f d\vec{\xi} + \frac{1}{2} \int \vec{\xi}_0 \xi_0^2 d\vec{\xi}] \tag{2.29}$$

Hence we get

$$\frac{\partial \varepsilon}{\partial t} = -\vec{u} \cdot \nabla \varepsilon - \frac{1}{\rho} [\nabla \cdot (\vec{u} \cdot \int \vec{\xi}_0 \vec{\xi}_0 f d\vec{\xi}) - \vec{u} \cdot (\nabla \cdot \int \vec{\xi}_0 \vec{\xi}_0 f d\vec{\xi})] - \frac{1}{\rho} \int \frac{1}{2} \xi_0^2 \vec{\xi}_0 f d\vec{\xi}. \tag{2.30}$$

Therefore, by substituting $\varepsilon = 3RT/2$ we get the macroscopic dynamic equations

corresponding mass, momentum and temperature

$$\frac{\partial \rho}{\partial t} + \nabla \cdot (\rho \vec{u}) = 0, \tag{2.31}$$

$$\frac{\partial \vec{u}}{\partial t} + (\vec{u} \cdot \nabla)\vec{u} = -\frac{1}{\rho}\nabla \cdot \sigma, \tag{2.32}$$

$$\frac{\partial T}{\partial t} + (\vec{u} \cdot \nabla)T = \frac{2}{3R\rho}[\nabla \cdot (\vec{u} \cdot \sigma) - \vec{u} \cdot (\nabla \cdot \sigma)] - \frac{2}{3R\rho}\nabla \cdot \vec{q}. \tag{2.33}$$

where σ and $\vec{q}$ are stress tensor and heat flux vector defined by Eqs.(2.1).

The study of flow with kinetic theory is largely concerned with attempts to solve the Boltzmann equation. However, even though the molecular interaction has been simplified as binary collision, exact solutions of the Boltzmann equation are rare because of its nonlinearity and integro-differential form. However, we have already seen how it is possible, without solving the Boltzmann equation, to obtain significant information from it such as the symmetry property of collision term, H-theorem, equilibrium distribution function, the moments of the distribution function etc. There are several outstanding names associated with the effort to solve the Boltzmann equation: Boltzmann, Maxwell, Hillbert, Chapman, Enskog, and Grad (see Harris [31]). In this dissertation, we are not going to cover the details about these approaches. Instead, we shall briefly introduce the lattice Boltzmann method.

C. The single-relaxation-time lattice Boltzmann model

Historically, the lattice Boltzmann BGK (LB-BGK) equation [24, 25] evolved empirically from Boolean approaches such as the lattice gas automata (LGA) [20, 21]. The LB-BGK equation was devised to overcome some serious deficiencies of LGA such as large statistical noise, limited range of physical parameters, non-Galilean invariance, and implementation difficulty in three dimensions. Recently, it has been shown that the LB-BGK equation can be derived from the continuous Boltzmann BGK equation

via discretization in both time and phase space. Details are presented by He & Luo [34, 35].

The simple single-relaxation-time (SRT) model used in kinetic theory is usually referred to as the BGK model, after Bhatnager, Gross, and Krook, who introduced the model in a paper published in 1954 [36]. In this model, the collision term $J(f)$ in the Boltzmann equation is simplified as

$$J(f) = -\mathcal{Z}(f - f_M) \tag{2.34}$$

Here the Maxwellian distribution function f_M is expressed in terms of the local mean velocity and temperature. $\mathcal{Z}$ is the mean collision frequency that may depend on temperature but not on molecular velocity. Therefore the Boltzmann equation becomes

$$\frac{\partial f}{\partial t} + \xi_i \frac{\partial f}{\partial x_i} = -\mathcal{Z}(f - f_M). \tag{2.35}$$

Eq. (2.35) is usually referred to Boltzmann BGK equation.

Integration of Eq. (2.35) along characteristics followed by Taylor series expansion to the first order in time leads to

$$f(\vec{x} + \vec{\xi}\delta_t, \vec{\xi}, t + \delta_t) - f(\vec{x}, \vec{\xi}, t) = \frac{1}{\tau}[f(\vec{x}, \vec{\xi}, t) - f_M(\vec{x}, \vec{\xi}, t)], \tag{2.36}$$

where $\tau = 1/(\mathcal{Z}\delta_t)$ is the dimensionless mean relaxation time and δt is the discretized time interval. Further discretization in phase space, followed by appropriate approximation of the equilibrium distribution and low Mach number assumption leads to the SRT-LBE form for isothermal incompressible flow

$$f_\alpha(\vec{x} + \vec{e}_\alpha\delta_t, t + \delta_t) - f_\alpha(\vec{x}, \vec{e}_\alpha, t) = \frac{1}{\tau}[f_\alpha(\vec{x}, \vec{e}_\alpha, t) - f_\alpha^{(eq)}(\vec{x}, \vec{e}_\alpha, t)] \tag{2.37}$$

where $f_\alpha^{(eq)}$ is the discretized equilibrium distribution function and $\{\vec{e}_\alpha\}$ is the discrete

velocity set, both are lattice model based. We shall present the details of $\{\vec{e}_\alpha\}$, $\{f_\alpha^{(eq)}\}$ for D2Q9 SRT-LBE in Chapter 3 and D3Q19 SRT-LBE in chapter 4 respectively. The fluid density and flow momentum are moments of the distribution given by

$$\rho = \sum_\alpha f_\alpha = \sum_\alpha f_\alpha^{(eq)}, \qquad \rho\vec{u} = \sum_\alpha \vec{e}_\alpha f_\alpha = \sum_\alpha \vec{e}_\alpha f_\alpha^{(eq)} \tag{2.38}$$

The hydrodynamic equations can be derived from Eq. (2.37) by means of the Chapman-Enskog analysis (multiple scale expansion) [26].

Although it has been pointed out in Chapter I that the Boltzmann equation is almost valid for all flow regimes ($Kn < 100$), LB-BGK equation which uses the BGK approximation [36] is only valid for small Knudsen number, say $Kn \sim 0.1$, due to the discretization of space and time and the low-Mach number expansion of the Maxwell-Boltzmann distribution function [34, 35]. However, it is possible to extend LBE to larger Kn by appropriate treatment of the collision operation.

D. The multiple-relaxation-time lattice Boltzmann model

As it has been shown in Section C, the SRT-LBE is indeed a special finite difference form of the Boltzmann BGK equation. The most drastic approximation made in the derivation of the SRT-LBE is the discretization of momentum space $\vec{\xi}$ into a very small set of discrete velocities $\{\vec{\xi}_\alpha | \alpha = 1, \ldots, b\}$ [34, 35]. The discretization of phase space and time inevitably introduces truncation error and numerical artifacts. It is highly desirable to reduce the effect of the artifacts.

Very recently, a new LBE model called the multiple-relaxation-time (MRT) LBE, also referred to as the generalized lattice Boltzmann equation, has emerged. In fact, the idea of MRT-LBE [37] was presented at the same time as SRT-LBE [24, 25] but was not utilized for practical problems until recently [38–40]. Like SRT-LBE, the

formulation of MRT-LBE is lattice based. We shall present a detail MRT-LBE model in Chapter V. Here, we only introduce the basic idea of MRT-LBE.

In the MRT model, different moments of the distribution function relax at different rates. On the contrary, in SRT model, all moments (hydrodynamic and higher order) relax at the same rate.

In general, MRT-LBE model has the same basic components as SRT-LBE model which are

- A discrete velocity (or phase) space defined by a regular $\mathcal{D}$-dimension lattice together with a set of discrete velocities $\{\vec{e}_\alpha|\alpha = 0, 1, \ldots, b\}$ connecting each lattice site to all or some of its neighbors. b is the number of discrete directions;
- A set of mass distribution functions $\{f_\alpha|\alpha = 0, 1, \ldots, b\}$ defined in the velocity space;
- An evolution equation of the mass distribution functions.

The difference is that in MRT model an equal number of moments $\{m_\beta|\beta = 0, 1, \ldots, b\}$ of the distribution functions f_α are constructed. The collision is executed in the moment space to achieve different moments relax at different rates. The velocity space $\mathbb{V}$ spanned by $\{f_\alpha|\alpha = 0, 1, \ldots, b\}$ and the moment space $\mathbb{M}$ spanned by $\{m_\beta|\beta = 0, 1, \ldots, b\}$ are transferred through a linear mapping M: $|m\rangle = M|f\rangle$ and $|f\rangle = M^{-1}|m\rangle$. The evolution equation of the MRT-LBE is [38, 39]

$$|f(\vec{x} + \vec{e}_\alpha\delta t, t + \delta t)\rangle - |f(\vec{x}, t)\rangle = -M^{-1}\hat{S}[|m(\vec{x}, t)\rangle - |m^{(eq)}(\vec{x}, t)\rangle], \tag{2.39}$$

where the Dirac notation of ket $|\cdot\rangle$ represents a column vector, e.g.

$$|f(\vec{x} + \vec{e}_\alpha\delta_t, t + \delta_t)\rangle \equiv [f_0(\vec{x} + \vec{e}_\alpha\delta_t, t + \delta_t), \ldots, f_b(\vec{x} + \vec{e}_\alpha\delta_t, t + \delta_t)]^T,$$

with the superscript T the transpose operator and δt the discrete time interval. $\hat{S}$ is the diagonal collision matrix determining different relaxation rates for different moments and $|m^{(eq)}\rangle$ is the equilibria of $|m\rangle$.

The construction of the transformation matrix M, the moments $|m\rangle$ and their equilibria $|m^{(eq)}\rangle$, and the diagonal collision matrix $\hat{S}$ are lattice based. The MRT-LBE model details for three popular lattice models – D2Q9, D3Q15, and D3Q19 are given by Lallemand & Luo [39, 40] respectively. In Chapter V, we will describe the details of a D3Q19 MRT-LBE model for large eddy simulation.

E. Implementation of LBE models

Numerical solving LBE is indeed simple and straightforward. The implementation of both SRT-LBE and MRT-LBE consists of two computational steps:

- collision

$$\tilde{f}_\alpha(\vec{x},t) = f_\alpha(\vec{x},t) + \Omega_\alpha(\vec{x},t) \qquad \alpha = 0,\ldots,b,$$

for SRT-LBE: $\Omega_\alpha(\vec{x},t) = -[f_\alpha(\vec{x},t) - f_\alpha^{(eq)}(\vec{x},t)]/\tau,$

for MRT-LBE: $\Omega_\alpha(\vec{x},t) = -M^{-1}\hat{S}[|m(\vec{x},t)\rangle - |m^{(eq)}(\vec{x},t)\rangle]$

- streaming

$$f_\alpha(\vec{x}+\vec{e}_\alpha\delta_t, t+\delta_t) = \tilde{f}_\alpha(\vec{x},t), \qquad \alpha = 1,\ldots,b$$

The computational flowchart is shown in Fig. 2.

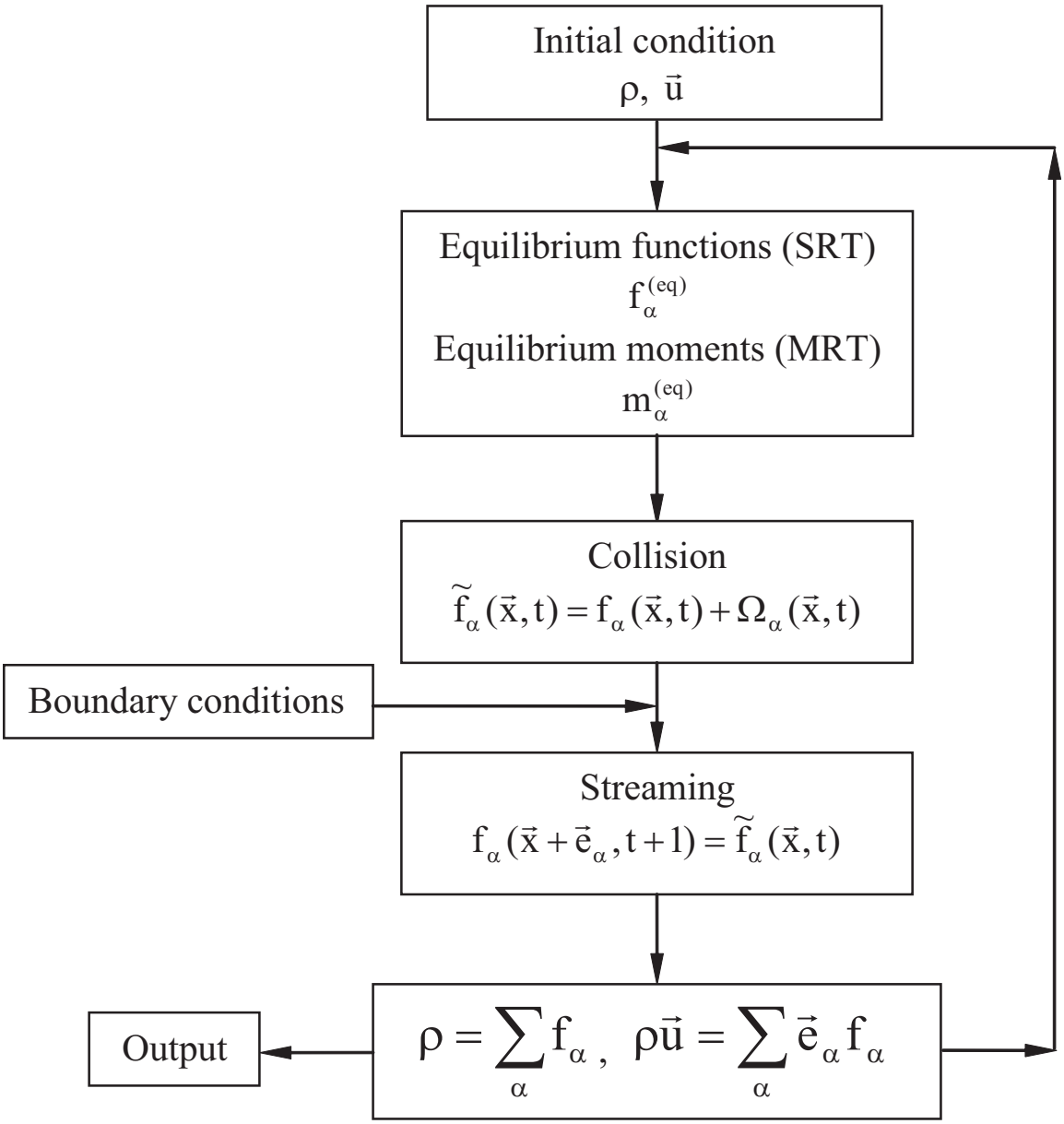

Fig. 2. Computational flowchart for LBE models.

CHAPTER III

SCALAR MIXING AND CHEMICAL REACTION SIMULATIONS USING LATTICE BOLTZMANN METHOD*

A. Introduction

The lattice Boltzmann equation (LBE) model has been emerging as a physically accurate and computationally viable tool for simulating laminar and turbulent flows [23, 34, 35, 42–45]. On the theoretical front, rigorous mathematical proof now exists demonstrating that LBM is a special finite difference scheme of the Boltzmann equation that governs all fluid flows [34, 35]. (Recall that the NS equation also has its basis in the Boltzmann equation.) It has also been shown that LBM can be related to some conventional computational fluid dynamics methods and the proof brings to light the advantages of the LBM [46, 47]. Detailed numerical studies with the LBM demonstrate the physical accuracy and computational viability for solving complex fluid flow problems [27, 28, 42, 43].

With few notable exceptions [48–54], the LBM has been so far used mostly for single-component, inert and isothermal flows. In this work, we simulate scalar mixing in a multi-component flow and a chemical reacting flow using the lattice Boltzmann computational approach. At the continuum level, the mixing example considered appears as a pure diffusion problem without any advection velocities. However, at the mesoscopic level, each of the components is associated with non-zero velocities. Hence, the problem considered is truly more significant than simple passive scalar mixing. Due to the kinetic nature of the LBE scheme, the extension of this method

to cases with non-trivial macroscopic velocity field is straight forward. The second problem considered is one-dimensional flame propagation in a well-stirred homogeneous mixture of propane and air. The flame speed calculated using the LBM is in good agreement with experimental data. This problem is very similar to the one solved by Yamamoto [55] but with a sightly different physical field.

The remainder of this chapter is organized as follows. In Section B, the lattice Boltzmann equations used in the mixing and reacting simulations are presented. The results from both simulations are presented in Section C. We conclude in Section D with a brief discussion. The derivation of hydrodynamic equations and mutual diffusivity for the binary scalar mixing model is presented in Appendix A. Details of the physical parameters used in the reacting flow simulation are given in Appendix B.

B. Lattice Boltzmann equations

1. Lattice Boltzmann equations for binary scalar mixing

For the sake of simplicity without losing generality, we adopt D2Q9 lattice model, as shown in Fig. 3, with the discrete particle velocities $\vec{e}_\alpha$ and the weighting factor ω_α $(\alpha = 0, 1, \ldots, 8)$

$$\vec{e}_\alpha = \begin{cases} (0,0), & \alpha = 0 \\ (\cos[(\alpha-1)\pi/2], \sin[(\alpha-1)\pi/2]), & \alpha = 1,2,3,4 \\ (\cos[(\alpha-5)\pi/2+\pi/4], \sin[(\alpha-5)\pi/2+\pi/4]), & \alpha = 5,6,7,8 \end{cases} \tag{3.1}$$

and

$$w_\alpha = \begin{cases} 4/9, & \alpha = 0 \\ 1/9, & \alpha = 1,2,3,4 \\ 1/36, & \alpha = 5,6,7,8 \end{cases} \tag{3.2}$$

respectively. The sound speed is $c_s = 1/\sqrt{3}(\delta_x/\delta_t)$ with δ_x being the lattice constant of the underlying square lattice and δt time interval respectively. Normally $\delta_x/\delta_t = 1$ meaning $\delta_x = \delta_t$.

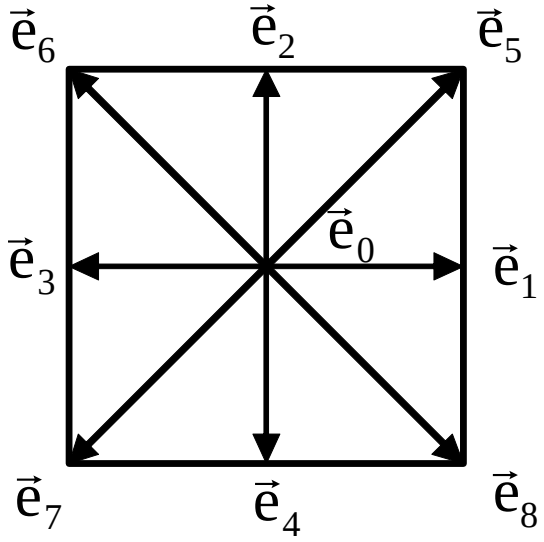

Fig. 3. FHP-9bit model: 9 discrete velocities on a square lattice.

Consider a multi-species field: n_α^σ denotes the number density distribution function of a particular species σ with discrete velocity $\vec{e}_\alpha$, $\alpha = 0, 1, \cdots, 8$. The number density and molecular weight of species σ are given respectively by n^σ and m^σ. Then mass density of the σ-species is given as

$$\rho^\sigma = m^\sigma n^\sigma \tag{3.3}$$

Number density, mass density and velocity of the mixture are computed by

$$n = \sum_\sigma n^\sigma \tag{3.4}$$

$$\rho = \sum_\sigma \rho^\sigma \tag{3.5}$$

and

$$\vec{u} = \frac{1}{\rho}\sum_{\sigma}(m^{\sigma}\sum_{\alpha} n_{\alpha}^{\sigma}\vec{e}_{\alpha}) \tag{3.6}$$

respectively.

Let σ and σ' denote the two species of interest. The LBE for each species is

$$n_{\alpha}^{\sigma}(\vec{x}+\vec{e}_{\alpha}, t+1) = n_{\alpha}^{\sigma}(\vec{x}, t) + \Omega_{\alpha}^{\sigma}(\vec{x}, t) \tag{3.7}$$

where the collision operator

$$\Omega_{\alpha}^{\sigma} = -\frac{1}{\tau^{\sigma}}[n_{\alpha}^{\sigma} - n_{\alpha}^{\sigma(eq)}] + \frac{J_{\alpha}^{\sigma\sigma'}}{m^{\sigma}} \tag{3.8}$$

includes an additional term $J_{\alpha}^{\sigma\sigma'}$ which reflects the interaction between two species.

We use the following number density equilibrium distribution function

$$n_{\alpha}^{\sigma(eq)} = w_{\alpha} n^{\sigma}[1 + 3(\vec{e}_{\alpha}\cdot\vec{u}') + \frac{9}{2}(\vec{e}_{\alpha}\cdot\vec{u}')^2 - \frac{1}{2}u'^2] \tag{3.9}$$

with

$$\vec{u}' = \frac{1}{\rho}\sum_{\sigma}\frac{m^{\sigma}}{\tau^{\sigma}}(n^{\sigma}\vec{u}^{\sigma}) \tag{3.10}$$

The binary interaction term is modelled as

$$J_{\alpha}^{\sigma\sigma'} = G_f n_{\alpha}^{(eq)}(\vec{e}_{\alpha} - \vec{u})\cdot[\nabla x^{\sigma} + (x^{\sigma} - \omega^{\sigma})\frac{\nabla\rho}{\rho}] = -J_{\alpha}^{\sigma'\sigma} \tag{3.11}$$

where G_f is a parameter reflecting mutual interaction strength between two species. x^{σ} and ω^{σ} are molar and mass fractions of the species σ

$$x^{\sigma} = \frac{n^{\sigma}}{n}, \quad \omega^{\sigma} = \frac{\rho^{\sigma}}{\rho}$$

and

$$n_{\alpha}^{(eq)} = w_{\alpha} n[1 + 3(\vec{e}_{\alpha}\cdot\vec{u}) + \frac{9}{2}(\vec{e}_{\alpha}\cdot\vec{u})^2 - \frac{1}{2}u^2] \tag{3.12}$$

The diffusion coefficient of this mixing model in the case that two species have

equal molecular weight m and equal relaxation time τ can be derived (see Appendix A)

$$D = -c_s^2 \rho(\tau n G_f - \tau + \frac{1}{2}) \tag{3.13}$$

2. Lattice Boltzmann equations for reacting flow

Here we consider simple one-dimensional flame propagation through a premixed mixture of propane and air. The problem studied is identical to that of Yamamoto [55] but the physical combustion field is sightly different. The simplifying assumptions invoked in this study are now listed:

- No external forces in the field and the flow is incompressible.
- The chemical reaction (heat release) does not affect the flow field; temperature and concentration fields are decoupled and solved separately.
- Nitrogen is inert.
- The transport properties are constants (not functions of temperature).
- Viscous energy dissipation and radiative heat losses are negligible.
- Simple one step reaction is considered

  $$C_3H_8 + 5O_2 \Rightarrow 3CO_2 + 4H_2O$$

  and the over-all reaction rate is given by

  $$\omega_{ov} = \kappa_{ov} C_{C_3H_8} C_{O_2} e^{-E/RT}$$

  where $C_{C_3H_8}$, C_{O_2}, κ_{ov} and E are concentrations of fuel propane and oxygen, reaction coefficient and effective activation energy respectively.

In a reacting flow, the state of the fluid at any given point in space and time can be completely specified in terms of fluid velocity, composition vector (either in terms of mass fraction or concentration) and temperature. We will need to develop the LBE for all these variables. For generating a background flow, the conventional LBM substeps of collision (relaxation) and streaming (convection) are used. However for the temperature and concentration fields, there is an extra substep between collision and streaming substeps to account for the reaction. This is identical to the time-splitting approach used in continuum methods for chemically reacting flows.

a. Flow field

The background flow-field is obtained using the following stencil for partial pressure

$$p_\alpha(\vec{x}+\vec{e}_\alpha, t+1) = p_\alpha(\vec{x}, t) - \frac{1}{\tau_p}[p_\alpha(\vec{x}, t) - p_\alpha^{(eq)}(\vec{x}, t)] \tag{3.14}$$

where

$$p_\alpha^{(eq)} = w_\alpha p[1 + 3(\vec{e}_\alpha \cdot \vec{u}) + \frac{9}{2}(\vec{e}_\alpha \cdot \vec{u})^2 - \frac{3}{2}u^2] \tag{3.15}$$

The total pressure p $(= \rho c_s^2)$ and the fluid velocity are calculated using

$$p = \sum_\alpha p_\alpha$$

$$\vec{u} = \frac{1}{p}\sum_\alpha \vec{e}_\alpha p_\alpha$$

This is the velocity used for determining the equilibrium distribution functions in temperature and concentration fields.

b. Temperature and concentration fields

For temperature (T is normalized by $T_c = E/R$) and concentration (mass ratio $Y^i, i = C_3H_8, O_2, CO_2$ and H_2O) fields, there is an extra computational substep, reaction,

besides conventional computational substeps of collision and advection.

- COLLISION

$$\tilde{T}_\alpha(\vec{x},t) = T_\alpha(\vec{x},t) - \frac{1}{\tau_T}[T_\alpha(\vec{x},t) - T_\alpha^{(eq)}(\vec{x},t)] \tag{3.16}$$

$$\tilde{Y}_\alpha^i(\vec{x},t) = Y_\alpha^i(\vec{x},t) - \frac{1}{\tau_{Y^i}}[Y_\alpha^i(\vec{x},t) - Y_\alpha^{i(eq)}(\vec{x},t)] \tag{3.17}$$

where

$$T_\alpha^{(eq)} = w_\alpha T[1 + 3(\vec{e}_\alpha \cdot \vec{u}) + \frac{9}{2}(\vec{e}_\alpha \cdot \vec{u})^2 - \frac{3}{2}u^2] \tag{3.18}$$

$$Y_\alpha^{i(eq)} = w_\alpha Y^i[1 + 3(\vec{e}_\alpha \cdot \vec{u}) + \frac{9}{2}(\vec{e}_\alpha \cdot \vec{u})^2 - \frac{3}{2}u^2] \tag{3.19}$$

and

$$T = \sum_\alpha T_\alpha, \qquad Y^i = \sum_\alpha Y_\alpha^i$$

Relaxation time-constant τ_T is determined by thermal diffusivity and τ_{Y^i}'s are determined by the diffusivity of corresponding species.

- REACTION

Reaction equation

$$C_3H_8 + 5O_2 \rightarrow 3CO_2 + 4H_2O$$

$$\omega_{ov} = \kappa_{ov}\tilde{C}_{C_3H_8}\tilde{C}_{O_2}e^{-1/\tilde{T}}$$

Concentrations

$$\tilde{C}_i = \rho\tilde{Y}_i/M_i$$

Reaction terms

$$Q_{Y^i} = \lambda_i\frac{M_i}{\rho}\omega_{ov}$$

$$Q_T = \frac{Q}{\rho c_p T_c}\omega_{ov}$$

where

$$\tilde{Y}^i = \sum_\alpha \tilde{Y}^i_\alpha, \quad \tilde{T} = \sum_\alpha \tilde{T}_\alpha$$

In the above equations, the stoichiometric coefficients (λ's) for the various species are: $\lambda_{C_3H_8} = -1$, $\lambda_{O_2} = -5$, $\lambda_{CO_2} = 3$, $\lambda_{H_2O} = 4$ and all physical parameters are listed in Appendix B.

- STREAMING

$$T_\alpha(\vec{x} + \vec{e}_\alpha, t+1) = \tilde{T}_\alpha(\vec{x}, t) + w_\alpha Q_T$$

$$Y^i_\alpha(\vec{x} + \vec{e}_\alpha, t+1) = \tilde{Y}^i_\alpha(\vec{x}, t) + w_\alpha Q_{Y^i}$$

C. Simulations

As mentioned above, the primary objective of this work is to investigate the ability of the LBM to simulate scalar mixing, chemical reaction. Working towards this end, we perform simulations of two unit problems: one to establish the mixing characteristics and another to demonstrate the chemical reaction scheme.

1. Non-premixed binary scalar mixing

This problem epitomizes the scalar mixing issues encountered in a typical non-premixed combustion application. Two species (presumably fuel and oxidizer) are initially segregated and randomly distributed in the computational domain which in the present case is a square box. Mesh size is set 500×500. The two species are generically labelled as black and white. A typical initial distribution is shown in Fig. 4. The macroscopic velocity is set everywhere to zero corresponding to a pure diffusion problem. It should be reiterated here that the mesoscopic velocities are non-zero. At each time step, particles stream along eight direction with the velocities given by Eq. (3.1). The initial values for the number densities are $n^b = 1.0$, $n^w = 0.0$ in region of

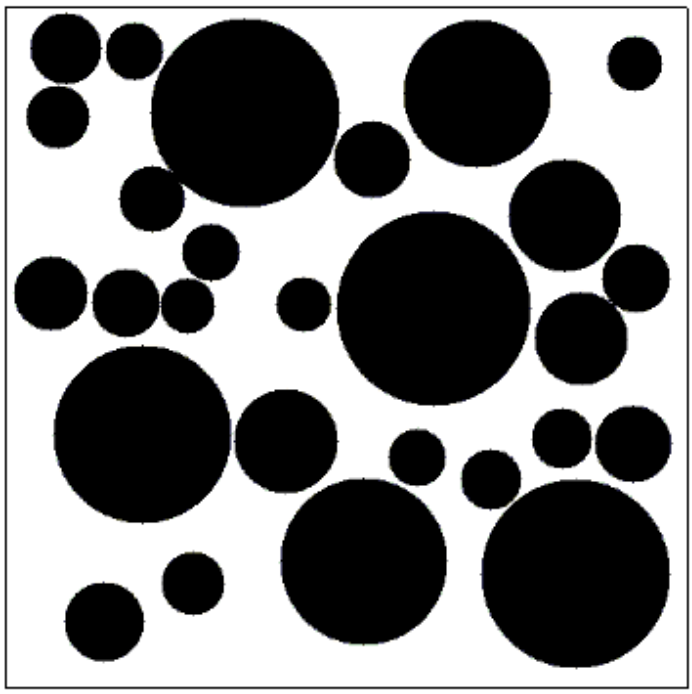

Fig. 4. Initial number density distribution for both equal and unequal mass cases.

the black species and $n^w = 1.0$, $n^b = 0.0$ in region of white species. Simulations are performed for sets: $\tau^b = \tau^w = 1.0$ and $G_f = 1/30.0$. Citing homogeneity of the scalar field, periodic boundary conditions are used in all directions.

To discretize ∇x^σ and $\nabla \rho$ in the binary interaction term in Eq. (3.11), we use central difference operator. Taylor series expansion of each of $f(\vec{x} + \vec{e}_\alpha)$ terms to the second order leads the following stencil of ∂_{x_1} and ∂_{x_2}:

$$\partial_{x_1} = \frac{1}{12}\begin{bmatrix} -1 & 0 & 1 \\ -4 & 0 & 4 \\ -1 & 0 & 1 \end{bmatrix}, \quad \partial_{x_2} = \frac{1}{12}\begin{bmatrix} 1 & 4 & 1 \\ 0 & 0 & 0 \\ -1 & -4 & -1 \end{bmatrix} \tag{3.20}$$

That is

$$\partial_{x_1} f(\vec{x}) \approx \frac{1}{12}[4f(\vec{x}+\vec{e}_1)+f(\vec{x}+\vec{e}_5)+f(\vec{x}+\vec{e}_8)-f(\vec{x}+\vec{e}_6)-4f(\vec{x}+\vec{e}_3)-f(\vec{x}+\vec{e}_7)] \quad (3.21)$$

$$\partial_{x_2} f(\vec{x}) \approx \frac{1}{12}[4f(\vec{x}+\vec{e}_2)+f(\vec{x}+\vec{e}_5)+f(\vec{x}+\vec{e}_6)-f(\vec{x}+\vec{e}_7)-4f(\vec{x}+\vec{e}_4)-f(\vec{x}+\vec{e}_8)] \quad (3.22)$$

in which f can be x^σ and ρ^σ.

We first compute the mutual diffusivity in a binary mixture by studying the decay of a sinusoidal concentration wave with small amplitude. The simulation was carried out on a (128×3) rectangular domain. Initially, assume both species have the same particle density $n^b = n^w = 0.5$ at each grid in the whole field. Introduce a perturbation particle density wave $\widetilde{n}(x) = Asin(\lambda x)$ with $\lambda = 2\pi/128$ and $A = 0.01$ into the particle density of black species, i.e. $n^b(x,0) = 0.5 + \widetilde{n}(x)$. From the diffusion equation

$$\frac{\partial n^b}{\partial t} = D\frac{\partial^2 n^b}{\partial x^2} \quad (3.23)$$

we have an analytical solution expressed as $n^b(x,t) = n^b(x,0)exp(-D\lambda^2 t)$. The mutual diffusivity is obtained by numerically measuring the decay rate of n^b

$$D = -\frac{\ln n^b(x,t) - \ln n^b(x,0)}{\lambda^2 t} \quad (3.24)$$

where x is an arbitrary grid picked in the computational domain. The results of the computation of Eq. (3.24) are plotted in Fig. 5 along with the analytical predictions from Eq. (3.13) for comparison. Two different τ values are used. Fig. 5 shows that numerical computations (bullets) are in excellent agreement with the analytical predictions (lines).

The lattice Boltzmann methodology permits simulation of mixing between species of equal or unequal number and mass densities with equal facility. However, in continuum based methods, mixing between species of unequal mass densities is not straight-

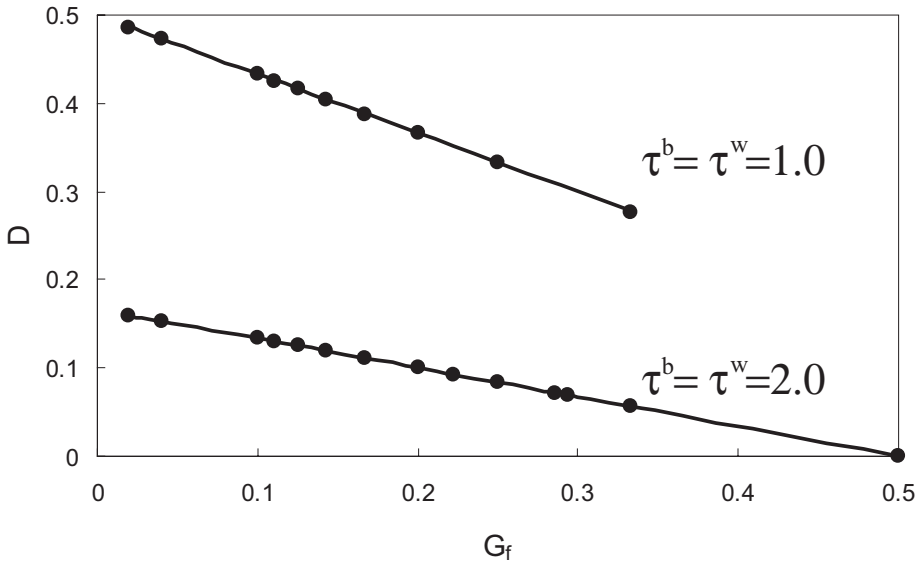

Fig. 5. Mutual diffusivity D of binary mixture as a function of the interaction strength G_f. Lines: analytical prediction; Bullets: numerical computation.

forward. This represents a fundamental advantage of the LBM over continuum-based methods.

a. Equal mass case ($m^b = m^w = 1.0$)

The first case studied is mixing of two fluids of equal molecular weight and number density, hence of equal mass density. This case is interesting as the results can be directly compared with direct numerical simulation (DNS) of NS equation data of Eswaran and Pope [56]. In this case, the number density and mass density are equivalent since the molecular weight of the two species are identical. Fig. 6 (a) shows the time evolution of the probability density function (pdf) of scalar $\overline{\rho}$:

$$\overline{\rho} = \frac{\rho^b - \rho^w}{\rho^b + \rho^w}$$

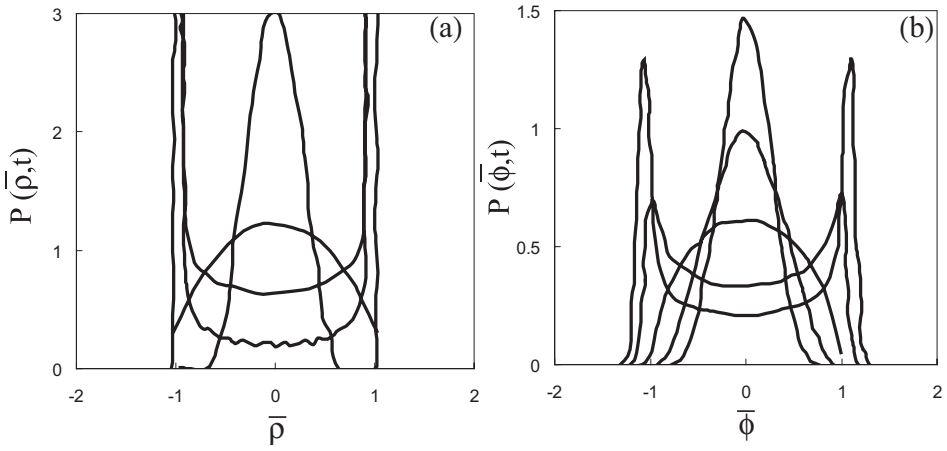

Fig. 6. Pdf evolution of number density in equal mass case. (a) LBE simulation; (b) DNS of NS computation from Eswaran and Pope [56].

The corresponding DNS data [56] is shown in Fig. 6 (b). The LBE and DNS data show excellent qualitative agreement. In particular, the change of the pdf shape from the initial double-delta shape through a nearly uniform distribution to, finally, a Gaussian-like distribution is well captured by the LBE results. It deserves to mention here that many other mixing models do not, even qualitatively, capture the form of pdf during evolution.

In Fig. 7, the time evolution of the root-mean-square (rms) of scalar fluctuations (ρ') obtained from LBE is compared with that from DNS [56]:

$$\rho' = \sqrt{< (\rho^b - < \rho^b >)^2 >} \tag{3.25}$$

where $< \cdots >$ implies volume-averaged value. The relaxation time-constant has been chosen to yield the best agreement. For the optimal time-constant, the agreement is again excellent. It suffices to say that given the right time-constant, the LBE captures the DNS behavior well, qualitatively and quantitatively.

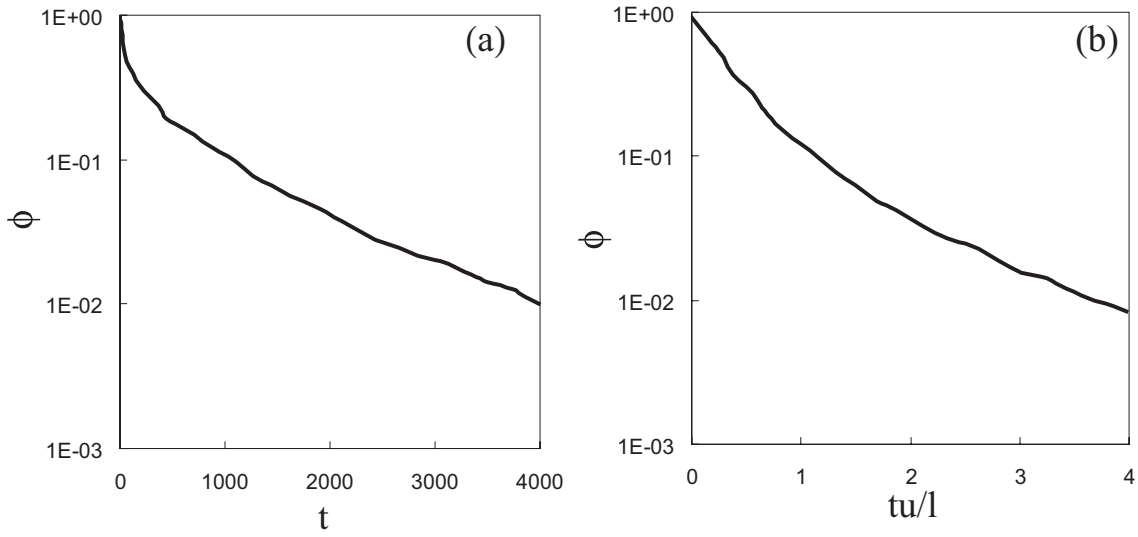

Fig. 7. Evolution of rms scalar (ϕ) in equal mass case. (a) LBE ($\phi = 2\rho'$) simulation; (b) DNS of NS computation from Eswaran and Pope [56].

b. Unequal mass case ($m^b = 2.0, m^w = 1.0$)

The unequal mass case is particularly interesting since it represents a more practical problem, mixing between species of unequal mass densities. In this case, the initial distribution of black and white species is similar to the equal mass case. Thus the average number density of black and white species are identical. However, the molecular weight of the black species is twice that of the white species. Hence, the macroscopic mass density of the black species is twice that of the white species. The precise definition of the mass density used here is

$$\overline{\rho^\sigma} = \frac{\rho^\sigma - \rho^{\sigma'}}{\rho^\sigma + \rho^{\sigma'}} = \frac{m^\sigma n^\sigma - m^{\sigma'} n^{\sigma'}}{m^\sigma n^\sigma + m^{\sigma'} n^{\sigma'}}$$

and the particle number density is

$$\overline{n^\sigma} = \frac{n^\sigma - n^{\sigma'}}{n^\sigma + n^{\sigma'}}$$

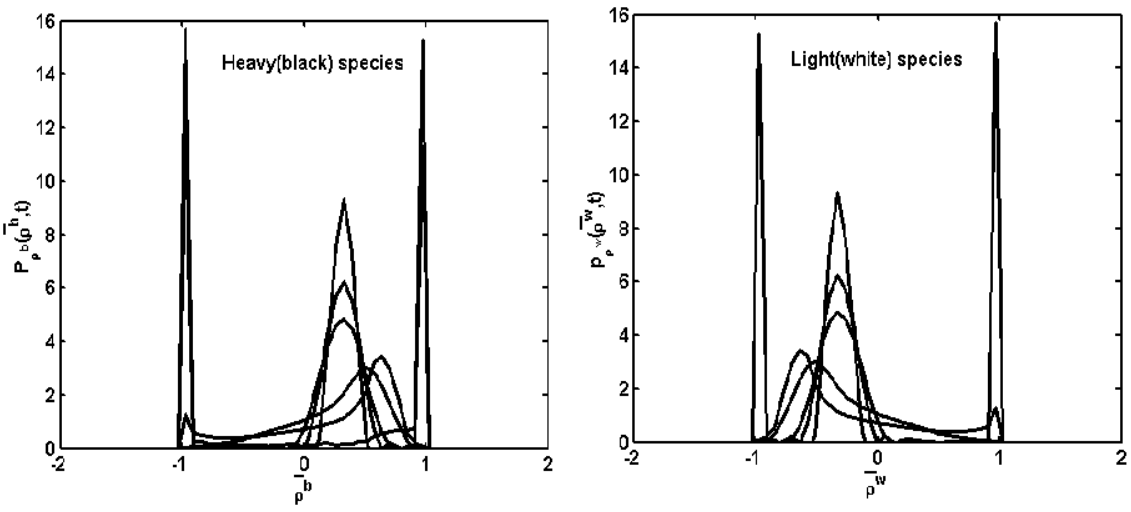

Fig. 8. Pdf evolution of mass density in unequal mass case ($m^b : m^w = 2 : 1$).

In the unequal molecular weight case, mass density and number density are two independent entities. The evolution of both these quantities are investigated. In Fig. 8, the mass density evolution is given for both species. The mass density goes from an initial double-delta shape to a Gaussian-like shape centered around the global average of the respective density. The final pdf shape for each species is clearly not symmetric. This is easily understood since the overall average density of the black species is twice that of the white species.

In Fig. 9, the number density evolution is shown. Since the average number density is identical for both species, the final pdf distribution is symmetric about the mean value for each species. However, the intermediate forms of the pdf are quite nonsymmetric, demonstrating that the mixing process in this case is quite different from the equal-mass case even if the final distributions are similar. A detailed study of the physics of mixing between species of unequal mass-densities will be undertaken later.

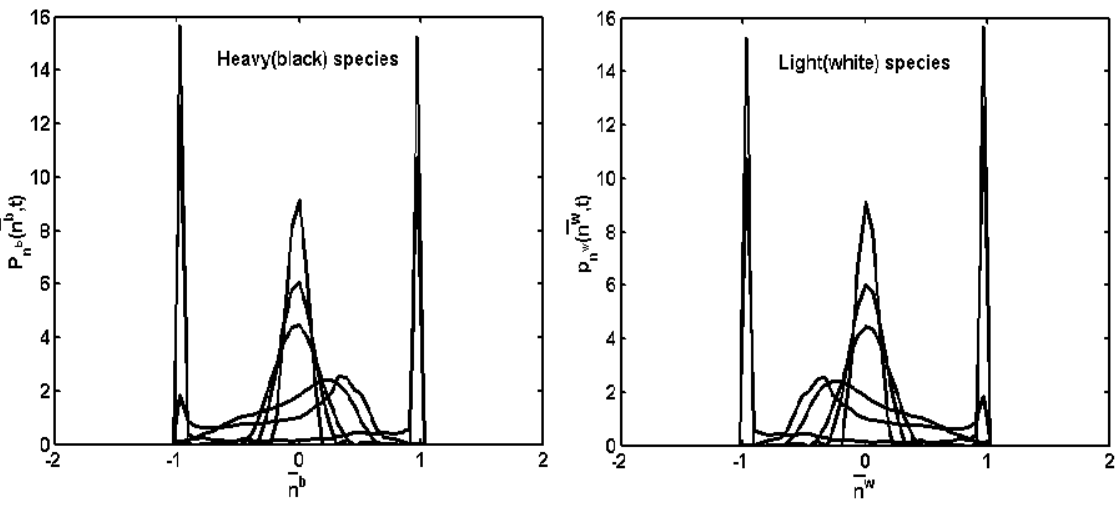

Fig. 9. Pdf evolution of number density in unequal mass case ($m^b : m^w = 2 : 1$).

2. Reacting flow in a 1-d channel

In this example, we study the ability of LBM to simulate chemical reaction. The simplest non-trivial case when reaction can be studied without the complicating effects of mixing is the case of 1-D flame propagation through a homogeneous premixed mixture.

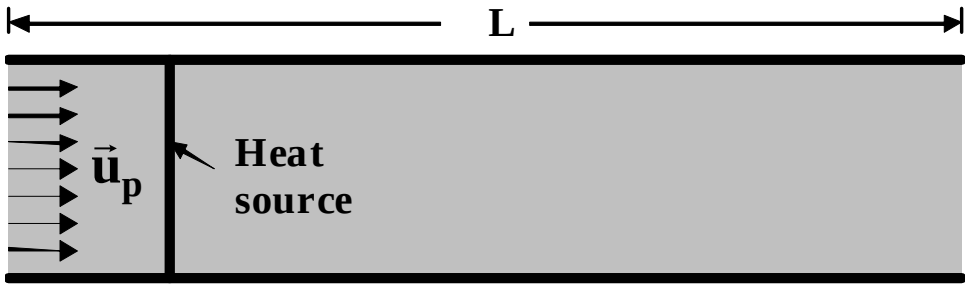

Fig. 10. A schematic illustration of a simple 1-D reacting flow.

Schematic of the flow simulated is shown in Fig. 10. For this simple case, the background flow generated from Eq. (3.14) maintains both the pressure and velocity fields uniform in space and time. A heat source is placed at a location close to the inlet to ignite the mixture. Once ignition is achieved, the heat source is removed. At subsequent times the flame propagates to the right. Initial conditions are set as following: The values of pressure and velocity are set at $p = 1$, $u_x = u_{in} = 0.1$, $u_y = 0.0$. Both fields are maintained uniform at all times in this simple case. The temperature is set at $T = 300^0K$ everywhere except at $x = 50$ where a heat source is placed with $T_{source} = 1500^0K$ to ignite the mixture. The hot spot is removed after the mixture ignites. The mass ratio of nitrogen is $Y_{N_2} = 0.7375$. The well-premixed mixture consists of propane and oxygen with the mass ratios of $Y_{C_3H_8} = 0.2252$, $Y_{O_2} = 0.0373$. The mass fractions of the products are initially set to zero: $Y_{CO_2} = Y_{H_2O} = 0.0$. All physical parameters used in this simulation are given in Appendix B.

Periodic boundary conditions are used at the top and bottom boundaries and the fully developed boundary condition is applied at the outlet. At the inlet, the initial conditions are maintained.

In Fig. 11, the flame position is shown as a function of time. The flame location is identified as the position with the highest reaction rate at any given time. The linear variation of flame location with time (in Fig. 11) indicates that the flame propagates at a nearly constant rate. This flame speed can be easily estimated from knowing the flame position at initial ($t_i = 0$; $x_{fl} = 50$) and final ($t_f = 4000$; $x_{fl} = 406$) times. The flame speed thus calculated is

$$v_f = \frac{x_{fl}(t_f) - x_{fl}(t_i)}{t_f - t_i} = \frac{406 - 50}{4000 - 0} = 0.0089$$

in lattice units. Knowing the flame speed, the burning velocity can be easily deter-

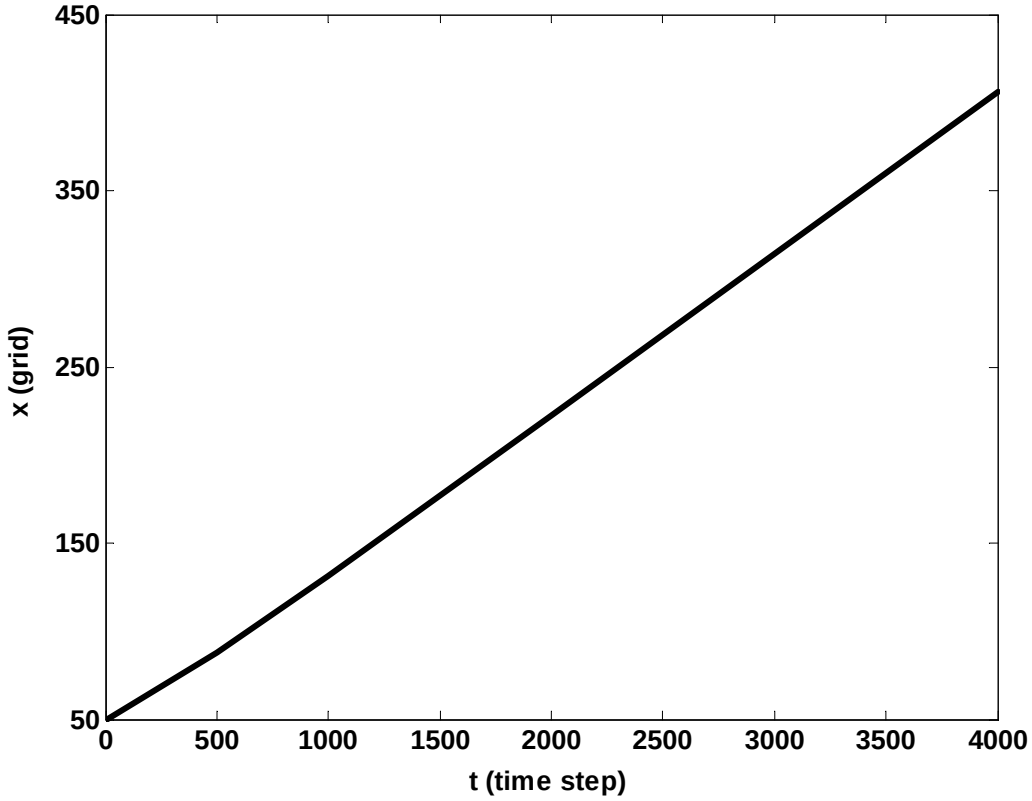

Fig. 11. The flame position evolution with time.

mined:

$$S_L = u_{in} - v_f$$

In the above, u_{in} is the reactant velocity at the inlet (which is maintained uniform throughout the flow-field). The burning velocity thus obtained will be in lattice units. This can be converted into metric units as follows:

$$S_L = \frac{u_{in} - v_f}{u_{in}} \cdot u_p \tag{3.26}$$

The resulting burning velocity is $S_L = 0.11 m/s$ which compares extremely well with

the value obtained from experiments for a propane-air flame [57].

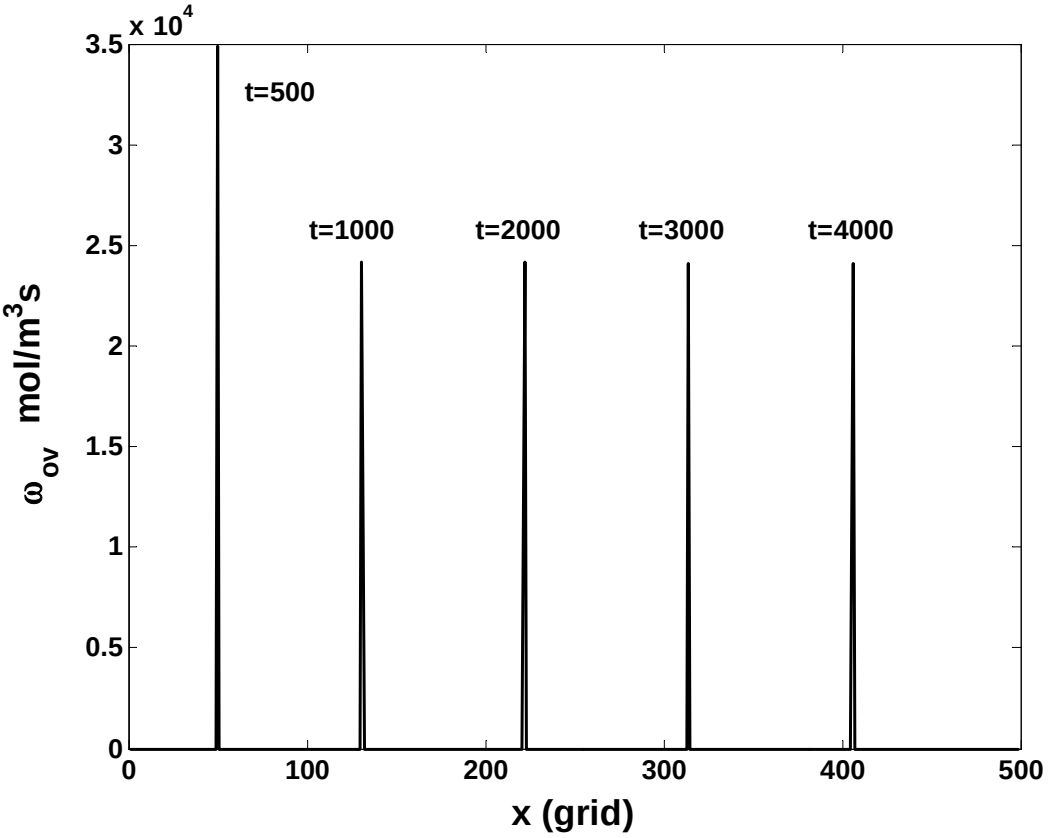

Fig. 12. Reaction rate profiles at different times.

Fig. 12 shows that the reaction rate profile in the reaction zone as time evolves. Simulations indicate that flame behavior is sensitive to the magnitude of the heat source.

D. Conclusions

We have simulated scalar mixing and chemical reacting flows using LBM. In the case of equal-density species mixing, well known results from continuum Naiver-stokes

simulation are reproduced. The true advantage of the LBM can be seen from the mixing simulations of species of different molecular weights. The results appear quite encouraging. Such simulations are very difficult with continuum based methods. The premixed reacting flow simulations also produce results that are in good agreement with known data. Based on these simulations, we conclude that LBM can perform adequately for more complicated turbulent combustion simulations.

CHAPTER IV

DNS AND LES OF DECAYING HOMOGENOUS ISOTROPIC TURBULENCE WITH AND WITHOUT FRAME ROTATION

A. Introduction

The lattice Boltzmann method (LBM) [23–25] is rapidly emerging as a physically sound and computationally efficient method for simulating fluid flow. The lattice Boltzmann equation is based on the Boltzmann equation instead of the Navier-Stokes (NS) equations and, in principle, is more general than continuum approaches. By simplifying the underlying microscopic physics so that only key elements (the local conservation laws and related symmetries) needed to guarantee accurate macroscopic behaviors are retained, a computational advantage over traditional methods can be achieved [27–29, 43]. Consequently, the LBM has found applications in many areas of flow physics, such as free-surface flows [58], the Rayleigh-Taylor instability between two fluids [59], multicomponent fluids through porous media [60], viscoelastic fluids [61, 62], particulate and colloidal suspensions in fluid [63–65], and other complex systems (cf. [27–29] and references therein).

In an effort to evaluate the capability of the LBM in turbulence, we perform DNS and LES of decaying homogenous isotopic turbulence in both inertial and rotating frames of reference. Decaying HIT is an important benchmark problem in the field of DNS and LES of turbulence. In fact, the first attempt at DNS with incompressible NS equation involved this problem [66]. Since then several numerical investigations of decaying HIT have been carried out, including some recent NS studies on decay exponents and low wave-number spectral scaling [67–70]. Some preliminary studies of three-dimensional (3D) decaying HIT using LBE have also been performed [71–

73], but these investigations stop well short of quantitative comparisons with the well established classical results.

The objective of this work is to perform a comprehensive investigation of decaying HIT with LBE-DNS and LBE-LES to establish the suitability of the LBM for turbulence applications. For this purpose, we perform three type of simulations. (a) LBE-DNS of decaying HIT in inertial and rotating frame of reference. The decay exponent for the kinetic energy k and the dissipation rate ε are computed and compared with corresponding NS-DNS results. The low wave-number scalings of the energy spectrum are studied. The effect of rotation on the kinetic energy decay is investigated. (b) LBE-LES of decaying HIT in inertial frame of reference. We compute kinetic energy decay, energy spectrum and flow structures using LBE-LES. By comparing LBE-LES results with the corresponding LBE-DNS results, we observe that LBE-LES accurately captures large scale flow behavior. We find that the optimal Smagorinsky constant value for LBE-LES is smaller than the traditional value used in NS-LES approaches. (c) LBE-LES vs. NS-LES. We carry out a comparative study of the LBE-LES and NS-LES of decaying HIT. We show that the LBE-LES simulations preserve flow structures more accurately than the NS-LES counterpart. This is due to the fact that some history/non-local effects are inherent in the LBE subgrid closure.

The remainder of this chapter is organized as follows. Section B briefly reviews relevant background on decaying HIT. Section C gives a concise introduction to the LBM equations for DNS and LES. We present our results in Section D and conclude in Section E.

B. Homogeneous isotropic turbulence

The energy spectrum $\hat{E}(\kappa, t)$ in decaying HIT evolves as

$$\partial_t \hat{E}(\kappa, t) = -\hat{T}(\kappa, t) - 2\nu\kappa^2 \hat{E}(\kappa, t), \tag{4.1}$$

where κ is the wave-number and ν is the kinematic viscosity, and $\hat{T}(\kappa, t)$ represents the nonlinear energy transfer between modes (cf. Eq. (6.162) in Pope [2]). The kinetic energy k and dissipation rate ε of turbulence are given, respectively, by

$$k = \int \hat{E}(\kappa) d\kappa, \qquad \text{and} \qquad \varepsilon = 2\nu \int \kappa^2 \hat{E}(\kappa) d\kappa.$$

It has been long observed that, after a short initial transient period of time, the kinetic energy k and dissipation rate ε exhibit power-law decay [2]

$$\frac{k(t)}{k_0} \sim \left(\frac{t}{t_0}\right)^n, \quad \frac{\varepsilon(t)}{\varepsilon_0} \sim \left(\frac{t}{t_0}\right)^{-(n+1)}, \tag{4.2}$$

where k_0 and ε_0 are the values of k and ε at the reference time $t_0 = nk_0/\varepsilon_0$. Isotropic turbulence is typically characterized by the Taylor-microscale Reynolds number

$$\mathrm{Re}_\lambda = \frac{u_{\mathrm{rms}}\lambda}{\nu} = \sqrt{\frac{20}{3\nu\varepsilon}}\, k, \tag{4.3}$$

where $\lambda = \sqrt{15\nu u_{\mathrm{rms}}^2/\varepsilon}$ is the transverse Taylor-microscale length and $u_{\mathrm{rms}} = \sqrt{2k/3}$ is the root mean square (rms) of the velocity field $\vec{u}$.

Equation (4.1) admits a continuous class of invariant solutions in the limit of $\mathrm{Re} \to \infty$ [74]. At the large Re, $\hat{E}(\kappa, t)$ at the low wave-number behaves as $\lim_{\kappa\to 0} \hat{E}(\kappa) \sim \kappa^\sigma$, where σ is a time-independent constant (e.g. [75]). For inviscid fluids, if Loitsyansky's integral [76] is an invariant, then $\sigma = 4$ and $n = 10/7$ [77]; if Birkhoff's integral [78] is an invariant, then $\sigma = 2$ and $n = 6/5$ [79]. It has been recently shown that time-invariant integral length scale l corresponds to $\sigma = \infty$

and $n = 2$ and time-invariant Reynolds number corresponds to $\sigma = 1$ and $n = 1$ [80]. Furthermore, the conservation of energy, angular momentum, and helicity lead to $\sigma = 2$, 7, and 1, in the limit of $\mathrm{Re} \to \infty$, respectively. The energy conservation of inviscid fluid uniquely determines the invariant solution of Eq. (4.1), i.e., $\sigma = 2$, in accordance with Birkhoff's invariant [78]. Despite the apparent simplicity of the decaying HIT problem, the relevant flow invariant, asymptotic decay exponent and the low wave-number scaling are strong functions of the initial spectrum and Reynolds number. There is still no clear consensus on whether the angular momentum or energy is the correct invariant. It is also not clear what the conditions are under which the invariance of either quantity can be observed. Consequently, various results have been reported [67, 68, 74, 81].

We perform detailed comparisons with established data qualitatively and quantitatively on the following important items: (i) energy decay exponent n, (ii) low wave-number scaling of the spectra, (iii) flow structure, and (iv) effect of rotation on kinetic energy decay.

C. LBE Formulation for DNS and LES of turbulence

1. Lattice Boltzmann equation for DNS

The LBE with single-relaxation-time approximation due to Bhatnagar, Gross, and Krook (BGK) [36] for the collision operator is [24, 25]

$$f_\alpha(\vec{x} + \vec{e}_\alpha \delta_t, t + \delta_t) = f_\alpha(\vec{x}, t) - \frac{1}{\tau}\left[f_\alpha - f_\alpha^{(\mathrm{eq})}\right] + F_\alpha, \tag{4.4}$$

where f_α is the density distribution function with discrete velocity $\vec{e}_\alpha$ along the αth direction, $f_\alpha^{(\mathrm{eq})}$ is the equilibrium distribution function, and τ is the relaxation time due to the fluid particle collision determining the viscosity ν of the modelled fluid. In

what follows, we use the LBE model with 19 velocities in three dimensions, i.e., the D3Q19 model shown in Fig. 13.

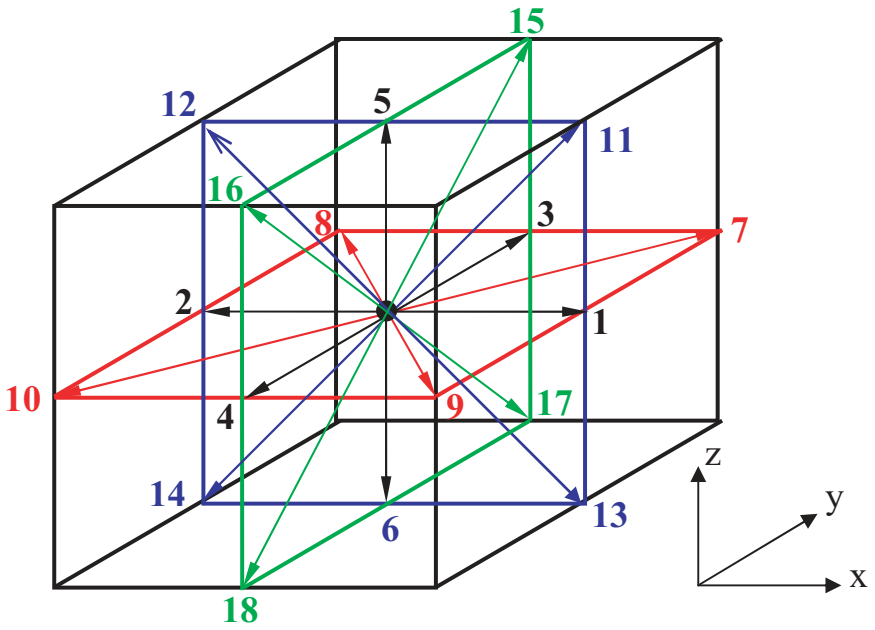

Fig. 13. 3D 19 velocities lattice.

The discrete velocities are:

$$\vec{e}_\alpha = \begin{cases} (0,\,0), & \alpha = 0 \\ (\pm 1,\,0,\,0)c, (0,\,\pm 1,\,0)c, (0,\,0,\,\pm 1)c, & \alpha = 1\text{–}6 \\ (\pm 1,\,\pm 1,\,0)c, (\pm 1,\,0,\,\pm 1)c, (\pm 1,\,\pm 1,\,0)c, & \alpha = 7\text{–}18. \end{cases} \tag{4.5}$$

The equilibria for incompressible flow [82] are

$$f_\alpha^{(\mathrm{eq})} = w_\alpha \left\{ \delta\rho + \rho_0 \left[\frac{3\vec{e}_\alpha \cdot \vec{u}}{c^2} + \frac{9(\vec{e}_\alpha \cdot \vec{u})^2}{2c^4} - \frac{3u^2}{2c^2} \right] \right\}, \tag{4.6}$$

where $\delta\rho$ is the density fluctuation, and ρ_0 is the constant mean density in the system which is usually set to 1, and $c = \delta_x/\delta_t = 1$ in lattice units (i.e. $\delta_t = \delta_x$). The sound speed of the model is $c_s = c/\sqrt{3}$. The total density is $\rho = \rho_0 + \delta\rho$. The weighting

factors w_α for the D3Q19 model are $w_0 = 1/3$, $w_{1-6} = 1/18$, and $w_{7-18} = 1/36$. The mass and momentum conservations are strictly enforced:

$$\delta\rho = \sum_\alpha f_\alpha = \sum_\alpha f_\alpha^{(\mathrm{eq})}, \tag{4.7a}$$

$$\rho_0 \vec{u} = \sum_\alpha \vec{e}_\alpha f_\alpha = \sum_\alpha \vec{e}_\alpha f_\alpha^{(\mathrm{eq})}. \tag{4.7b}$$

For athermal fluids, the forcing term F_α is [83]

$$F_\alpha = -3 w_\alpha \rho_0 \frac{\vec{e}_\alpha \cdot \vec{a}}{c^2} \delta_t, \tag{4.8}$$

where $\vec{a}$ is the acceleration due to external force. In our simulations, only for rotating case, we consider the Coriolis force, i.e., $\vec{a} = -2\vec{\Omega} \times \vec{u}$, where $\vec{\Omega}$ is the angular velocity of the frame of reference.

The hydrodynamic equations derived from Eq. (4.4) via the Chapman-Enskog analysis are

$$\partial_t \rho + \vec{\nabla} \cdot \rho \vec{u} = 0, \tag{4.9a}$$

$$\partial_t \vec{u} + \vec{u} \cdot \vec{\nabla} \vec{u} = -\vec{\nabla} p + \nu \nabla^2 \vec{u} + \vec{a}, \tag{4.9b}$$

where $p = c_s^2 \rho / \rho_0$ and the kinematic viscosity ν has the following relation with the relaxation time

$$\nu = \frac{1}{3}\left(\tau - \frac{1}{2}\right) c\delta_x. \tag{4.10}$$

It is important to note that in LBE the strain rate tensor S_{ij} can be obtained directly from the second-order moment of the non-equilibrium distribution function as

$$\mathsf{S}_{ij} = -\frac{1}{2\rho_0 c_s^2 \tau} \sum_\alpha e_{\alpha i} e_{\alpha j} \left[f_\alpha - f_\alpha^{(\mathrm{eq})} \right], \tag{4.11}$$

so that the dissipation rate is computed as $\varepsilon = 2\nu \sum_{i,j} \mathsf{S}_{\mathsf{ij}} \mathsf{S}_{\mathsf{ij}}$.

2. LES extension of lattice Boltzmann equation

For the LES, high wave number Fourier components of the density distribution function are filtered and the resolved-scale distribution function is separated from the unresolved part. The filtered form of the LBE for LES is modelled as [84]:

$$\overline{f}_\alpha(\vec{x}+\vec{e}_\alpha\delta_t, t+\delta_t) = \overline{f}_\alpha(\vec{x},t) - \frac{1}{\tau^*}[\overline{f}_\alpha - \overline{f}_\alpha^{(\mathrm{eq})}] + F_\alpha, \tag{4.12}$$

where $\overline{f}_\alpha$ and $\overline{f}_\alpha^{(\mathrm{eq})}$ represent the distribution function and the equilibrium function of the resolved scales respectively. The effect of the unresolved scale motion is modelled through an effective collision τ_t which has been included in the LES effective relaxation time τ^* in Eq. (4.12). The LES effective viscosity ν^* is then obtained from

$$\nu^* = \nu + \nu_t = \frac{1}{3}\left(\tau^* - \frac{1}{2}\right) c\delta_x, \tag{4.13}$$

with ν_t denoting turbulent viscosity usually called eddy viscosity.

To evaluate the fidelity of the LBE-LES simulations, we use the Smagorinsky model [2, 85] for the small unresolved scale motion. In the Smagorinsky model, the eddy viscosity ν_t is calculated from the filtered strain rate tensor $\overline{\mathsf{S}}_{ij} = (\partial_j\overline{u}_i + \partial_i\overline{u}_j)/2$ and a filter length scale δ_x as follows:

$$\nu_t = (C_{sm}\delta_x)^2\overline{S}, \tag{4.14}$$

$$\overline{S} = \sqrt{2\sum_{i,j}\overline{\mathsf{S}}_{ij}\overline{\mathsf{S}}_{ij}}, \tag{4.15}$$

where $\overline{S}$ is the characteristic filtered rate of strain and C_{sm} is the Smagorinsky constant. With C_{sm} and δ_x given, τ_t can be obtained from Eq (4.11) [84]:

$$\tau_t = \frac{1}{2}\left(\sqrt{\tau^2 + 18\sqrt{2}(\rho_0 c^2)^{-1}C_{sm}^2\delta_x\overline{S}} - \tau\right). \tag{4.16}$$

As shown in Eq. (4.11), the filtered strain rate tensor $\overline{\mathsf{S}}_{ij}$ can be computed from the

second-order moment of the filtered nonequilibrium distribution function directly. In Eq. (4.16), the filtered strain rate $\overline{S}$ which is used to determine ν_t is current in time. Because the time step in the LBE simulations is relatively small in physical units, we can also use the value of $\overline{S}$ of the previous time step and compute ν_t ($\nu_t = c_s^2 \tau_t \delta_t$) according to Eq. (5.6) instead of Eq. (4.16). We will evaluate both these options. Furthermore, it is possible to use finite difference approximation for $\overline{S}$. We will also investigate this option.

It is important to point out the salient difference between the LBE-LES and the NS-LES. In the NS-LES, the eddy viscosity is evaluated and then used to determine the evolution of the flow fields in the next time step. In the LBE-LES, the eddy viscosity affects the relaxation process of the flow fields as well as other nonhydrodynamic variables (higher order fluxes). The relaxation process, as described by Eq. (4.12), does not force the flow fields to immediately attain the expected state specified by the equilibrium distributions. This preserves more spatio-temporal memory effects in the LBE-LES which are absent in the NS-LES counterpart. Some preliminary tests using the LBE-LES have yielded encouraging results [84, 86, 87]. In this work we will compare the LBE-LES and NS-LES in the fundamental problem of HIT.

In all the results presented in this chapter, we use the single-relaxation-time LBE obtained from the BGK model for the collision operator. Preliminary computations of LBE-DNS in an inertial frame using the multiple-relaxation-time(MRT) lattice Boltzmann model show no distinguishable difference in the results obtained. We will investigate the use of MRT for LBE-DNS in rotational frame and LBE-LES in the future work.

D. Simulation results

All numerical simulations are conducted in a three-dimensional periodic cube with various resolutions: N^3. The initial incompressible homogeneous isotropic velocity field is generated in spectral space with the following energy spectrum in a prescribed range $\kappa_{\min} \leq \kappa \leq \kappa_{\max}$ (For further details, see the on-line article: T. Miyauchi and T. Ishizu, "Direct numerical simulation of HIT decay of passive scalar fluctuation," available at http://cfd.me.umist.ac.uk/ercofold/database/test48/test48.html):

$$\hat{E}(\kappa, 0) = \begin{cases} 0.038\kappa^m \exp(-0.14\,\kappa^2), & \kappa \in [\kappa_{\min},\, \kappa_{\max}], \\ 0, & \kappa \notin [\kappa_{\min},\, \kappa_{\max}], \end{cases} \tag{4.17}$$

with random phase and then transferred to physical space. In the above, m is set to 4 or 2 for different simulations.

The initial density fluctuation $\delta\rho$ (or the pressure p) can be consistently obtained by an iteration procedure. It is important to stress that the preparation of the initial data is crucial in the LBE-DNS simulations of HIT. The pressure obtained by solving the Poisson equation from the initial velocity $\vec{u}_0$ is inconsistent and insufficient to initialize the LBE simulation. It is inconsistent because LBE is intrinsically compressible thus the Poisson equation is not satisfied exactly. It is insufficient because LBE initial data consists of more than the hydrodynamic variables and the nonhydrodynamic variables cannot be specified by solving hydrodynamic equations. By consistently constructing the initial data for the LBE simulation, we are able to minimize the error due to initialization and the difference between the LBE and pseudo-spectral simulations [73].

1. LBE-DNS of decaying isotropic turbulence

a. Inertial reference frame

We first present the results from LBE-DNS of decaying HIT in the inertial frame at two resolutions: 64^3 and 128^3. All initial spectra are given by Eq. (4.17) in which m is set to 4 unless indicated otherwise. Fig. 14 shows the evolutions of the

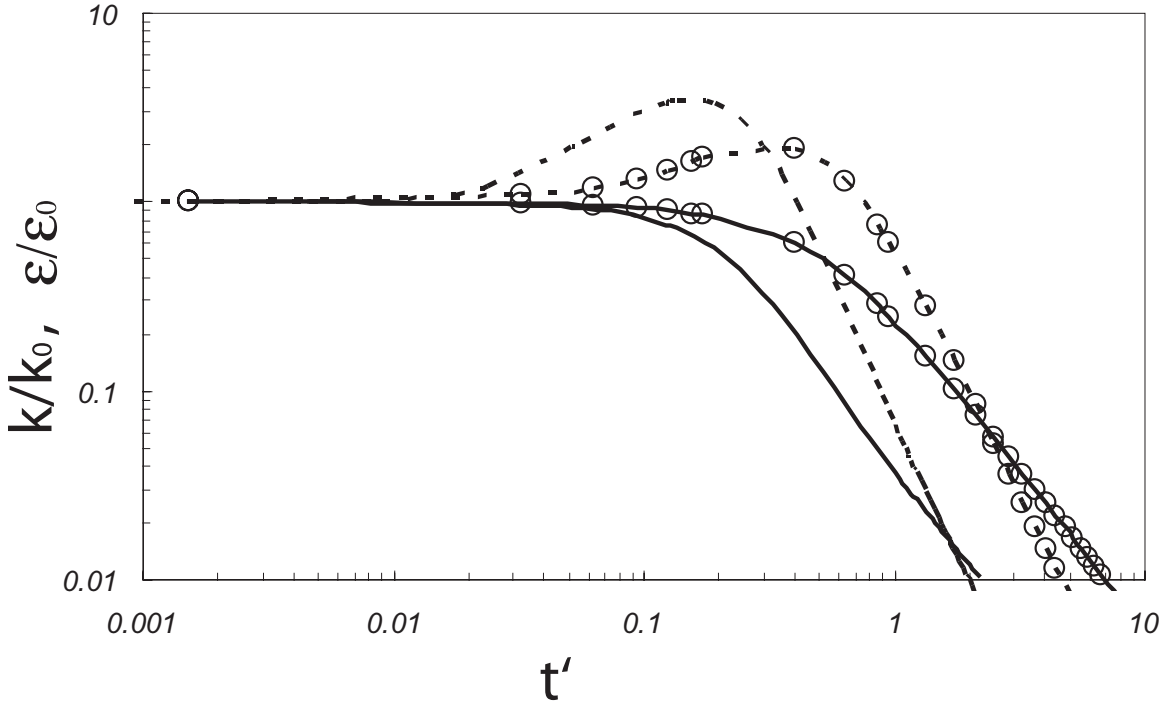

Fig. 14. Time evolution of the normalized kinetic energy k/k_0 (solid lines) and normalized dissipation rate $\varepsilon/\varepsilon_0$ (dashed lines) for 64^3 (lines and symbols) and 128^3 (lines only) by using LBE-DNS.

normalized kinetic energy k/k_0 and the normalized dissipation rate $\varepsilon/\varepsilon_0$ with respect to normalized time $t' = t\varepsilon_0/k_0$ for the cases of 128^3 and 64^3. The parameters for both cases are $u_{\rm rms} = 0.023$ and $\nu \approx 0.0017$ ($\tau = 0.505$). In the case of 64^3, the initial energy spectrum is non-zero in the range $4 \leq \kappa \leq 8$, resulting in $\mathrm{Re}_\lambda \approx 53$. For the case of 128^3, the initial energy spectrum is non-zero in the range $1 \leq \kappa \leq 8$, resulting

in $\mathrm{Re}_\lambda \approx 119$. In the absence of production, kinetic energy decays monotonically in time, whereas at early stages the dissipation rate increases. This increase in $\varepsilon/\varepsilon_0$ is completely consistent with known turbulence physics (explained further below) and the same phenomenon is also seen in NS-DNS results. Following this period of increasing dissipation, both the kinetic energy and dissipation decay monotonically. The decay exponent n of the kinetic energy in these low Re_λ simulations varies in time. Furthermore, Re_λ itself is a function of time as the turbulence decays. The variation of n vs. Re_λ in various simulations are shown in Fig. 15. The dependence of n on Re_λ obtained by the LBE-DNS is very similar to that observed in NS-DNS calculations [68]. The values of n obtained in the present work agree well with the experimental and numerical NS-DNS data.

In Fig. 16, the upper plot (Fig. 16(a)) shows the compensated energy spectra $[\hat{E}(\kappa, t)/\kappa^4]$ of the above 128^3 simulation at early times during which cascade is the dominant process. Initially, the spectrum (dashed line) is narrow and soon the energy spreads to higher wave numbers (smaller scales) due to the nonlinear cascade process. This phenomena leads to the increase of the dissipation rate in physical space, as shown in Fig. 14. This fact, in itself, is significant since advection (the source of nonlinearity) is handled very differently in LBE. At this stage, the spectrum scales as $\hat{E}(\kappa, t') \sim \kappa^4$ at small κ. The bottom plot (Fig. 16 (b)) shows another 128^3 simulation which has the same rms of the initial velocity field and ν as the upper case but the initial non-zero energy is concentrated in the range of $8 \leq \kappa \leq 16$, resulting in $Re_\lambda \approx 67$. In spite of the different range of initial energy, the spectrum still scales as $\hat{E}(\kappa, t') \sim \kappa^4$.

Next we show results from a set of simulations in which the initial spectrum is also given by Eq. (4.17) but with $m = 2$. In Fig. 17, the compensated spectrum $\hat{E}(\kappa)/\kappa^2$ is shown at various times. It is seen that the spectrum now scales as κ^2. In

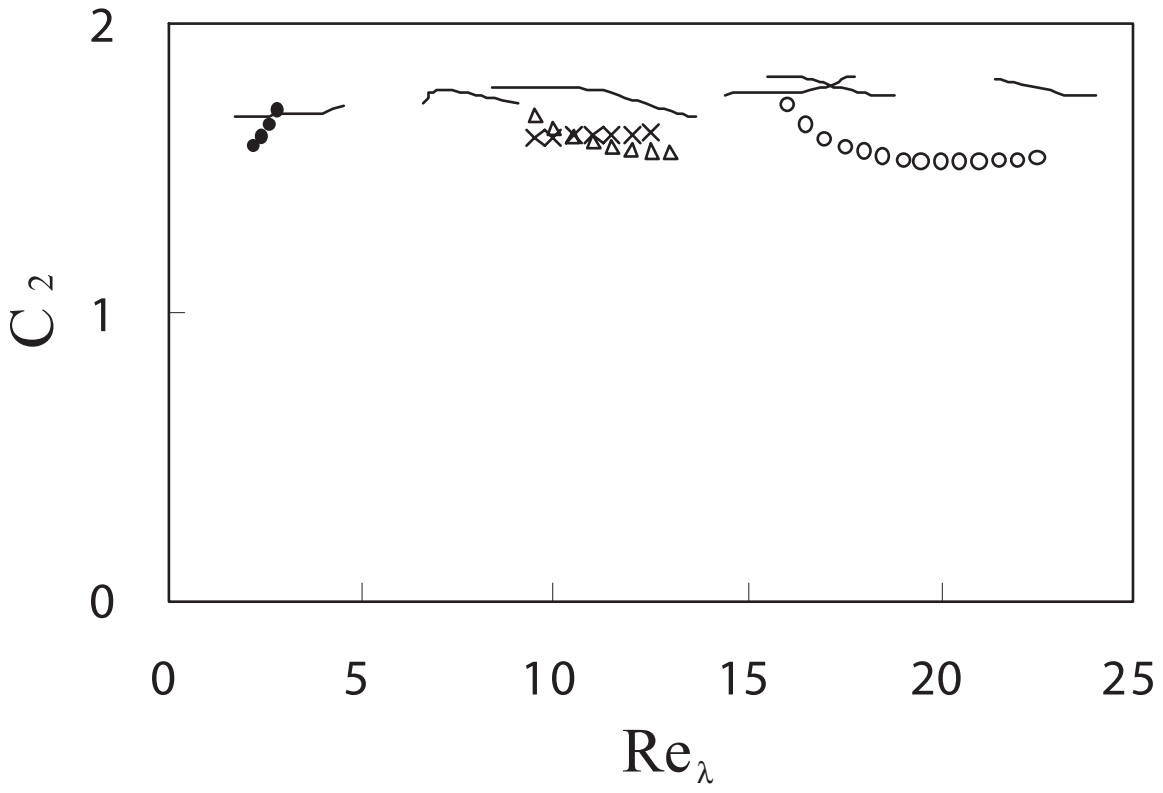

Fig. 15. Dependence of the decay exponent $n = 1/(C_2 - 1)$ on initial conditions and Re_λ. The quantity C_2 is depicted in the figure instead of n. Solid lines represent NS-DNS data from Mansour & Wray [68] and symbols correspond to the LBE-DNS results of the present work. For the 128^3 resolution, •: $u_{\mathrm{rms}} = 0.0064$, $k_{\mathrm{min}} = 1$, $k_{\mathrm{max}} = 8$, and $\nu = 0.01$ ($\tau = 0.53$); △: $u_{\mathrm{rms}} = 0.021$, $k_{\mathrm{min}} = 8$, $k_{\mathrm{max}} = 16$, and $\nu \approx 0.00167$ ($\tau = 0.505$); ∘: $u_{\mathrm{rms}} = 0.022$, $k_{\mathrm{min}} = 1$, $k_{\mathrm{max}} = 8$, and $\nu \approx 0.00167$ ($\tau = 0.505$). For the 64^3 resolution (×): $u_{\mathrm{rms}} = 0.022$, $k_{\mathrm{min}} = 4$ and $k_{\mathrm{max}} = 8$, and $\nu \approx 0.00167$ ($\tau = 0.505$).

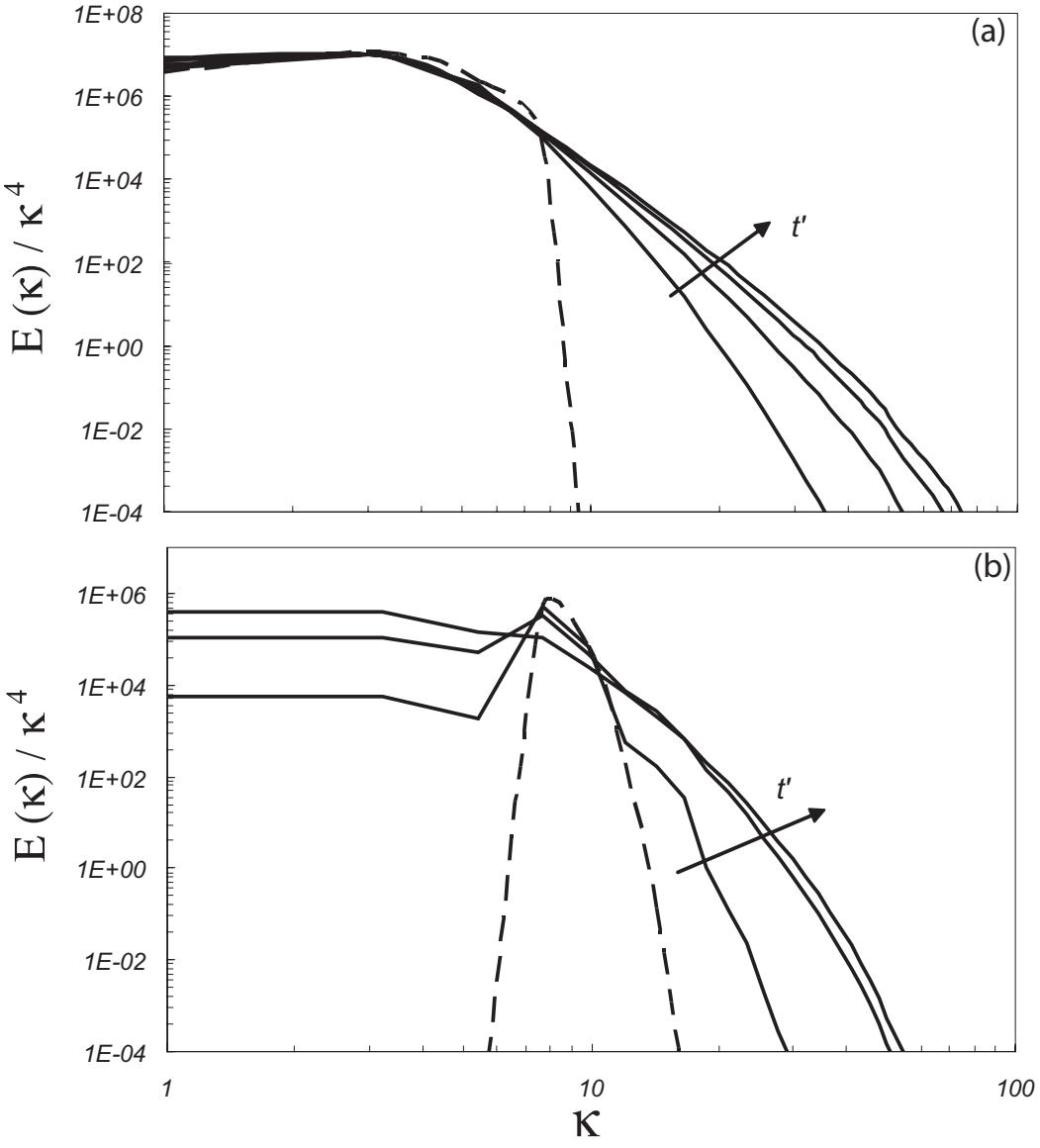

Fig. 16. Compensated energy spectra for two cases of 128^3 at early times. (a) $t' = 0.022$, 0.044, 0.066, and 0.088; (b) $t' = 0.0022$, 0.022, and 0.088. The dashed lines represent the initial spectra given by Eq. (4.17) with $m = 4$. The spectra scale as $\hat{E}(\kappa, t') \sim \kappa^4$ at small κ.

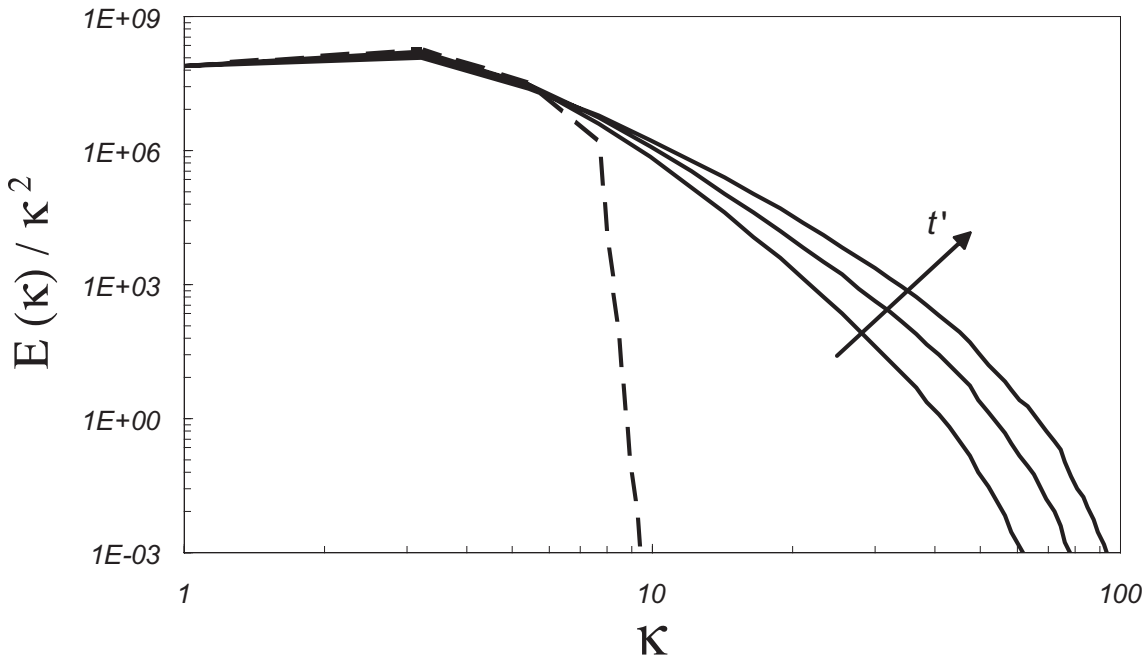

Fig. 17. Compensated energy spectra for a 128^3 simulation ($u_{\rm rms} = 0.023$, $\nu \approx 0.0017$ ($\tau = 0.505$), and $Re_\lambda \approx 141$), at early times, $t' = 0.011,\ 0.017,\ 0.027$. The dashed lines represent the initial spectra given by Eq. (4.17) with $m = 2$. The spectra scale as $\hat{E}(\kappa, t') \sim \kappa^2$ at small κ.

summary, as shown in Fig. 18, the low wave-number spectra scale as $\hat{E}(\kappa) \sim \kappa^4$ (Fig. 18 (a)) if $m = 4$ and $\hat{E}(\kappa) \sim \kappa^2$ (Fig. 18 (b)) if $m = 2$. This dependence of low-wave number scaling on initial spectrum is in exact agrement with the results reported in Mansour & Wray [68] and Huang & Leonard [67].

b. Rotating reference frame.

LBE-DNS of decaying HIT in a rotating frame is also performed. Without loss of generality, we assume that the frame of reference rotates about the z-axis with the angular velocity $\vec{\Omega} = (0, 0, \omega)$. The Rossby number is defined as $\mathrm{Ro} = \kappa_p u_{\mathrm{rms}}/\omega$, where κ_p characterizes the energy containing wave number at $t = 0$. Here, we use $\kappa_p = (\kappa_{\max} - \kappa_{\min})/2$.

The effects of rotation are scale dependent and they are enhanced by increasing the rotation rate ω (decreasing Ro). In general, it has been well understood that rotation slows down the cascade and delays the approach to equipartition [88, 89]. These features are captured in Figs. 19 and 20. Fig. 19 shows the evolution of kinetic energy at various Rossby numbers in a simulation with 128^3 resolution. The initial energy spectrum is non-zero in the range of $1 \leq \kappa \leq 8$. As expected, the energy decay slows down with decreasing Rossby number (or increasing rate of rotation). Closer examination of the spectra (Fig. 20) shows the tendency to maintain more energy at the small wave numbers (large scales) when the system rotates. The faster the system rotates (smaller Rossby number), the more prominent is this tendency.

2. LBE-LES of decaying isotropic turbulence

In the previous section, it was clearly demonstrated that the LBE method is an accurate DNS tool for turbulence. It is also important to asses the ability of LBE in the LES context. In this work, we conduct LES of decaying HIT without rotation.

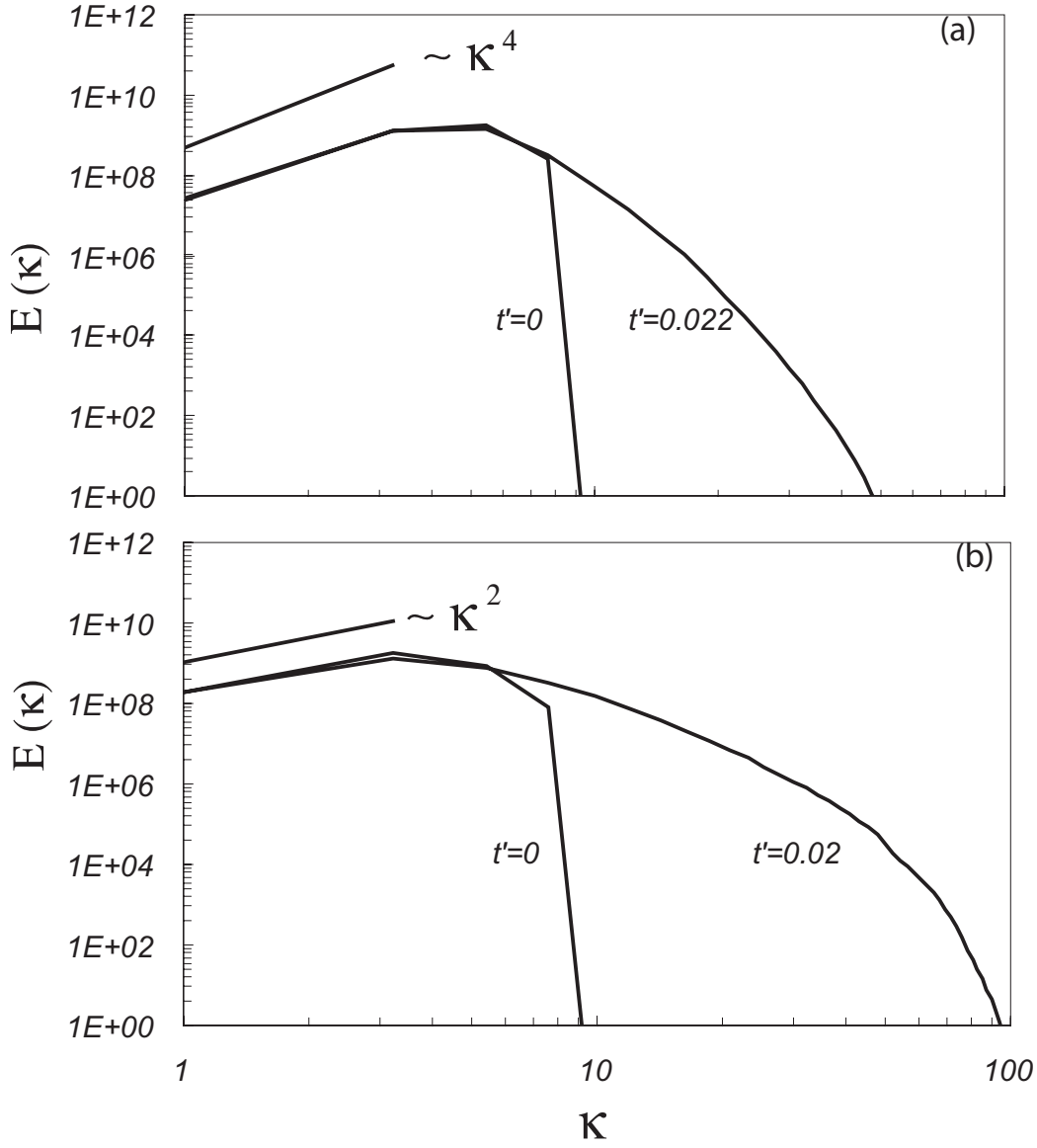

Fig. 18. Energy spectra for two cases of 128^3 above with initial energy concentrating in the range of $1 \leq \kappa \leq 8$ at $t' = 0$ and $t' = 0.022$ respectively. The initial energy spectra: (a) $E(\kappa) = 0.038\kappa^4 \exp(-0.14\,\kappa^2)$; (b) $E(\kappa) = 0.038\kappa^2 \exp(-0.14\,\kappa^2)$ respectively.

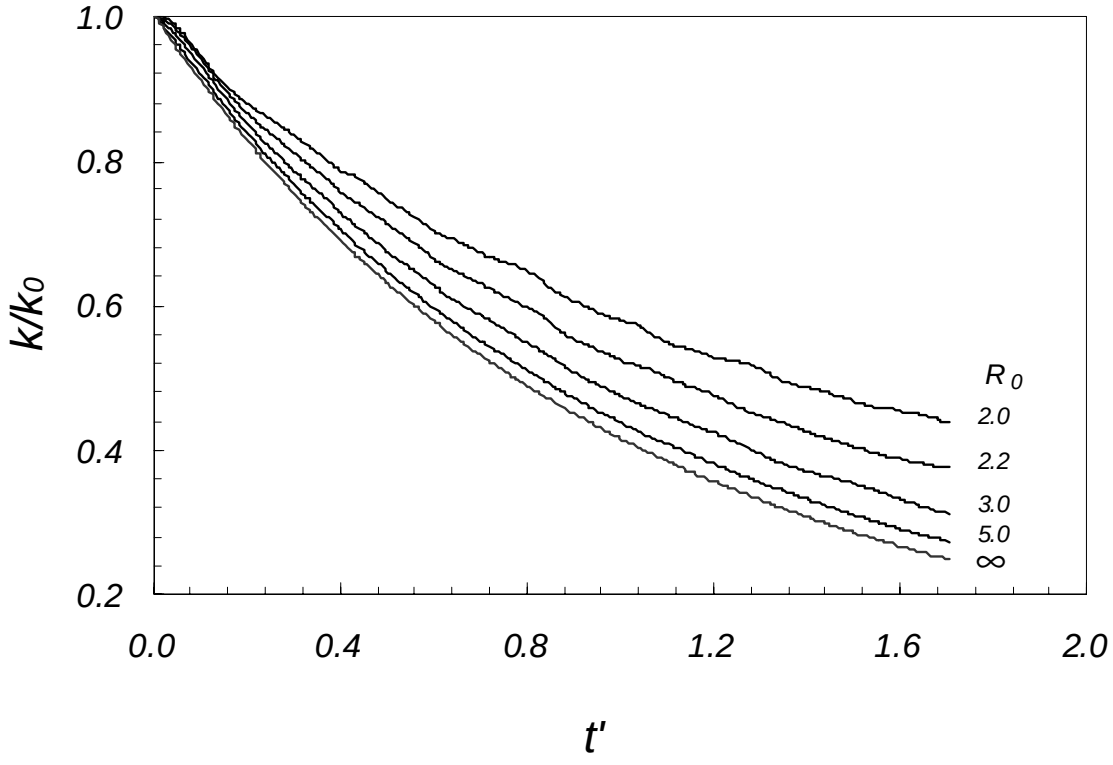

Fig. 19. Kinetic energy decay in 128^3 LBE-DNS with different Rossby number Ro.

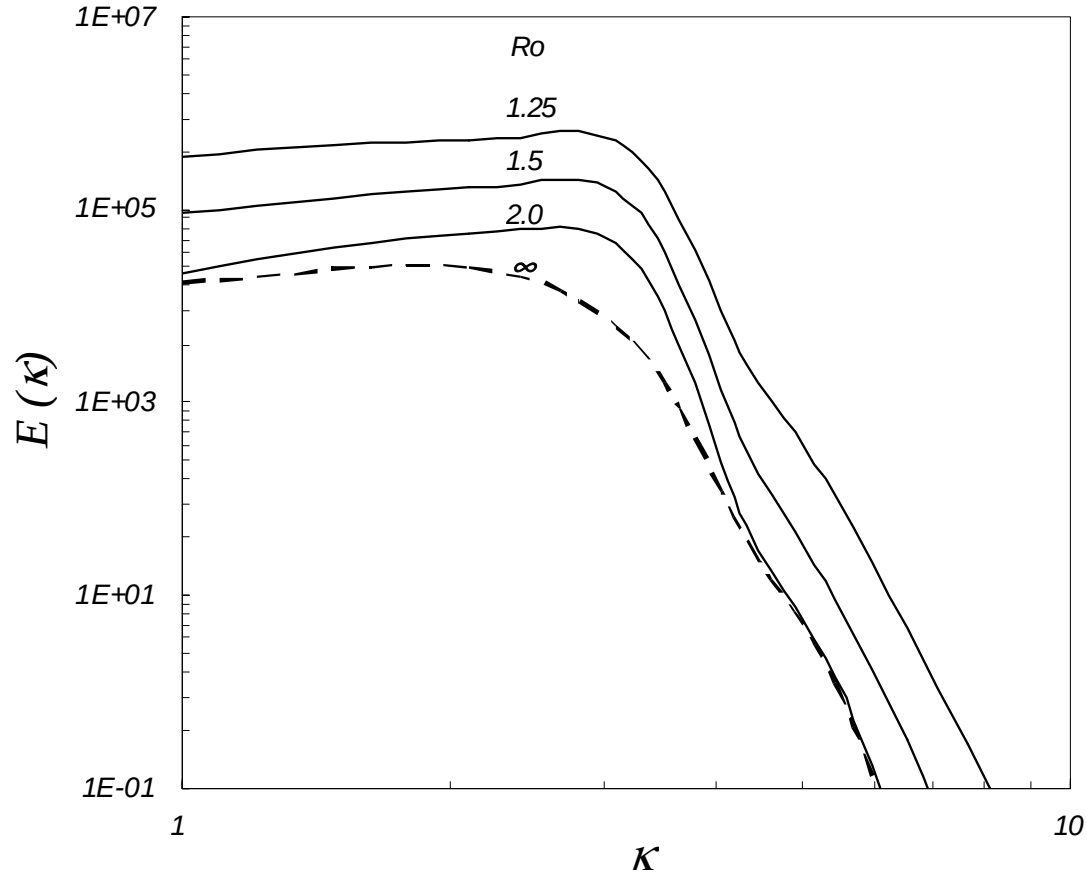

Fig. 20. Energy spectra at $t' = 10.5$ with different Rossby number Ro for 64^3 case: $u_{\rm rms} = 0.023$, $k_{\rm min} = 1$, $k_{\rm max} = 4$, and $\nu = 0.01$ ($\tau = 0.53$). The dashed line is the inertial case ($\vec{\Omega} = \vec{0}$ or Ro $= \infty$).

Investigation of the LES of decaying HIT with rotation will be presented in the near future.

In order to perform close comparisons with DNS results, we perform LES with the initial large-scales identical to that of 128^3 LBE-DNS case (corresponding to the results presented in Fig. 14). Thus the initial flow fields obtained in the LBE-DNS are appropriately truncated in spectral space to yield the initial fields for the LBE-LES for 32^3 and 64^3 resolutions. In other words, the initial LBE-LES field is obtained by

filtering out all wave numbers above 16 for 32^3 and 32 for 64^3.

a. Calibration of C_{sm}

Our first exercise is to determine the appropriate Smagorinsky constant for LBE-LES. Fig. 21 shows the energy spectra at some specific time instant with different Smagorinsky constant values for both 32^3 and 64^3 cases. The instantaneous LES spectra with resolutions 32^3 and 64^3 are compared against DNS spectrum at the same time. In general, 64^3 performs better than 32^3 although at small κ (large scale) region both 32^3 and 64^3 spectra agree well with the DNS spectrum. The comparison of the kinetic energy decay from the same runs is shown in Fig. 22. From both figures, we find that $C_{sm} = 0.1$ yields better results than the typical value of $C_{sm} = 0.17$ used in the NS-LES [2]. The need for a reduced C_{sm} in LBE-LES compared with the NS-LES value can be explained as follows. In the lattice Boltzmann equation there are nonhydrodynamic variables which are higher order fluxes ($\partial_i^n u_j$, $n > 1$). These higher order fluxes could lead to a higher effective viscosity and other nonlinear effects. Thus a smaller C_{sm} value in LBE-LES is adequate to achieve the same effect as a larger C_{sm} in NS-LES. In Fig. 23, we compare the instantaneous flow structure of $u_z(i, j, k = N/2, t')$ obtained by the LBE-LES with that by LBE-DNS. As shown in Fig. 23, the LBE-LES appears to capture the flow-field structure quite adequately even with a coarse resolution of 32^3. In all subsequent calculations, we use $C_{sm} = 0.1$.

b. Other methods of $\overline{S}$ computation

In all the above calculations, we determine $\overline{S}$ (in the express of ν_t) from the second moment of nonequilibrium distribution functions at the current time-step. We now investigate the other options for determining $\overline{S}$ which may provide some computational advantages.

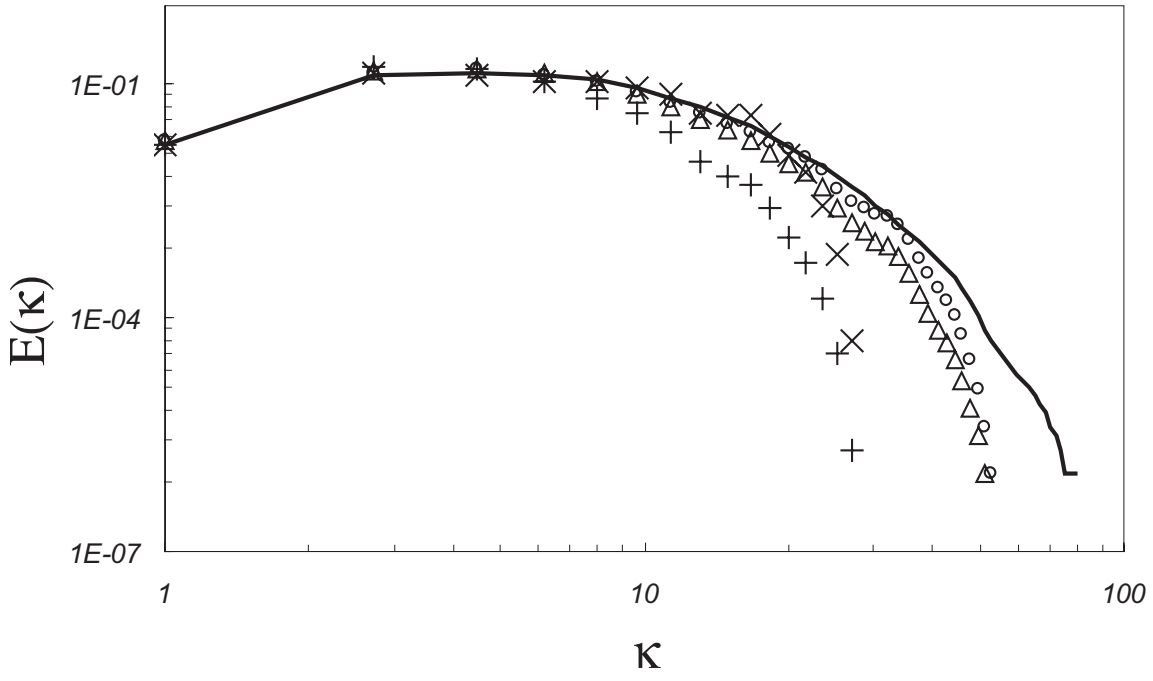

Fig. 21. Energy spectra at $t' = 0.04796$ with different C_{sm} and resolution. Solid line for LBE-DNS (128^3) and symbols for LBE-LES ($\circ$: 64^3, $C_{sm} = 0.1$; $\triangle$: 64^3, $C_{sm} = 0.17$; $\times$: 32^3, $C_{sm} = 0.1$; $+$: 32^3, $C_{sm} = 0.17$).

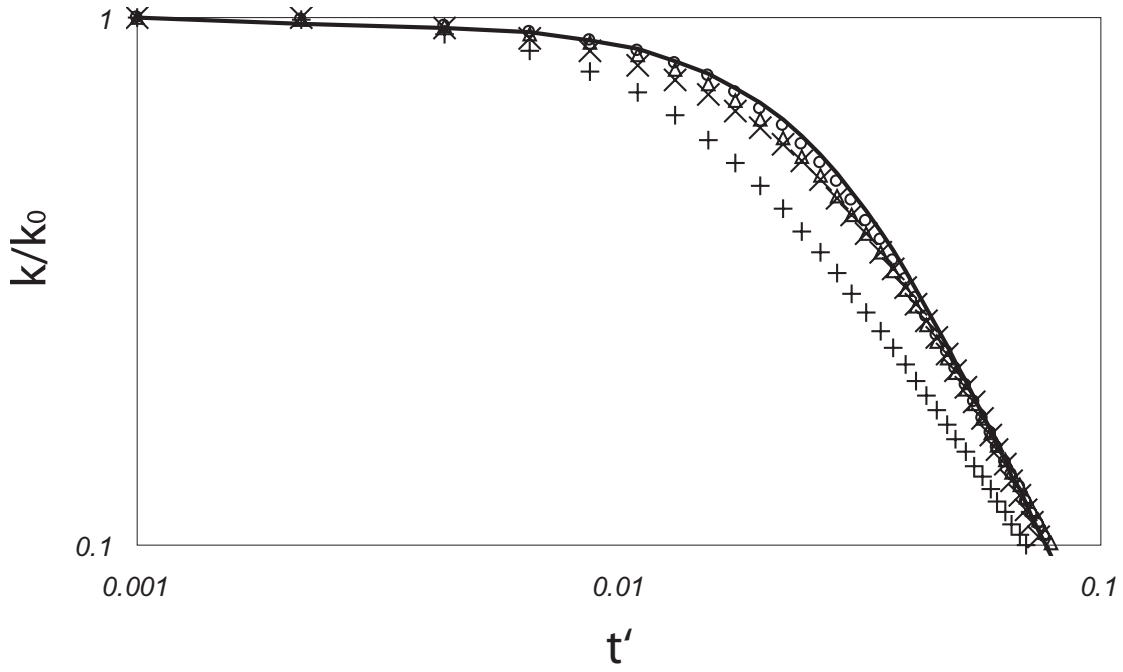

Fig. 22. Kinetic energy decay with different C_{sm} and resolution. Solid line for LBE-DNS (128^3) and symbols for LBE-LES ($\circ$: 64^3, $C_{sm} = 0.1$; $\triangle$: 64^3, $C_{sm} = 0.17$; $\times$: 32^3, $C_{sm} = 0.1$; $+$: 32^3, $C_{sm} = 0.17$).

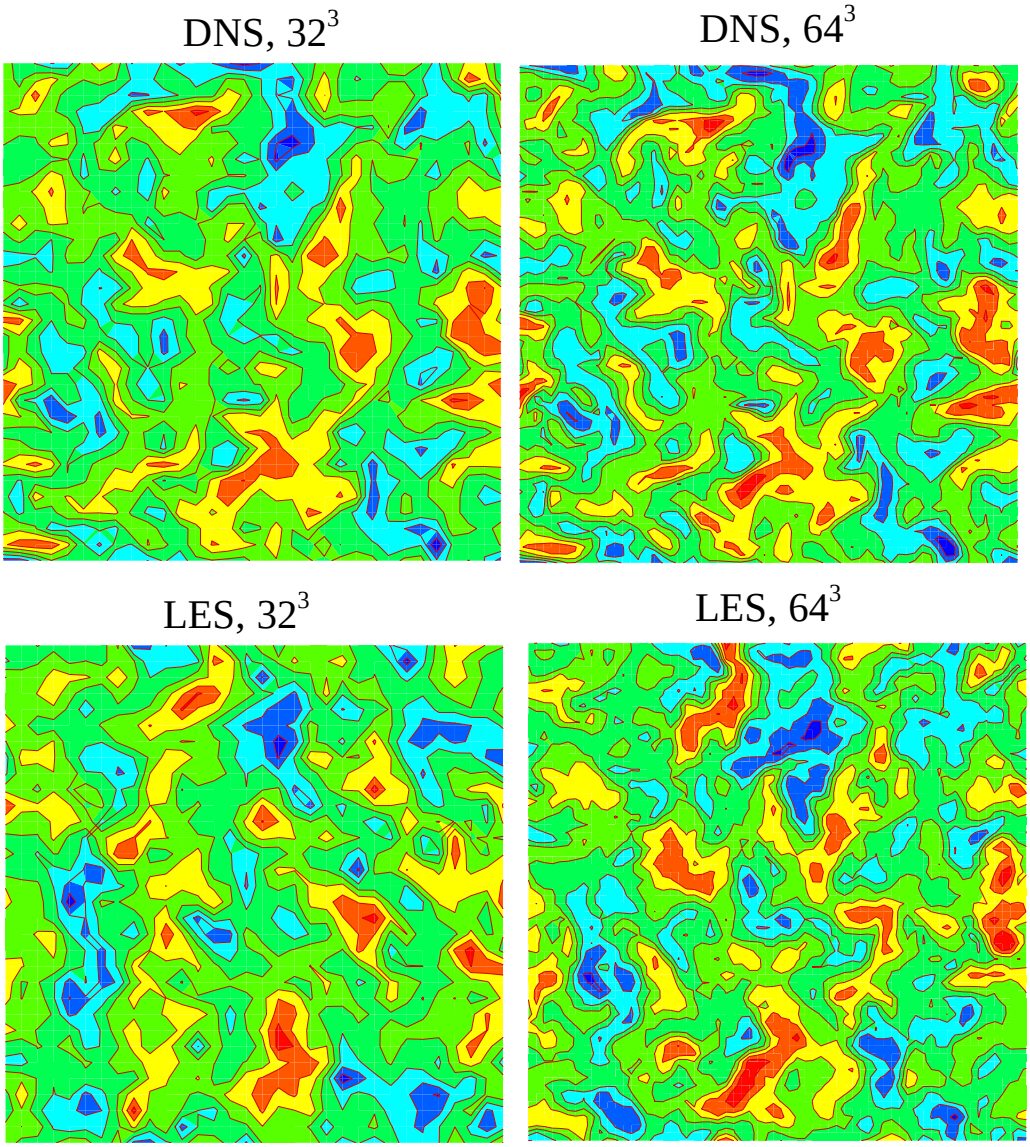

Fig. 23. Contours of the instantaneous flow field $u_z(i, j, k = N/2, t')$. LBE-DNS vs. LBE-LES with different resolutions. The $32^3$and 64^3 LBE-DNS contours shown here are obtained by truncating the 128^3 LBE-DNS data.

First, we test two different ways to compute the strain rate tensor: (i) from the second moment of nonequilibruim distribution functions as given in Eq. (4.11) and (ii) by finite-difference approximation of derivatives $\overline{\mathsf{S}}_{ij} = (\partial_j \overline{u}_i + \partial_i \overline{u}_j)/2$. In Fig. 24, we compare the kinetic energy evolution from both computations with LBE-DNS result at two resolutions. In the 32^3 case (Fig. 24, upper), it is seen that the computation using finite-difference approximation quickly diverges while computation from the nonequilibrium distribution function moment captures the DNS result. In the 64^3 case (Fig. 24, bottom), since the resolution is high enough, both computations yield good results. Next, we test two different ways of computing strain rate $\overline{S}$ from the second moment of nonequilibruim distribution functions. In the implicit method, $\overline{S}$ of the current time-step is used to yield Eq. 4.16 for ν_t. In the explicit approach, $\overline{S}$ from previous time-step is used (as in Eq. 5.6).

Fig. 25 depicts the contours of the instantaneous flow structure of $u_z(i,\, j,\, k = N/2,\, t')$ obtained from LBE-LES (32^3) by using the two formulae to compute ν_t. The velocity fields obtained with the two formulae are almost identical, as shown in Fig. 25; the L^2-norm difference between the two velocity fields is less than 0.02%. Therefore, we verify that the eddy viscosity can be computed by either Eq. (4.16) or Eq. (5.6) without significant effect on the flow fields.

3. LBE-LES vs. NS-LES

We further compare the LBE-LES with the NS-LES results at 32^3 resolution and the results are shown in Figs. 26 – 28.

The initial velocity fields for LBE-LES and NS-LES calculation are nearly identical. From Figs. 26 and 27, it is seen that the kinetic energy and spectra computed from LBE-LES are somewhat closer to the DNS results than those calculated from NS-LES. The difference can be seen more clearly from contours of the instantaneous

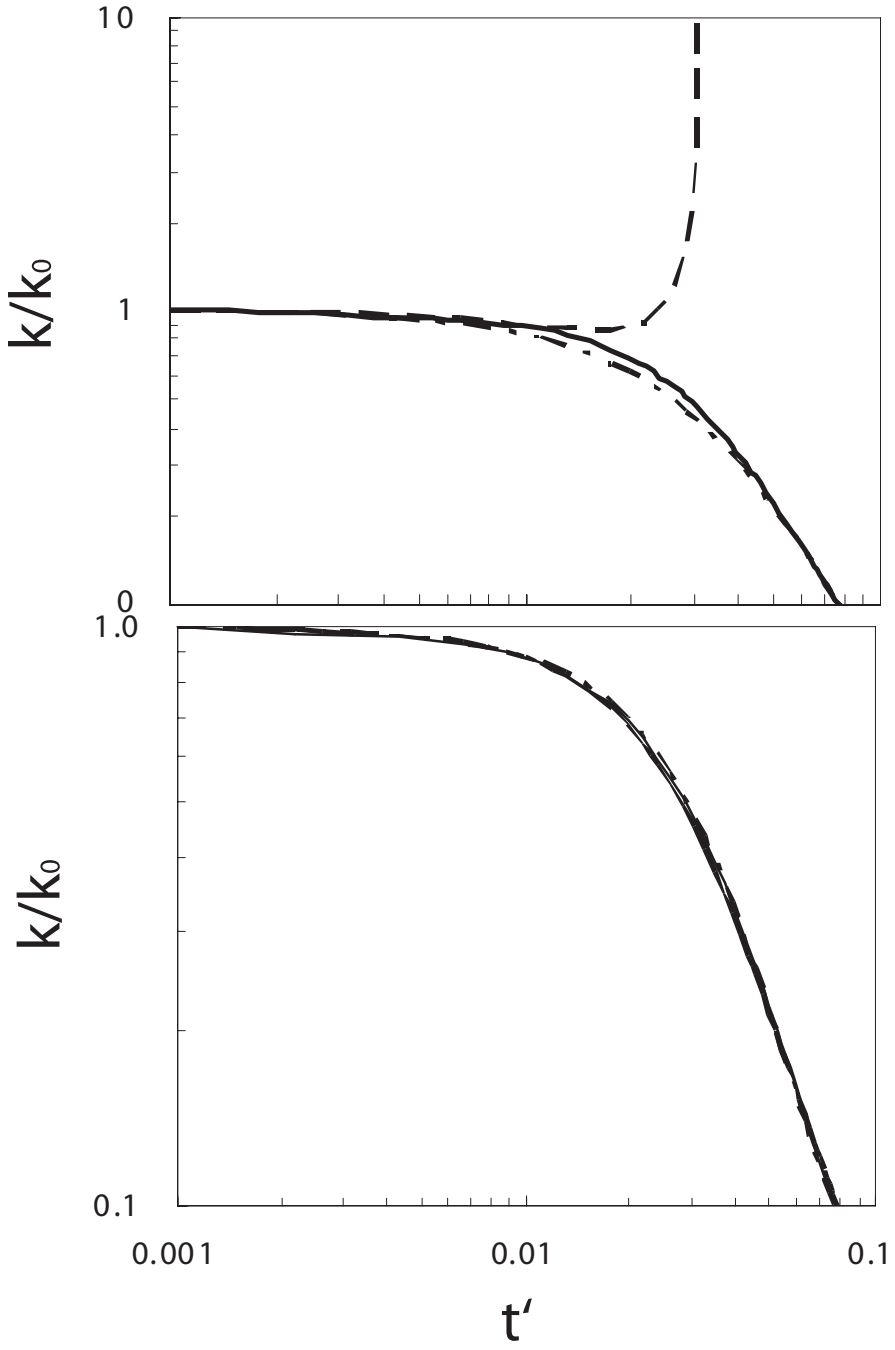

Fig. 24. 32^3 (upper) and 64^3 (bottom) kinetic energy decays of LBE-LES with different ways to compute strain rates vs. LBE-DNS. Solid lines: LBE-DNS; Dashed lines: LBE-LES, strain rate computed by finite difference; Dashed-dot lines: LBE-LES, strain rate computed by nonequilibrium distribution functions.

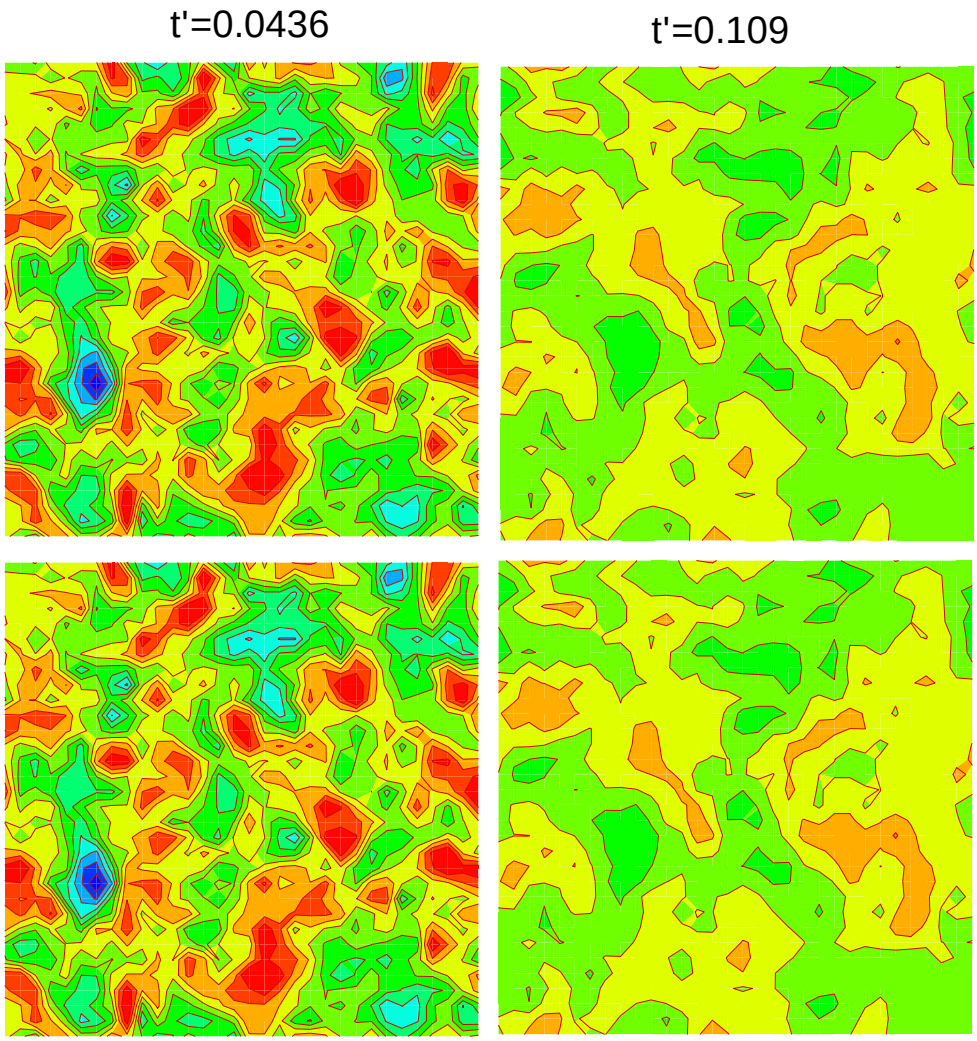

Fig. 25. Contours of the instantaneous flow field $u_z(i, j, k = N/2, t')$ obtained by LBE-LES with a resolution of 32^3 and two different formulae for ν_t in two different times. Top row: ν_t is computed according to Eq. (4.16) and bottom row: ν_t is computed according to Eq. (5.6) with one time step lagging in $\overline{S}$.

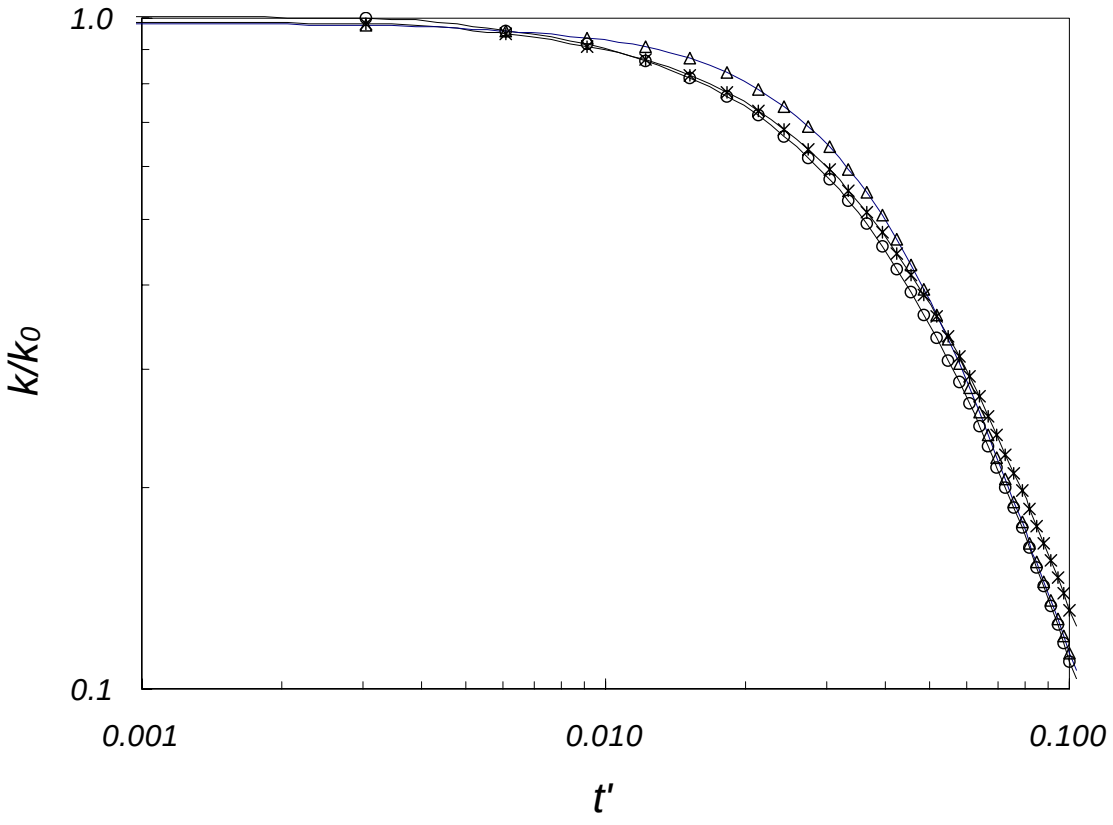

Fig. 26. Comparison of kinetic energy decay of 32^3 LBE-LES ($\circ$), 32^3 NS-LES ($*$) and 128^3 LBE-DNS ($\triangle$).

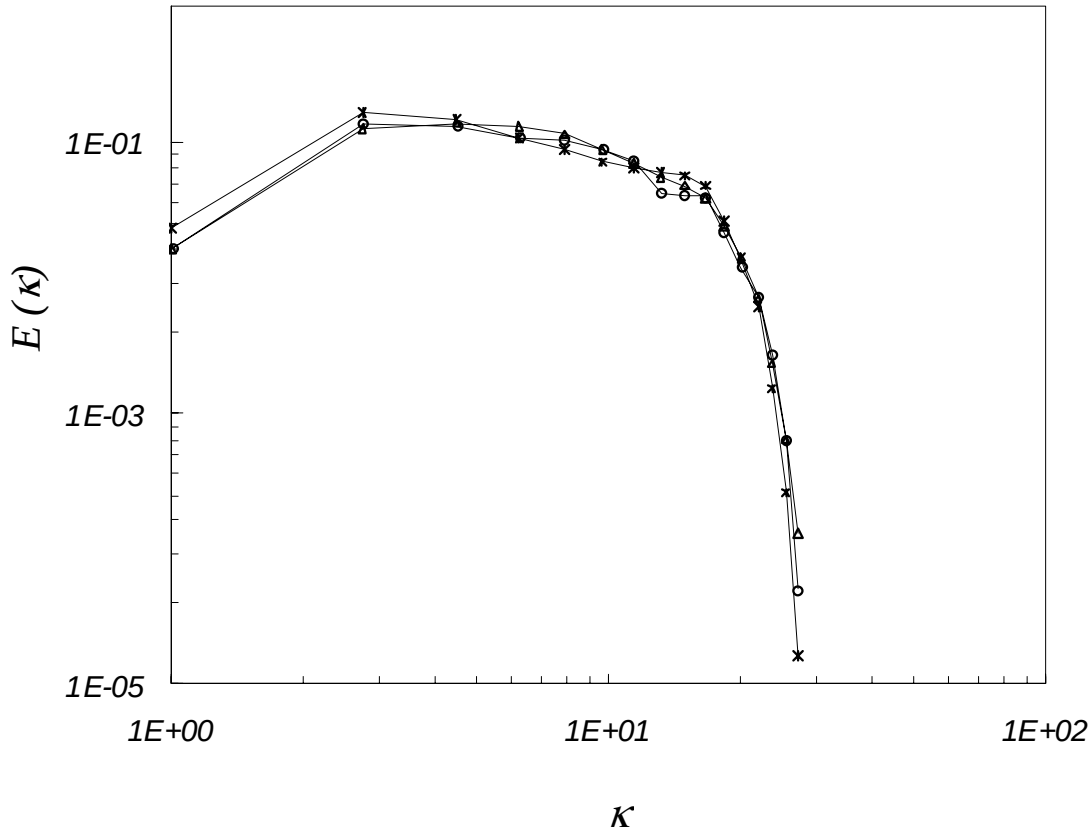

Fig. 27. Comparison of the energy spectra at $t' = 0.06079$ of 32^3 LBE-LES ($\circ$), 32^3 NS-LES ($*$) and 128^3 LBE-DNS ($\triangle$).

flow field $u_z(i,\, j,\, k = N/2,\, t')$ at three different times as shown in Fig. 28. By Comparing the LBE-LES results (left column) and the NS-LES results (right column) with the LBE-DNS results (center column), we observe that LBE-LES preserves the flow structure better than the corresponding NS-LES. The 32^3 LBE-DNS contours shown here are obtained by truncating the 128^3 LBE-DNS data.

E. Summary and conclusions

In this work we perform DNS and LES of the classical decaying HIT problem with and without reference frame rotation using the LBM. Three categories of simulations have been performed. First we conduct the direct numerical simulations by using the LBM. The well known power-law decay of the kinetic energy is reproduced. The decay exponents obtained in the LBE simulations are in good agreement with the results from experimental measurements and NS-DNS calculations. The low-wavenumber energy spectrum scaling depends on initial conditions. Both κ^4 and κ^2 scaling are obtained from appropriate initial conditions consistent with experimental data [67, 68]. The effect of rotation on turbulence, which is to suppress the spectral cascade, is also well captured.

Second, we conduct a comparative study of the LBE-LES and the LBE-DNS. Comparisons between 64^3, 32^3 LBE-LES and 128^3 LBE-DNS show that the large scale motion is well captured by LBE-LES. A smaller Smagorinsky constant, $C_{sm} = 0.1$, is demonstrated to achieve better performance in LBE-LES. By choosing appropriate Smagorinsky constant, even 32^3 can adequately capture large scale motions.

Finally we compare both the LBE-LES and NS-LES with with the corresponding DNS results. Our comparisons indicate that LBE-LES has better capability to preserve flow-field structure than NS-LES.

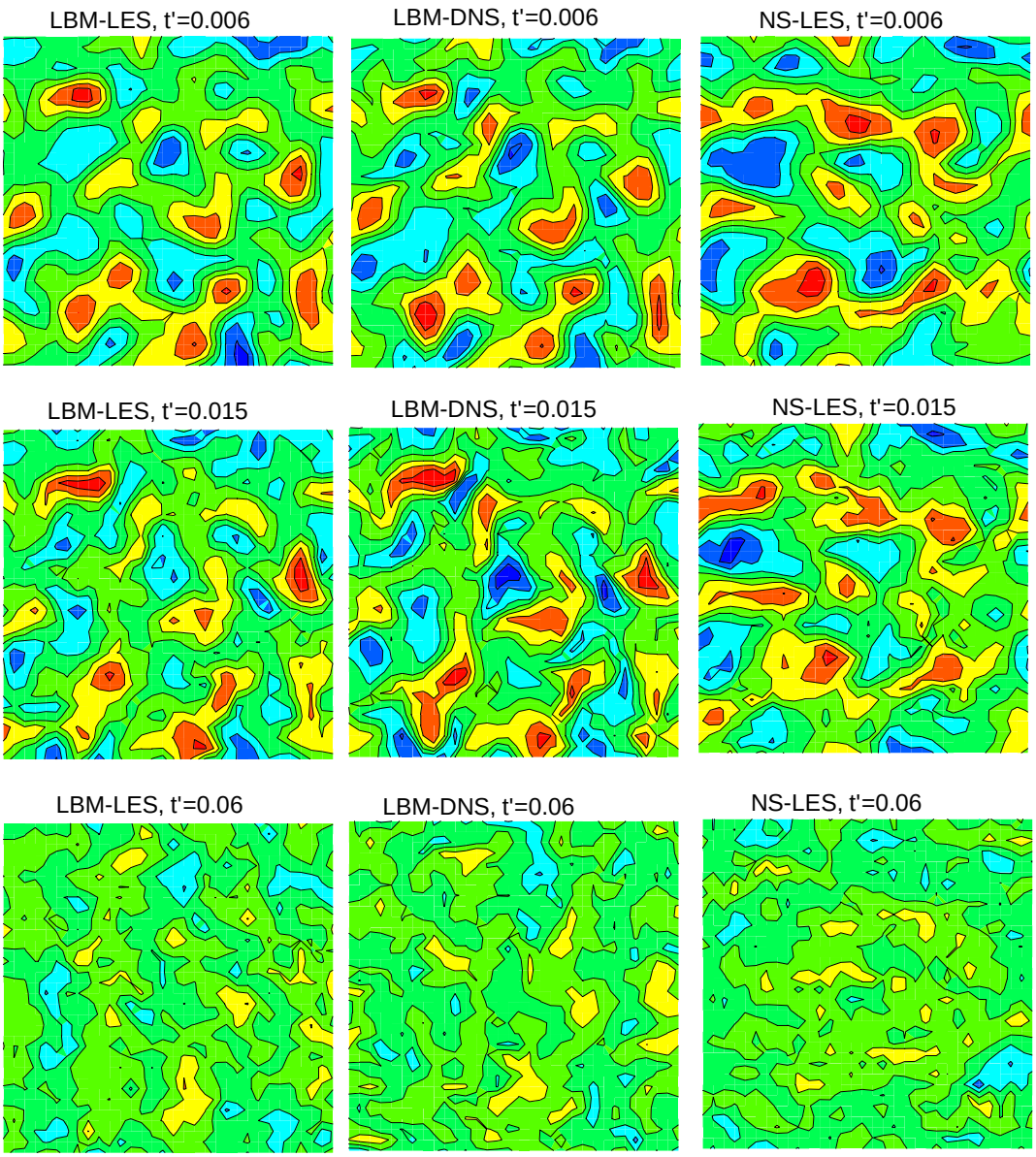

Fig. 28. Contours of the instantaneous flow field $u_z(i, j, k = N/2, t')$. The LBE-LES and NS-LES with a resolution of 32^3 compared to the LBE-DNS with a resolution of 128^3 at three different times. The 32^3 LBE-DNS contours shown here are obtained by truncating the 128^3 LBE-DNS data.

This work further establishes the LBM as a viable computational tool for turbulence simulations.

CHAPTER V

D3Q19 MULTI-RELAXATION-TIME LATTICE BOLTZMANN MODEL FOR LES OF TURBULENCE

A. Introduction

The lattice Boltzmann equation (LBE) [23, 90] is now well established as an accurate and efficient method for direct numerical simulations (DNS) for flow problems in recent years (cf. reviews [27–29] and references therein). However, the LBE method has not been thoroughly investigated in the area of large eddy simulations (LES). Although LES based on the LBE with Smagorinsky model was proposed early on [84, 91, 92], it is only recently the LBE-LES has been applied to some more realistic flows [86, 87, 93–95]. In this paper we will study a turbulent square jet in three dimensions (3D) with the LBE-LES.

In the LBE literature, the lattice Boltzmann equation with the single-relaxation-time (SRT) approximation or Bhatnagar-Gross-Krook (BGK) [36] model is the most popular one [25, 71], due to its simplicity. However, the lattice BGK (LBGK) model has limitations due to its numerical instability [39] and inaccuracy in boundary conditions [96]. Many of these limitations in the LBGK models can be overcome with the use of multiple-relaxation-time (MRT) model described in [37–40]. It has been clearly demonstrated that the LBE models with MRT collision operators have inherent advantages over their LBGK counterparts [37–40, 96]. The LBE model used in the present work is a three dimensional (3D) 19-velocity (D3Q19) model with MRT collision operator [38]. We apply the MRT-LBE method for LES of a square turbulent jet flow.

Turbulent jet emerging from a square exit has been previously studied by means

of experiments and Navier-Stokes based simulations [97]. In this work we study the turbulent square jet at $\mathrm{Re} = 184,000$ using LBM-LES. The remainder of this chapter is organized as follows. Section B briefly describes the formulation of MRT-LBE with the Smagorinsky eddy viscosity model for LES. Section C presents the numerical results for the turbulent square jet by using the LBE-LES and compares the LBE-LES results with experimental data. We close with a discussion in Section D. Appendices C and D discuss the calculation of the strain-rate tensor from nonequilibrium moments and the implementation tips of the D3Q19 MRT-LBE model.

B. D3Q19 MRT-LBE with Smagorinsky model

In the D3Q19 MRT-LBE model [38], the 19 discrete velocities are:

$$\vec{e}_\alpha = \begin{cases} (0,0,0), & \alpha = 0, \\ (\pm 1,0,0),\ (0,\pm 1,0),\ (0,0,\pm 1), & \alpha = 1\text{–}6, \\ (\pm 1,\pm 1,0),\ (\pm 1,0,\pm 1),\ (0,\pm 1,\pm 1), & \alpha = 7\text{–}18. \end{cases}$$

A set of velocity distribution functions $\{f_\alpha | \alpha = 0, 1, \cdots, 18\}$ are defined on each lattice node $\vec{x}$. For a MRT-LBE model with $Q(= 19)$ velocities, the collision is executed in the moment space $\mathbb{M} = \mathbb{R}^Q$, while the advection is done in the velocity space $\mathbb{V} = \mathbb{R}^Q$ [38]. The evolution equation for the MRT-LBE is:

$$\mathbf{f}(\vec{x} + \vec{e}\delta_t, t + \delta_t) - \mathbf{f}(\vec{x}, t) = \vec{\Omega}(\vec{x}, t) = -\mathsf{M}^{-1} \cdot \hat{\mathsf{S}} \cdot [\mathbf{m} - \mathbf{m}^{(eq)}], \tag{5.1}$$

where δt is the time step size and M is a $Q \times Q$ matrix which linearly transforms the distribution functions $\mathbf{f} \in \mathbb{V}$ to the velocity moments $\mathbf{m} \in \mathbb{M}$ via:

$$\mathbf{m} = \mathsf{M} \cdot \mathbf{f}, \qquad \mathbf{f} = \mathsf{M}^{-1} \cdot \mathbf{m}. \tag{5.2}$$

We use the bold-face symbols to denote column vectors as the following:

$$\mathbf{f}(\vec{x}+\vec{e}\delta_t, t+\delta_t) := (f_0(\vec{x}, t+\delta_t), \ldots, f_{18}(\vec{x}+\vec{e}_{18}\delta_t, t+\delta_t))^{\mathsf{T}},$$
$$\mathbf{f}(\vec{x}, t) := (f_0(\vec{x}, t), f_1(\vec{x}, t), \ldots, f_{18}(\vec{x}, t))^{\mathsf{T}},$$
$$\mathbf{m} := (m_0(\vec{x}, t), m_1(\vec{x}, t), \ldots, m_{18}(\vec{x}, t))^{\mathsf{T}},$$
$$\mathbf{m}^{(eq)} := (m_0^{(eq)}(\vec{x}, t), m_1^{(eq)}(\vec{x}, t), \ldots, m_{18}^{(eq)}(\vec{x}, t))^{\mathsf{T}},$$

where T is the transpose operator.

The 19 moments are arranged in the following order: $m_0 = \delta\rho$ is the density fluctuation, $m_1 = e$ is related to energy, $m_2 = \varepsilon$ is related to energy square, $m_{3,5,7} = j_{x,y,z}$ are components of the momentum $\vec{j} = (j_x, j_y, j_z) = \rho_0\vec{u}$, $m_{4,6,8} = q_{x,y,z}$ are related to components of the heat flux $\vec{q} = (q_x, q_y, q_z)$, $m_9 = 3p_{xx}$, $m_{11} = p_{ww}$ and $m_{13,14,15} = p_{xy,yz,zx}$ are related to the components of the symmetric and traceless strain-rate tensor, $m_{10} = 3\pi_{xx}$ and $m_{12} = \pi_{ww}$ are the fourth order moments, and $m_{16,17,18} = m_{x,y,z}$ are the third order moments [38]. The quantity ρ_0 is the mean density in the system, which is usually set to 1. The relaxation matrix $\hat{\mathsf{S}}$ is diagonal in the moment space $\mathbb{M}$:

$$\begin{aligned}\hat{\mathsf{S}} &= \mathrm{diag}(0, s_1, s_2, 0, s_4, 0, s_4, 0, s_4, s_9, s_2, s_9, s_2, s_9, s_9, s_9 s_{16}, s_{16}, s_{16}) \\ &= \mathrm{diag}(0, s_e, s_\varepsilon, 0, s_q, 0, s_q, 0, s_q, s_\nu, s_\pi, s_\nu, s_\pi, s_\nu, s_\nu, s_\nu, s_m, s_m, s_m). \end{aligned} \quad (5.3)$$

The equilibria of the moments, $\mathbf{m}^{(\mathrm{eq})}$, are the functions of the conserved moments, which are density ρ and flow velocity $\vec{u}$ for athermal fluids, *i.e.*, $\mathbf{m}^{(\mathrm{eq})}(\vec{x}, t) = \mathbf{m}^{(\mathrm{eq})}(\rho(\vec{x}, t), \vec{u}(\vec{x}, t))$. For the D3Q19 model, the equilibria for the non-conserved moments are given by [38, 40]:

$$m_1^{(eq)} = -11\delta\rho + \frac{19}{\rho_0}\vec{j}\cdot\vec{j}, \quad m_2^{(eq)} = \omega_\varepsilon\delta\rho + \frac{\omega_{\varepsilon j}}{\rho_0}\vec{j}\cdot\vec{j}, \quad (5.4a)$$

$$m_{4,6,8}^{(eq)} = -\frac{2}{3} j_{x,y,z}, \tag{5.4b}$$

$$m_{9}^{(eq)} = \frac{1}{\rho_0}(3j_x^2 - \vec{j}\cdot\vec{j}), \quad m_{11}^{(eq)} = \frac{1}{\rho_0}(j_y^2 - j_z^2), \tag{5.4c}$$

$$m_{10}^{(eq)} = \omega_{xx} m_9^{(\mathrm{eq})}, \quad m_{12}^{(eq)} = \omega_{xx} m_{11}^{(eq)}, \tag{5.4d}$$

$$m_{13}^{(eq)} = \frac{1}{\rho_0} j_x j_y, \quad m_{14}^{(eq)} = \frac{1}{\rho_0} j_y j_z, \quad m_{15}^{(eq)} = \frac{1}{\rho_0} j_z j_x, \tag{5.4e}$$

$$m_{16}^{(eq)} = m_{17}^{(eq)} = m_{18}^{(eq)} = 0. \tag{5.4f}$$

The parameters in the equilibria are chosen as the following to optimize the linear stability of the model: $\omega_\varepsilon = \omega_{xx} = 0$ and $\omega_{\varepsilon j} = -475/63$ [38]. The density fluctuation $\delta\rho$ instead of the total density ρ is used in m_0, $m_1^{(\mathrm{eq})}$ and $m_2^{(\mathrm{eq})}$ to reduce the numerical effects due to the round-off error [38].

The speed of sound in the model is $c_s = 1/\sqrt{3}$ in the lattice units of $\delta_x = \delta_t = 1$. And the viscosity is

$$\nu = \frac{1}{3}\left(\frac{1}{s_\nu} - \frac{1}{2}\right) c^2 \delta_t, \qquad c := \frac{\delta_x}{\delta_t}. \tag{5.5}$$

For LES, $\nu = \nu_0 + \nu_t$, where ν_0 and ν_t are the molecular viscosity and turbulent viscosity (or eddy viscosity), respectively. In the Smagorinsky model [2, 85], the eddy viscosity ν_t is determined from the filtered strain rate tensor $S_{\alpha\beta} = (\partial_\alpha u_\beta + \partial_\beta u_\alpha)/2$, a filter length scale Δ_x and the Smagorinsky constant C_S:

$$\nu_t = (C_S \Delta_x)^2 \bar{S}, \qquad \bar{S} := \sqrt{2\mathsf{S} : \mathsf{S}}. \tag{5.6}$$

In the LBE-LES with a uniform mesh, we set $\Delta_x = \delta_x = 1$ and $C_S = 0.1$. It should be noted that in the LBE-LES, all the quantities involved, *i.e.*, ρ, $\vec{u}$ and other moments of $\mathbf{f}$, are filtered quantities. Since we are only concerned with LBE-LES, we do not use different symbols to distinguish filtered quantities from the unfiltered ones. The calculation of $S_{\alpha\beta}$ is given in the Appendix C.

The non-slip boundary conditions in the LBE is realized by the bounce-back

boundary conditions [83]:

$$f_{\bar{\alpha}} = f_\alpha - 6w_\alpha \vec{j}_b \cdot \vec{e}_\alpha = f_\alpha - 6w_\alpha \rho_b \vec{u}_b \cdot \vec{e}_\alpha, \tag{5.7}$$

where $f_{\bar{\alpha}}$ is the distribution function of $\vec{e}_{\bar{\alpha}} := -\vec{e}_\alpha$, $w_0 = 1/3$, $w_{1-6} = 1/18$ and $w_{7-18} = 1/36$ correspond to the velocities of speed 0, 1, and $\sqrt{2}$, respectively; and ρ_b and $\vec{u}_b$ are respectively the density and velocity at the boundary where the bounce-back collision occurs. In what follows, we assume $\rho_b = \rho_0$.

In our simulations, the values for the relaxation rates other than s_ν are chosen as the following: $s_1 = 1.19$, $s_2 = s_{10} = 1.4$, $s_4 = 1.2$, $s_{16} = 1.98$. These values of s_α are obtained by optimizing the linear stability of the model [38]. The turbulent square jet has been studied experimentally and numerically [97].

Three points should be noted here about D3Q19 MRT-LBE-LES model:

1. Although the strain-rate tensor can be directly computed from non-equilibrium distribution functions in SRT-LBE and from non-equilibrium moments in MRT-LBE, the latter is more accurate. The reason is as follows: MRT-LBE introduces a moment representation that makes it possible to only pick up first-order modes to compute strain-rate tensor components while in SRT-LBE, all modes are not distinguishable.

2. As pointed out in reference [38], in MRT-LBE-DNS (corresponding to $\nu_t = 0$), SRT-LBE-DNS is recovered when set $\omega_\varepsilon = 3$, $\omega_{\varepsilon j} = -11/2$, $\omega_{xx} = -1/2$, and $s_i = 1/\tau$, $i = 1$, 2, 4, 9, and 16 in Eq. (5.3). The parameter τ is the single relaxation time. However this statement is not valid for MRT-LBE-LES because of the presence of eddy viscosity ν_t.

3. In order to gain efficient computation, all null terms in M, $\hat{\mathsf{S}}$, $\mathbf{m}$, and $\mathbf{m}^{(\mathbf{eq})}$ in the collision operator at the right-hand side of Eq. (5.1) should be excluded

in the iteration. Efficient implementation tips for the collision term of D3Q19 MRT-LBE-LES are given in Appendix D. By doing this, our MRT-LBE-LES computation is not expensive (only around 5% slower than its SRT counterparts in terms of the CPU time).

C. LBE-LES for square turbulent jet

In the experimental and numerical study of square jet by Quinn and Militzer [97], the jet is generated in a $76^2 \times 123$ (cm^3) settling chamber with a curved contraction connected to a square jet exit slot of area 4×4 (mm^2), from which the jet ejaculates into a $244^2 \times 366$ (cm^3) chamber. The mean streamwise velocity at the center of the slot exit u_0 is 60 (m/s). The Reynolds number based on the slot side dimension h (4 (mm)), u_0 and the viscosity of air is about 184,000.

Our focus in the present work is on the region near the jet exit. We use a uniform mesh of $100^2 \times 500$ for the jet chamber, with the jet exit slot area of 20^2. The equivalent diameter D_e ($D_e := 2h/\sqrt{\pi}$) of the jet exit is about 22.57. The coordinate system of the simulation is arranged as follows. The x, y and z axes are parallel to streamwise, spanwise, and vertical directions. The jet exit slot is situated at the center of plane $x = 0$. The periodic boundary conditions are applied in both y and z directions. We do not use nonslip wall boundary conditions in y and z directions because a higher resolution are required near the wall and it does not improve the result much. We impose a uniform velocity and density (pressure) profile for the jet at the exit: $u_0 = 0.1$ and $\rho_0 = 1.0$. Non-slip and fully developed-flow boundary conditions are applied at upstream and downstream boundaries, respectively. The molecular viscosity ν_0 is obtained from $\text{Re} = 184,000$, $u_0 = 0.1$ and $h = 20$ in lattice units. Initially, the system is set in a quiescent state of $\rho = \rho_0 = 1.0$ and $\vec{u} = 0.0$

except the jet exit area where $\vec{u} = u_0\vec{i}$. After an initial period of $1000T_0$ ($T_0 := D_e/u_0$), the statistics are gathered over a period of $1000T_0$ to obtain meaningful statistics.

In any jet study, three quantities are of primary interest: (a) the extent of jet penetration into the ambient; (b) the extent of jet spread or entrainment and (c) the evolution of the velocity profile of the jet. We now compare the simulation results with experimental data in these three categories.

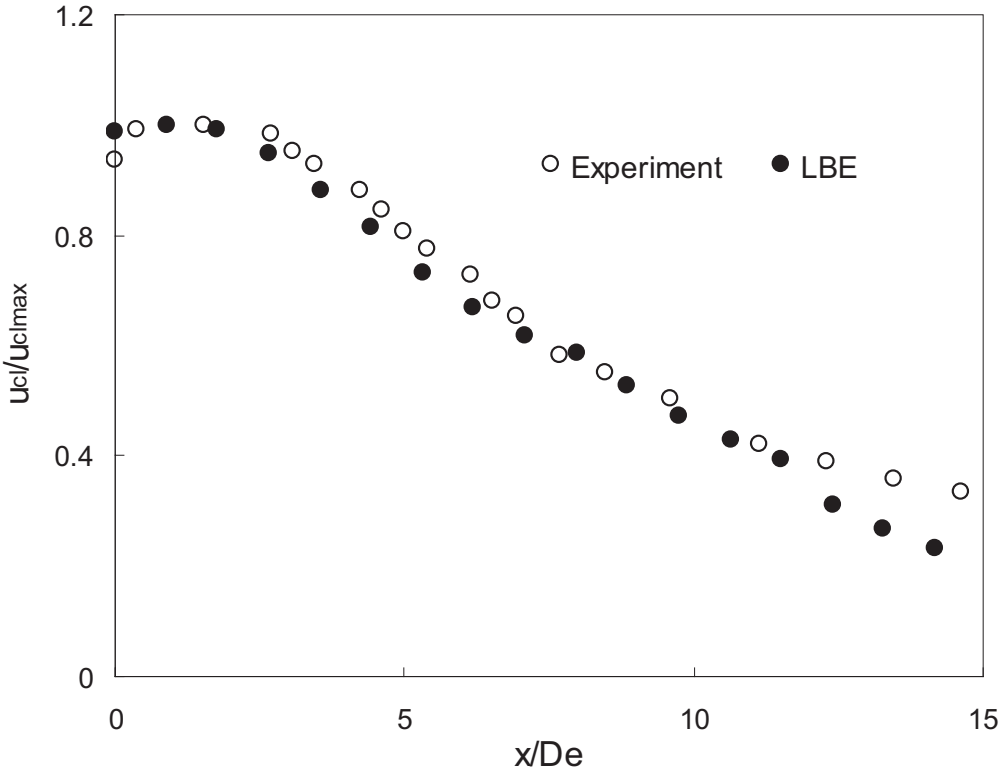

Fig. 29. Decay of the mean centerline streamwise velocity $u_{cl}(x)$ normalized by the maximum velocity u_{clmax}. The experimental data are taken from Fig. 3 in [97].

The extent of penetration is best quantified by the rate of decrease of the centerline velocity u_{cl} of the jet. Slow decrease of the centerline velocity would indicate

deeper penetration of the jet into the ambiance. The computed mean streamwise velocity evolution on the jet centerline is shown in Fig. 29 along with the experimental result of Quinn and Militzer [97]. The centerline velocity u_{cl} is normalized with u_{clmax} which is the maximum mean streamwise velocity along the jet centerline. The maximum centerline velocity u_{clmax} is not at the jet exit but at *vena contracta* located approximately at $x/D_e \approx 1.5$. The *vena contracta* effect is more pronounced in the experiment [97] than in the simulations. This is due to the difference in the jet exit velocity profile in the two cases. In the experiment the jet exit profile is not uniform due to the curvature in the streamlines as they emerge from the plenum chamber [97]. This profile strongly depends on the plenum chamber geometry and jet-exit details and can change significantly from one experiment to the other. Here, we do not attempt to address this issue and use a simple plug (uniform) jet-exit velocity profile. We focus on the agreement between the simulations and experiment in the region $2 \leq x/D_e \leq 15$. The results show that beyond the *vena contracta*, the mean streamwise velocity decreases monotonically. Although the *vena contracta* effect is not captured precisely, the LBE results agree with the experimental ones in the region of interest. To produce better agreement in the jet exit region $x/D_e < 2$, a better physical description of the plenum chamber and finer grid resolution are required.

Fig. 30 shows the near field spanwise profiles of the mean streamwise velocity on the xy plane at different streamwise locations $x/D_e = 0.28$, 2.688, 4.484 and 7.088. In Fig. 30, y_{hlf} is the velocity half-width of the jet in the spanwise (y) direction, which is the distance between the jet centerline and the location where the mean streamwise velocity is half that of the centerline. Very good agreement at all locations along streamwise direction between the experimental and LBE numerical results is seen. It is somewhat surprising that the simulations capture the experimental profile in the pre-*vena contracta* region (*e.g.*, $x/D_e = 0.28$) reasonably well. However, it should

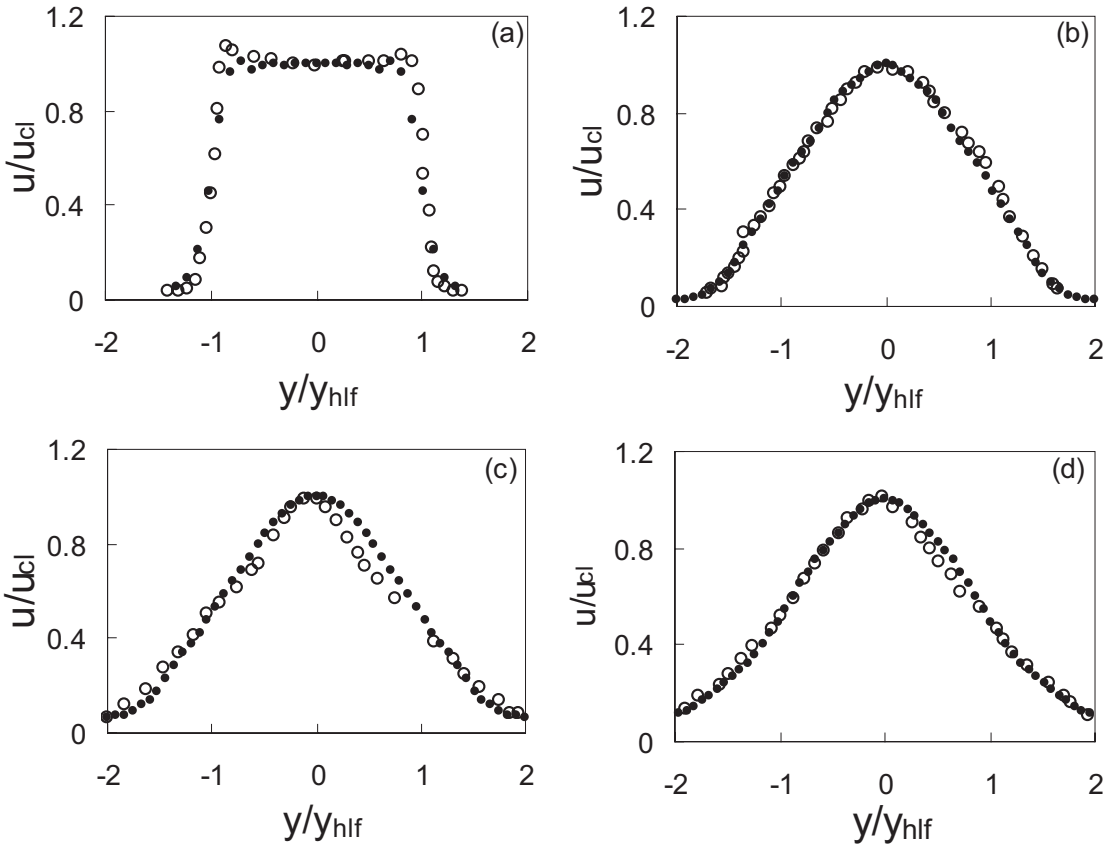

Fig. 30. Mean streamwise velocity profiles in the central xy plane ($z = 0$) at different locations. (a) $x/D_e = 0.28$, (b) $x/D_e = 2.658$, (c) $x/D_e = 4.484$ and (d) $x/D_e = 7.088$. Experimental data ($\circ$) are taken from Fig. 5 in [97].

be noted that the comparisons are for streamline velocity normalized by centerline velocity.

The next quantity of interest is the jet spread rate. One quantitative measure of the spread rate is the jet half-width y_{hlf}. Clearly, this will be a strong function of downstream location. Rapid increase of the jet half-width with down-stream distance would indicate rapid mixing or spreading. The computed variation of the half-width with down-stream distance along jet centerline is shown in Fig. 31. Also shown in the

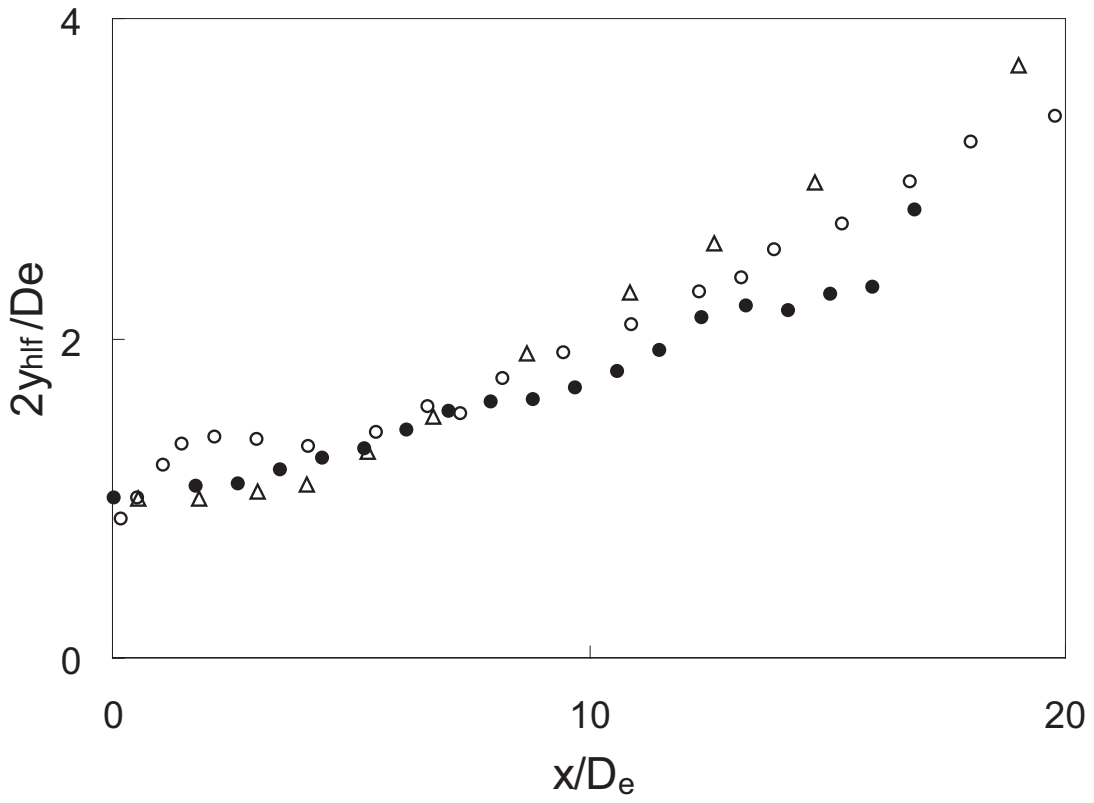

Fig. 31. Development of the jet half-width y_{hlf} along the jet centerline. Experimental ($\circ$) and Navier-Stokes ($\triangle$) data are taken from Fig. 6 in [97].

figure for comparison are the experimental data and Navier-Stokes numerical data of Quinn and Militze [97]. Again, the agreement between experimental data and numerical data from LBE simulation and Navier-Stokes computation is good except the very near region ($x/De < 4$). In this region, the experiment exhibits a spread-contract-spread behavior which is not well captured by either LBE or NS methods. It is not clear whether the observed experimental behavior is due to the *vena contracta* effect or a simpler consequence of the jet exit slot geometry. In either case, to capture this feature it requires a better representation of the plenum chamber flow and the

details of jet exist geometry, and finer resolution for the overall flow field.

D. Conclusions

In this work we present a preliminary investigation of the capability of the LBE-LES method for turbulent jet flows. We use the D3Q19 MRT-LBE model with the Smagorinsky eddy-viscosity model for subgrid turbulence closure. Numerical evaluation of MRT-LBE-LES is performed in a 3D turbulent square jet flow at $\mathrm{Re} = 184,000$. The LBE-LES results are compared with experimental data for the following quantities: the mean streamwise velocity, the spanwise profiles of mean streamwise velocity at different down-stream locations and the jet spread. Simulation results are in good agreement with available data. This investigation demonstrates that MRT-LBE is a viable method for LES of turbulent jet flows. Further studies of turbulent jets of different configurations are presented in Chapter VI.

CHAPTER VI

NEAR-FIELD TURBULENT MIXING SIMULATIONS OF RECTANGULAR JETS USING LATTICE BOLTZMANN METHOD

A. Introduction

Jets and plumes are omnipresent in nature and engineering applications. In recent years, special attention has been given to the case of jets emerging from non-circular exits, which are of great interest because of their enhanced entrainment and mixing properties relative to those of comparable axisymmetric jets (cf. [98] and references therein). Rectangular turbulent jet features prominently in technological applications in aerospace, chemical and mechanical engineering fields. Some of these applications are in smart-combustor propulsion units of both conventional and V/STOL aircraft, in the dispersion of pollutant effluents, and in boiler furnaces and gas-turbine plants of electric power utilities. RTJ combines the variable aspect ratio feature of elliptic jet with the corner (vertex) feature of square jet, which has attracted extensive interest in experimental investigations [97, 99–113].

In general, the mixing process in a jet shear layers occurs in two stages: initial bulk mixing or large-scale stirring and, subsequent small-scale mixing characterized by gradient steepening leading to enhanced molecular diffusion. The first stage is driven by the generation of large coherent structures that entrain large pockets of ambient fluid. Then, these large-scale fluctuations cascade down to the small scales creating steep gradients which accelerate mixing at the molecular level. Large-scale coherent structures, are intrinsic features of high Reynolds number mixing layer [114]. They are generally characterized by organized vorticity distributions. Active and passive control of jets in practical applications entail clear understanding of the dynamics

and topology of large-scale coherent structures. In particular, formation, interaction, merging, and breakdown of large-scale coherent structures in jets need investigation.

Experimental and analytical investigations [99, 100, 105] have shown that the flow field of RTJ may be subdivided into three main regions: (i) Potential core (PC) region where the axis velocity (u_{cl}) is close to the jet exit velocity in the core since the mixing which initiates at the jet boundaries has not permeated yet; (ii) Characteristic decay (CD) region where velocity profiles in the plane of the minor axis are found to be self-similar, whereas those in the plane of the major axis are nonsimilar, which leads to the pronounced axis-switching behavior. The axis velocity decays depending upon the jet exit configuration. In this region u_{cl} is proportional to x^{-n} with $n \simeq 1$; (iii) Axisymmetric decay (AD) region where the velocity field is axisymmetric irrespective of the exit geometry. AD region extends to infinity.

A unique feature of RTJ is the so-called saddle-back spanwise profile of mean streamwise velocity in the CD region. Saddle-back velocity profiles are clearly evident in the large AR RTJ flows, say $AR \geq 10$ [102, 104, 105, 109, 113]. In the case of small AR, Masters and Fotheringham[101] and Tsuchiya *et al.* [106] report their observations of saddle-back velocity profiles for $AR = 6.44$ and 5 in their experiments respectively. However, such saddle-shaped MSV profile is not evident in the experiment of Quinn [109] in which $AR = 5$. There is still no consensus on the formation mechanism of this kind of velocity distribution. Van Der Hegge Zijen [115] suggests that such a profile may be due to the superposition of a uniform stream with the flow due to a system of vortex rings representing the jet, while Tsuchiya *et al.* [106] suggests that the rapid growth of the saddle-back profiles might be due to a region where the mixing of the spanwise axis is retarded in comparison with that just on the lateral axis. However, more detailed study of the flow field is needed to clearly understand the origin of such profiles. Another striking feature of RTJ is called axis-

switching: the change in direction of the major axis of the jet. This behavior is most noticeable in low aspect ratio rectangular turbulent jets [101, 102, 106, 110]. According to Gutmark & Grinstein [98], axis-switching results from self-induced Biot-Savart deformation of vortex rings with non-uniform azimuthal curvature and interaction between azimuthal and streamwise vorticity.

Many analytical treatments of non-circular jets have been based on linear stability analysis [116–119]. However, the extent of literature on detailed numerical simulations of 3D jet flows is very limited. Most numerical simulations have been performed for round or planar jets. Much less computational data exist for non-circular jets. Early numerical attempts of RTJs include Grinstein [120], Miller *et al.* [121], and Wilson & Demuren [122] with emphasis on the vorticity dynamics in the near and mid-range fields. Quite recently, Rembold *et al.* [123] and Feiz *et al.* [124] performed DNS and LES of rectangular turbulent jets respectively to investigate velocity profiles. However these studies stop well short of addressing all pertinent issues.

The objectives of this work are twofold. (1) To systematically investigate the near-field turbulent mixing features of RTJs which are dominated by large coherent flow structures. The near-field consists of potential core and characteristic decay regions. (2) To further evaluate the capability of MRT-LBE model for LES of turbulence at sufficiently high Reynolds number. Emphasis is placed on the near-field flow statistics of RTJ flow and comparisons with experimental data qualitatively and quantitatively. Investigation of the detailed physics of the different phenomena will be performed in the future.

The remainder of this chapter is organized as follows. The flow fields and boundary conditions are described in Section B. Results of near-field mixing features and comparisons with experimental data are presented in Section C. Finally, we conclude

with a brief summary in Section D.

B. Coordinate system and boundary conditions

Instead of solving the usual continuum hydrodynamic equations, i.e. NS equations, the LBE method deals with the evolution of discretized single-particle velocity distribution functions. The local macroscopic quantities of density, momentum, and temperature are computed from these distribution functions. In what follows, we use the LES-MRT-LBE approach presented in Chapter V to perform all the simulations.

Fig. 32 shows the schematic configuration and coordinate system of the flow field. Exit velocity u_0, MSV on jet centerline u_{cl}, half-widths (y_{hlf} - lateral; z_{hlf} - spanwise), jet width w, height h, and three axis (x - streamwise, y - lateral, and z - spanwise) are denoted. In the LES-MRT-LBE model, we use $C_S = 0.1$.

The computational domain of the flow field is a $(W \times H \times L)$ channel. The inflow is a uniform velocity u_0 issuing from a $(w \times h)$ orifice exit. This configuration results in a jet with an aspect ratio of $AR \equiv w/h$ and an equivalent diameter of $De \equiv 2\sqrt{wh/\pi}$. The equivalent diameter is defined as the diameter of a round exit with the same exit area as the rectangular exit. Jet exit has been simplified as a plane. We apply the bounce-back boundary condition [83] at jet exit area ($x = 0$, $-w/2 \leq z \leq w/2$, and $-h/2 \leq y \leq h/2$). The remainder of the jet exit plane is treated as a solid wall. Fully developed boundary condition is applied at outflow($x = L$) and periodic boundary conditions in both lateral and spanwise directions. Initially, the velocity field is $\vec{u} = 0$ everywhere in the computational domain except the jet exit area where $\vec{u} = u_0\vec{i}$. The initial density field is uniform. After an initial run of $1000T_0(T_0 = De/u_0)$, the streamwise velocity and the square of streamwise velocity are averaged over time for another $1000T_0$ to get the mean streamwise velocity $u(x, y, z)$ and streamwise

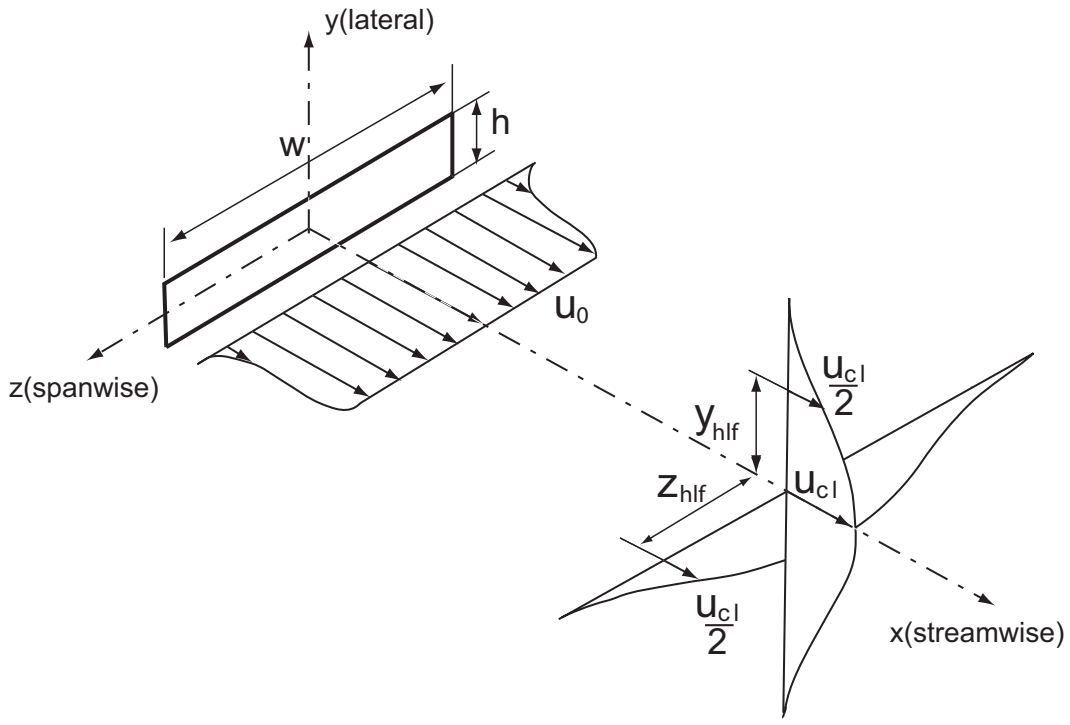

Fig. 32. Schematic configuration and coordinate system of the flow field. Adapted from Tsuchiya [106].

turbulence intensity $u'(x, y, z)$.

In order to compare our numerical results with published experimental data, we perform simulations of four jets. The details of the four jets and computational parameters are given in Table I and II.

C. Numerical results and discussions

In this section, we present results from our simulations and compare them with data wherever possible. The various experimental works present results in terms of different flow parameters and comparisons are made for all possible variables.

Table I. Low AR RTJs conducted in this work. units: length–(cm), velocity–(m/s)

Jet	u_0	w, h	AR	D_e	Re	W, H, L	Reference
I	60	$1, 1$	1	1.1	208000	$5, 5, 35$	Quinn & Militzer [97]
II	39	$1.5, 1$	1.5	1.4	36260	$5, 3.7, 28$	Tsuchiya *et al.* [106]
III	60	$2.6, 1.3$	2	2	128000	$8.8, 4.4, 30$	Quinn [108, 109]
IV	23	$5, 1$	5	2.5	35000	$10, 4.2, 64$	Tsuchiya *et al.* [106]

Table II. Computational grid sizes of the four jets.

Jet	Jet exit size	Full domain size
I	20×20	$100 \times 100 \times 700$
II	32×24	$150 \times 100 \times 700$
III	40×20	$160 \times 80 \times 700$
IV	70×14	$210 \times 80 \times 700$

1. Streamwise centerline velocity decay

The decay of the MSV along the jet centerline of all four jets is shown in Fig. 33. Vena Contracta effect triggered by the sharp-edged exit is evident in all cases as the centerline MSV increases initially. Beyond this region, the MSV decreases monotonically. The two near-field sub-regions PC and CD are identified in the figure. In the CD region, the decay exponents of all cases are around -1 which agrees qualitatively with experimental data. The faster decay of jet IV demonstrates that the mixing in the RTJ increases as the jet slot AR increases. Thus, in large AR jets, the ambient fluid is entrained into the core very rapidly.

Fig. 34 shows the LBM MSV decay of jet I along with experimental results

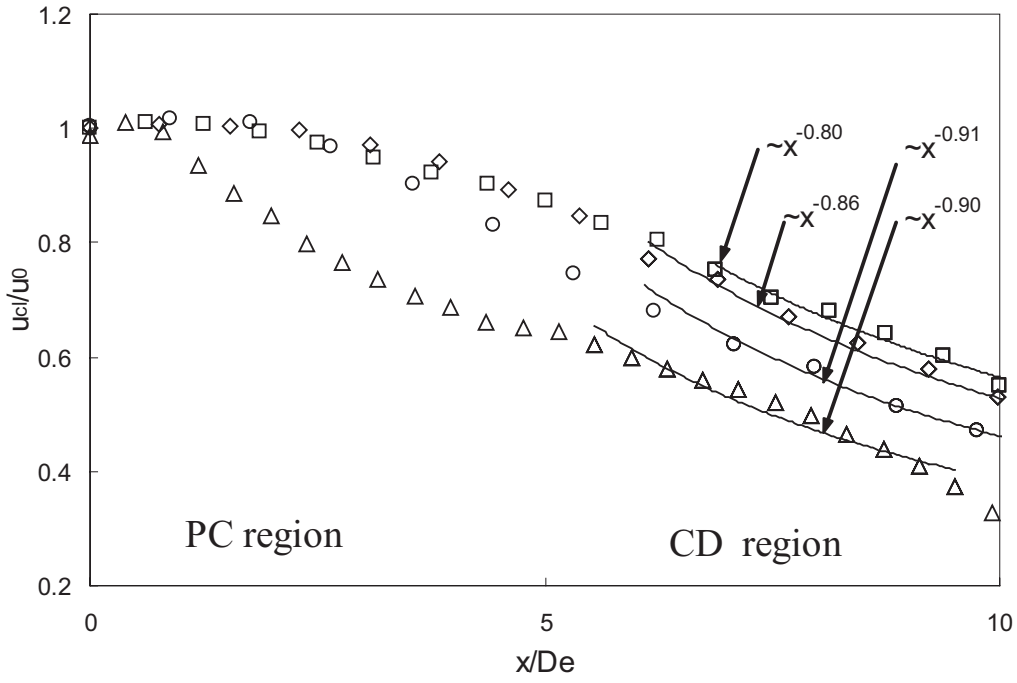

Fig. 33. Decay of the MSV along the jet centerline by LES-MRT-LBE simulations. □: jet III; △: jet IV.

of Quinn & Militzer [97] and duPlessis *et al.* [125]. It must be noted that the Quinn experiment uses nozzle-type exit whereas in the LBM simulation and duPlessis experiment the exit is of orifice-type. The Vena Contracta effect is more pronounced in the Quinn nozzle-exit experiment than LBM simulation or duPlessis measurement. Beyond this short region, the three datum sets are in qualitative agreement. The inverse mean velocity decays along the jet centerline for jet I and jet III are shown in Fig. 35. Here, u_{max} is the maximum MSV on the jet centerline typically located at Vena Contracta. The agreement between LBM and experiments is excellent. Also, the decay rates of the two jets show no distinguishable difference since the AR of the two jets are very close.

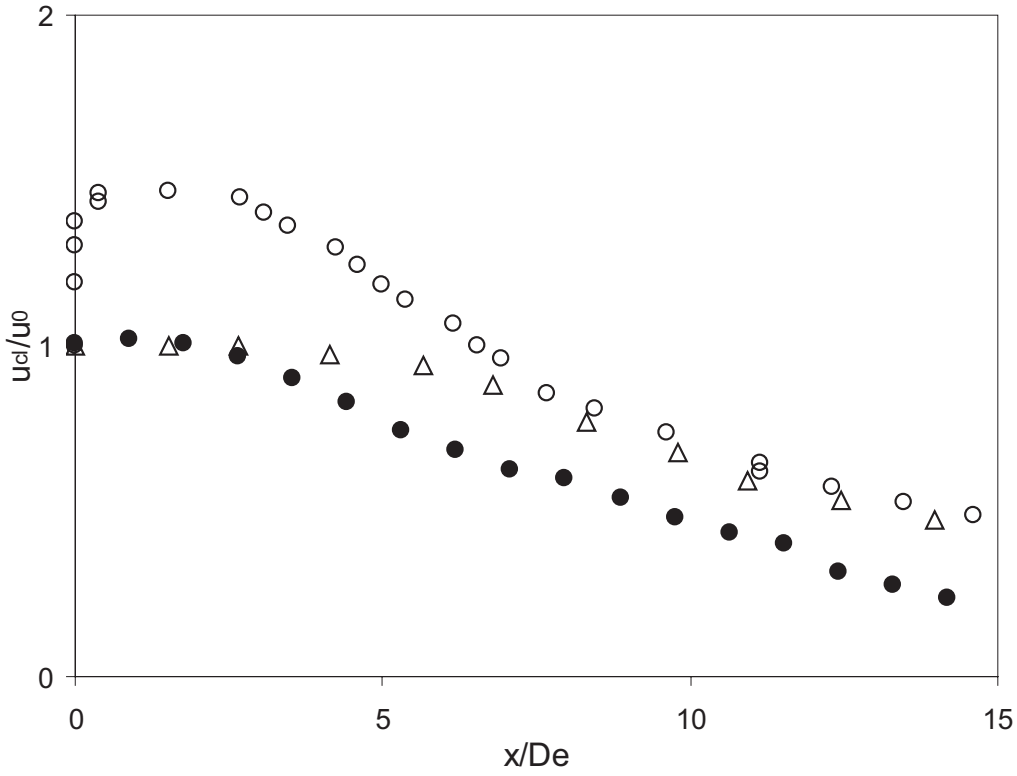

Fig. 34. Near-field MSV decay of jet I compared with experimental data. •: LES-MRT-LBE simulation result; ○: experimental data from Quinn [97]; △: experimental data from duPlessis [125].

2. Spanwise and lateral profiles of mean streamwise velocity

The spanwise and lateral distributions of MSV at various downstream locations for jet III and IV are presented in Fig. 36 and 37. The velocity profiles in spanwise and lateral directions are similar for III since the AR is not high enough. For $AR = 5$, the behavior in the two directions are dissimilar. The most striking features is the pronounced saddle-back spanwise velocity profile at $x = 2.8De$ (Fig. 37 (b)). In general, LES-MRT-LBE data are found to be in good quantitative agreement with corresponding experimental data.

It has been long known that saddle-back velocity profile occurs on the spanwise

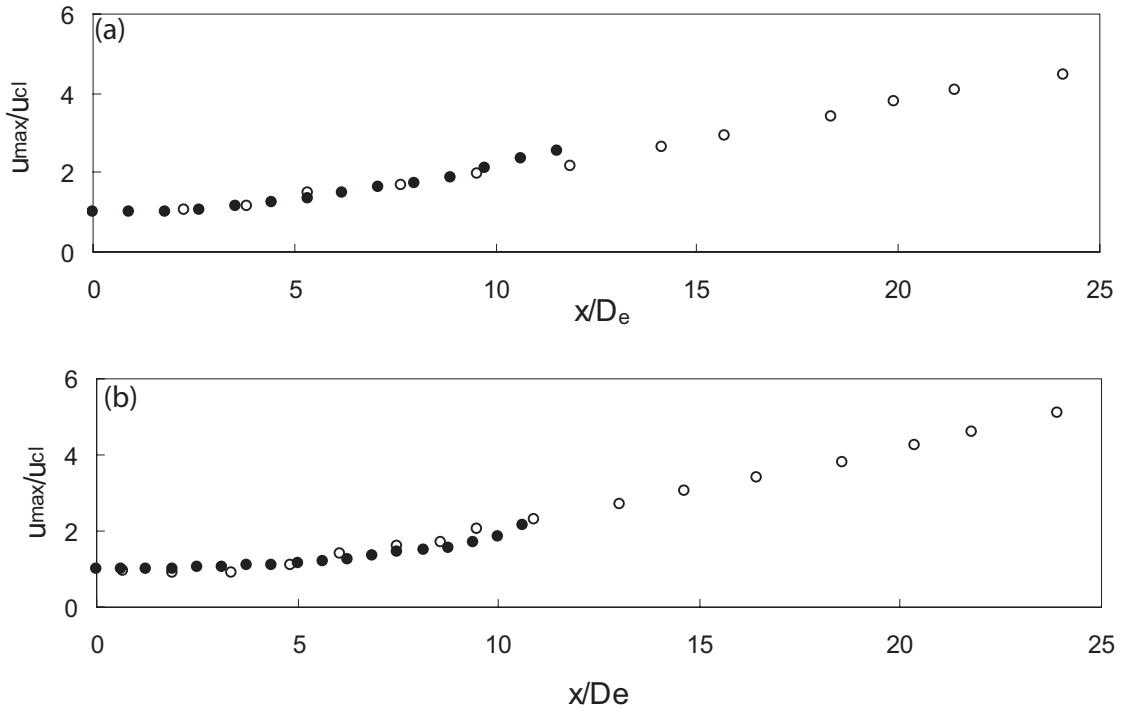

Fig. 35. Near-field inverse MSV decay along the jet centerline. (a) jet I •: LES-MRT-LBE simulation result; ○: experimental data from Quinn [97]. (b) jet III •: LES-MRT-LBE; ○: experimental data from Quinn [108].

axis for large AR, $AR \geq 10$ [101–105, 108–110, 113]. The saddle-back MSV profiles are characterized by steep gradients, which should give rise to high production of turbulence and thus facilitate effective mixing. There are few observations of saddle-back profiles in RTJs of smaller AR [101, 106]. According to our reference survey, $AR = 5$ [106] is the smallest AR in which the saddle-back profile is experimentally observed. However according to Quinn [109], saddle-back profiles are only evident for AR larger than 10. He claimed that "saddle-back profiles are barely noticeable in the AR 5 jet and are absent (or perhaps not detectable) in the aspect ratio 2 jet". Our numerical results show that saddle-back profile is not evident in $AR = 2$ jet (Fig. 36). We do observe a mild saddled-back profile in $AR = 5$ jet (Fig. 37 (b)). Our studies

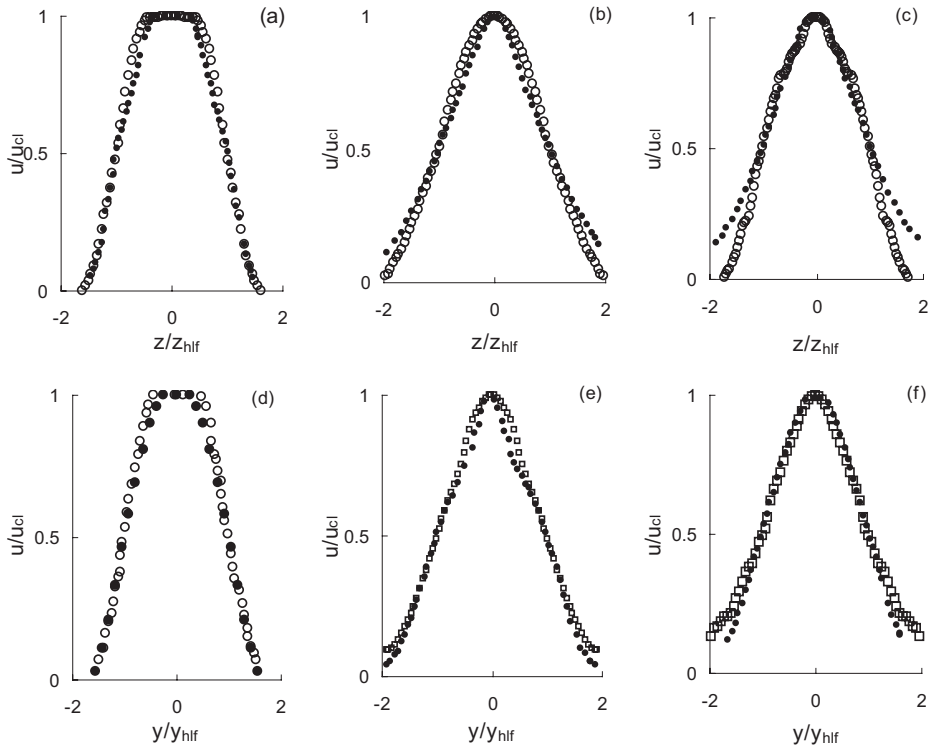

Fig. 36. Streamwise mean velocity profiles of jet III at different downstream locations along with experimental results for comparisons. Spanwise profiles: (a) x/De=2, (b) x/De=5, and (c) x/De=10; Lateral profiles: (d) x/De=2, (e) x/De=5, and (f) x/De=10. •: LES-MRT-LBE simulation result; ○: experimental data from Quinn [108].

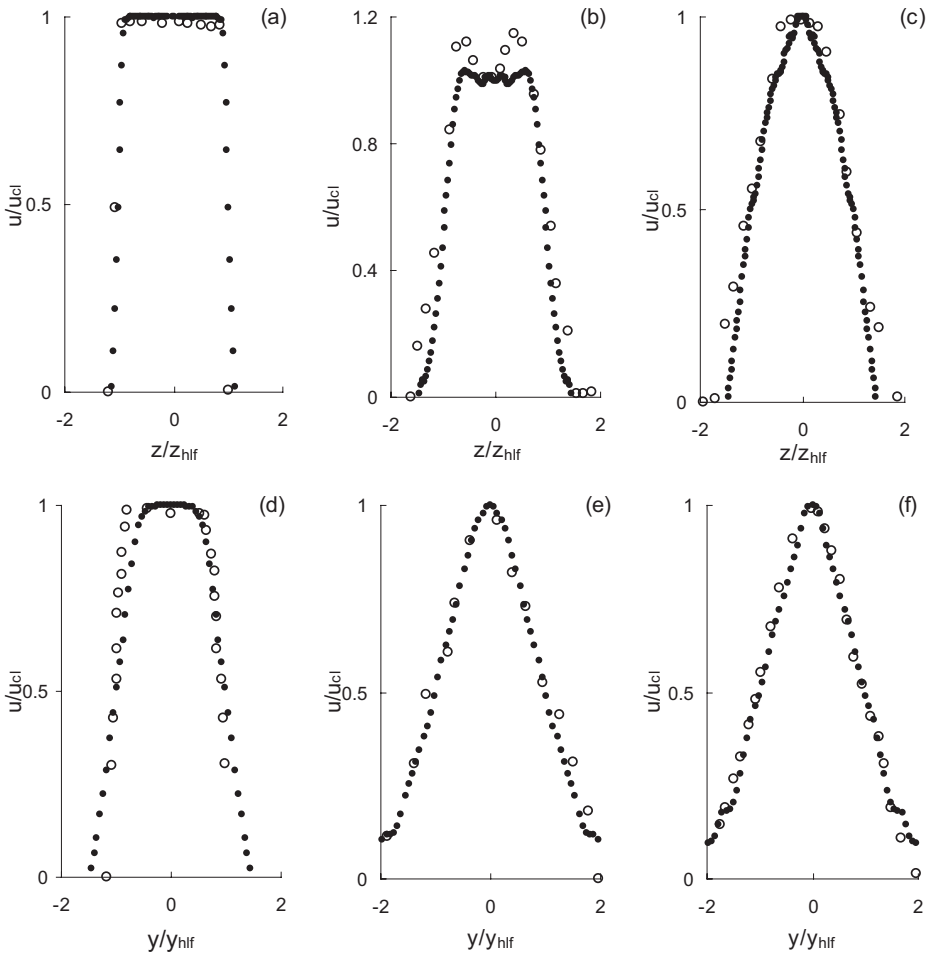

Fig. 37. Streamwise mean velocity profiles of jet IV at different downstream locations along with experimental results for comparisons. Spanwise profiles: (a) x/De=0.4, (b) x/De=2.8, and (c) x/De=5.2; Lateralwise profiles: (d) x/De=0.4, (e) x/De=2.8, and (f) x/De=5.2. •: LES-MRT-LBE simulation result; ○: experimental data from Tsuchiya [106].

also show that the occurrence of saddle-back may be influenced by factors such as jet-exit geometry, jet-exit velocity profile and boundary conditions.

3. Velocity contours and axis switching

The jet spread rates in the X-Y and X-Z planes are shown in Fig. 38–40 for jet II, III, and IV respectively. The spread rates are quantified in terms of lateral half-width

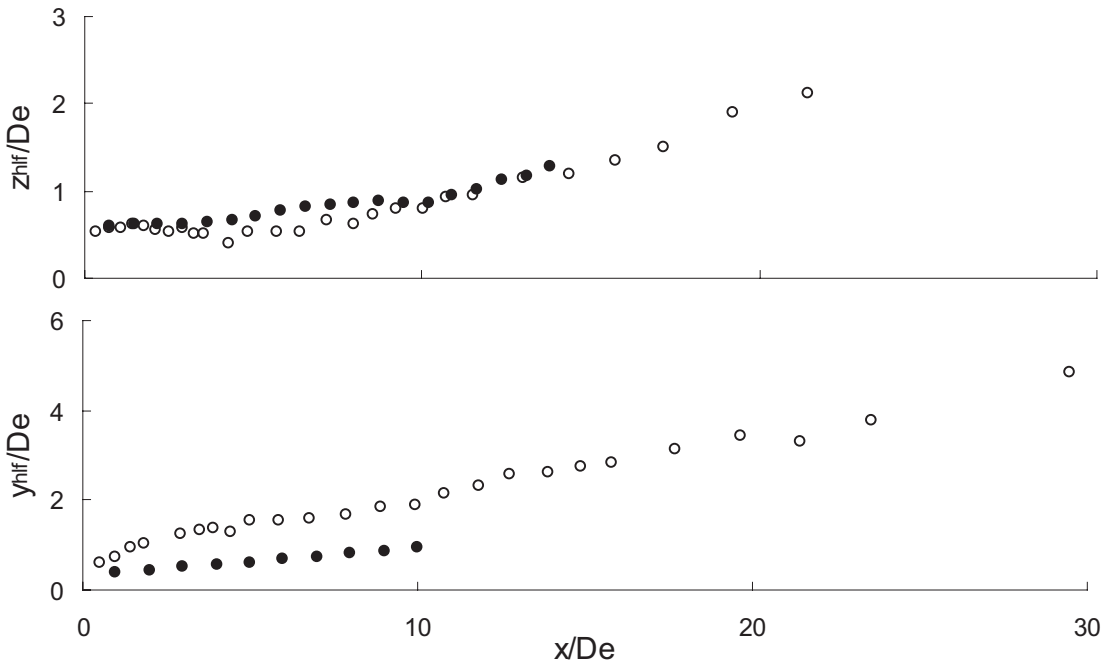

Fig. 38. Half-velocity width development of jet II •: LES-MRT-LBE simulation result; ○: experimental data from Tsuchiya [106].

(y_{hlf}) and spanwise half-width (z_{hlf}). Experiments indicate that while y_{hlf} increases monotonically, z_{hlf} stays nearly constant (even decreases) at early stages and then grows. The LBM results capture these effects adequately well. The difference in y_{hlf} and z_{hlf} growth rates leads to the phenomenon of axis-switching in the low AR jets. Axis-switching is of interest both from fundamental physical and practical application points of view. Beyond this region, the jet spreads in a similar fashion in

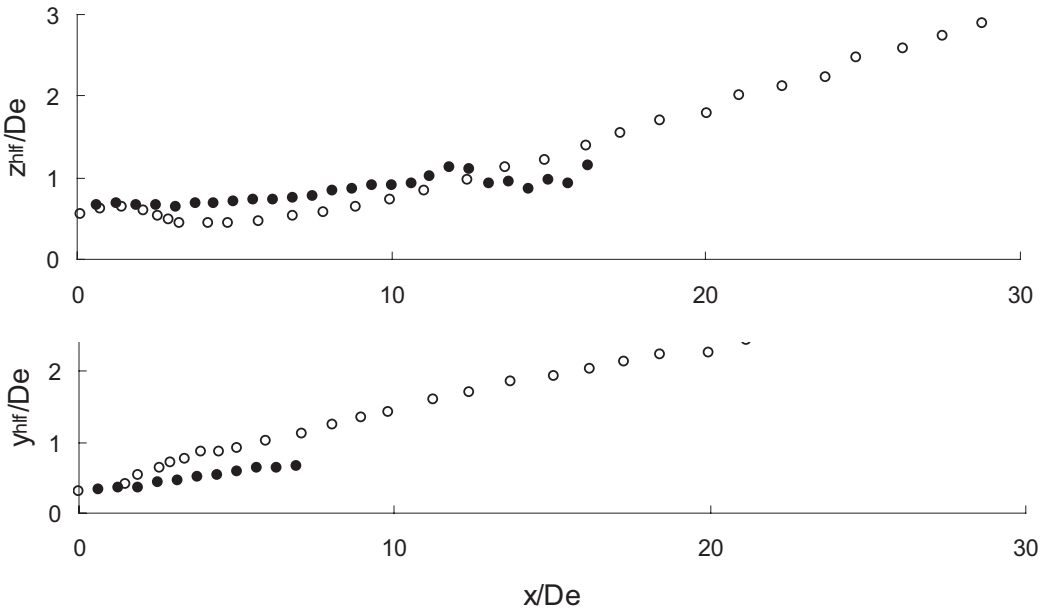

Fig. 39. Half-velocity width development of jet III •: LES-MRT-LBE simulation result; ○: experimental data from Quinn [109].

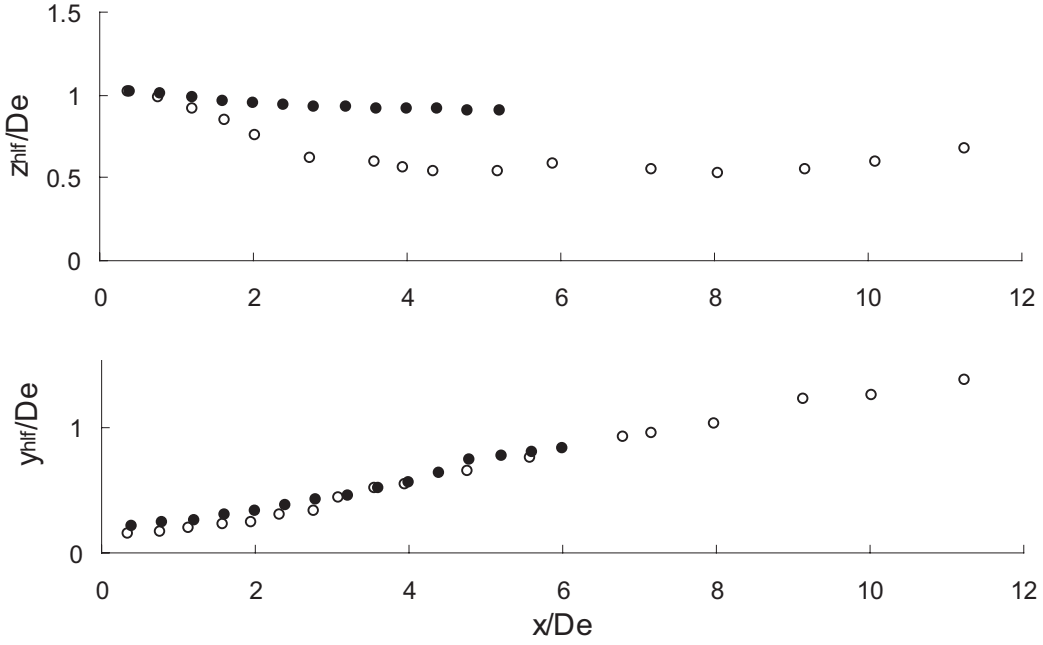

Fig. 40. Half-velocity width development of jet IV •: LES-MRT-LBE simulation result; ○: experimental data from Tsuchiya [106].

both directions. The axis-switching phenomenon is further investigated next.

In Fig. 41, the computed half-width velocity ($u/u_{cl} = 0.5$) contours of jet II at different x-locations are directly compared with experimental contours at approximately the same locations. The simulation mimics the deformation of the jet spread

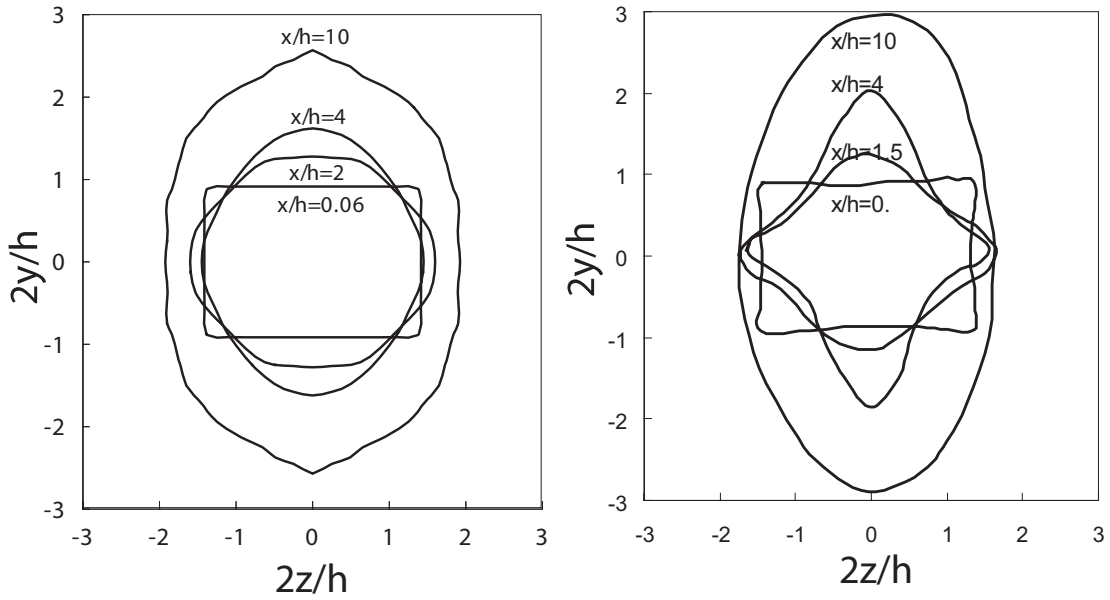

Fig. 41. Half-width contour of streamwise mean velocity ($u/u_{cl} = 0.5$) of jet II at different x-locations. h is the jet height. (a) experimental data from Tsuchiya [106]; (b) LES-MRT-LBE simulation result.

from the initial rectangular shape with major axis along spanwise through a rhombus-like shape at a short distance from the exit to an ellipse with major axis along lateral direction. This is a typical axis-switching phenomenon at relatively low AR (=1.5). For $AR = 2$, the axis-switching behavior is slightly different. Fig. 42 (a)–(d) show the MSV contour maps of jet III at 0.03De, 0.625De, 3.75De, and 6.25De respectively. The contour levels are 0.45, 0.575, 0.7, 0.825, 0.9. At location $x = 0.03De$ (Fig. 42 (a)), the MSV distribution is fairly uniform. The contours retain the rectangular shape of the jet exit (Fig.42 (b)). The initial close spacing of the contours

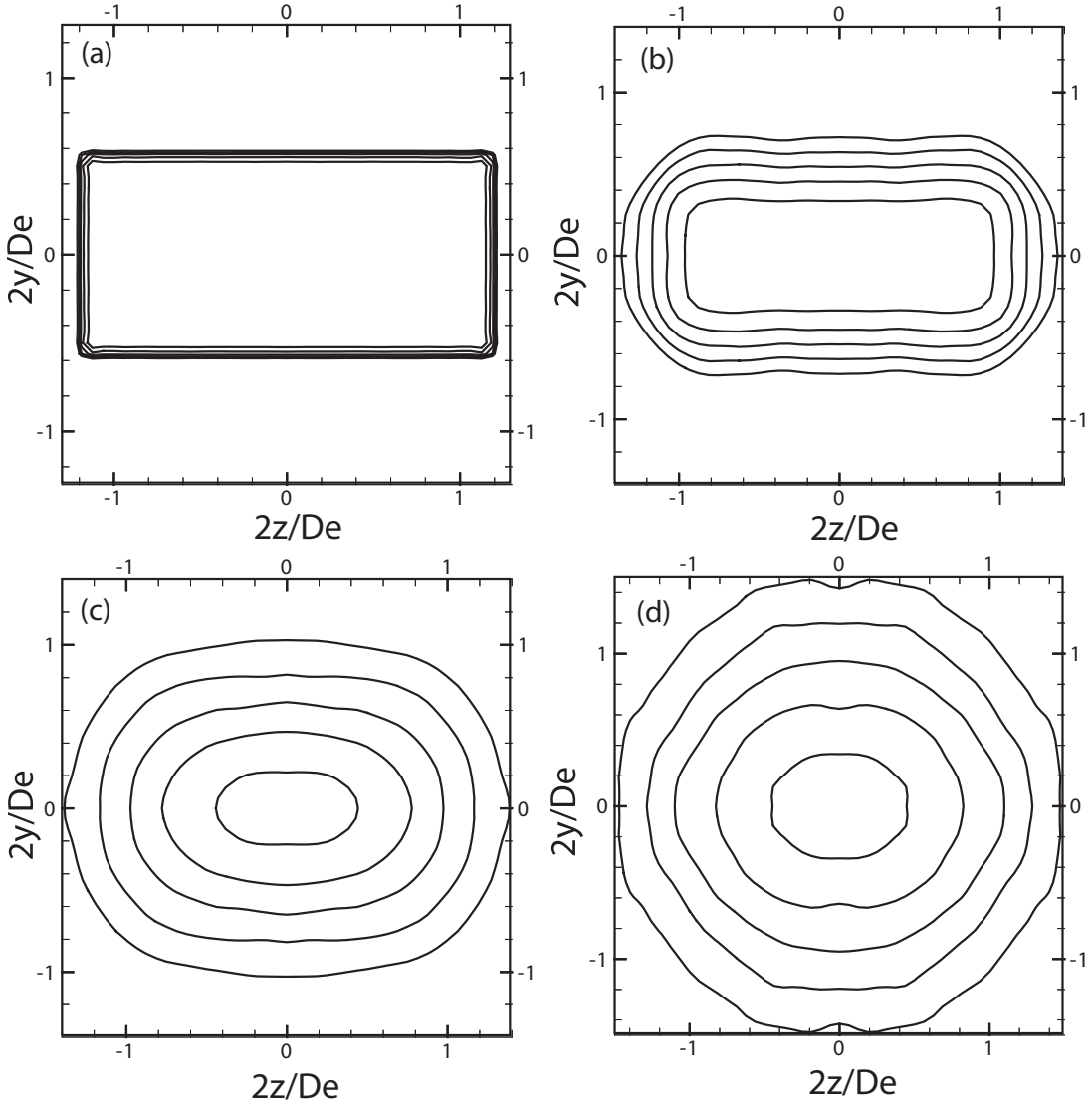

Fig. 42. Mean streamwise velocity (u/u_{cl}) contour development of jet III. (a) $x/De = 0.03$ (sharp rectangle), (b) $x/De = 0.625$ (rounded rectangle), (c) $x/De = 3.75$ (oval), and (d) $x/De = 6.25$ (circle).

implies high MSV gradients. At the intermediate streamwise station (Fig. 42 (c)), the contours take on an oval shape with wider spacing implying significant mixing. From location $x = 6.25De$ (Fig. 42 (d)) onwards, the contours are essentially circular. The change in shape of the MSV field from rectangular to oval to circular is a characteristic feature of RTJ flow with larger AR. In Quinn's experiments [110], this rectangular–oval–circular transition for $AR = 2$ has been clearly captured.

According to the instability analysis of Koshigoe & Tubis [117] for elliptic jets, the initial development of axis switching is characterized by the deformation of the coherent structures in the elliptic jet. The deformation of the structures and subsequent development of axis switching can be associated with the self-induction of asymmetrical distribution of vorticity in the elliptic jet, which causes differences in roll-up locations. According to Tam & Thiess [119], in high AR RTJs, the corner instability rapidly induces deformation of coherent structures causing them to evolve in an axisymmetric fashion further downstream. In future work, we will further investigate the physical mechanisms that cause axis switching.

4. Streamwise turbulence intensity

The streamwise turbulence intensity (u'/u_{cl}) of jets I, III and IV along the jet centerline is shown in Fig. 43 (a)–(c). Corresponding experimental results are also presented. In all three jets, u' increases rapidly near the jet exit (or Vena contracta) where large local shear leads to high values of turbulence production. The LES-MRT-LBE results are in reasonable qualitative agreement with experimental data. The spanwise profiles of the streamwise turbulence intensity of jet I at various streamwise locations are presented with experimental results in Fig. 44. Although the LES-MRT-LBE simulation captures the profile shapes at each location, the magnitudes of turbulence intensity are quantitatively different. The values of streamwise turbulence intensity

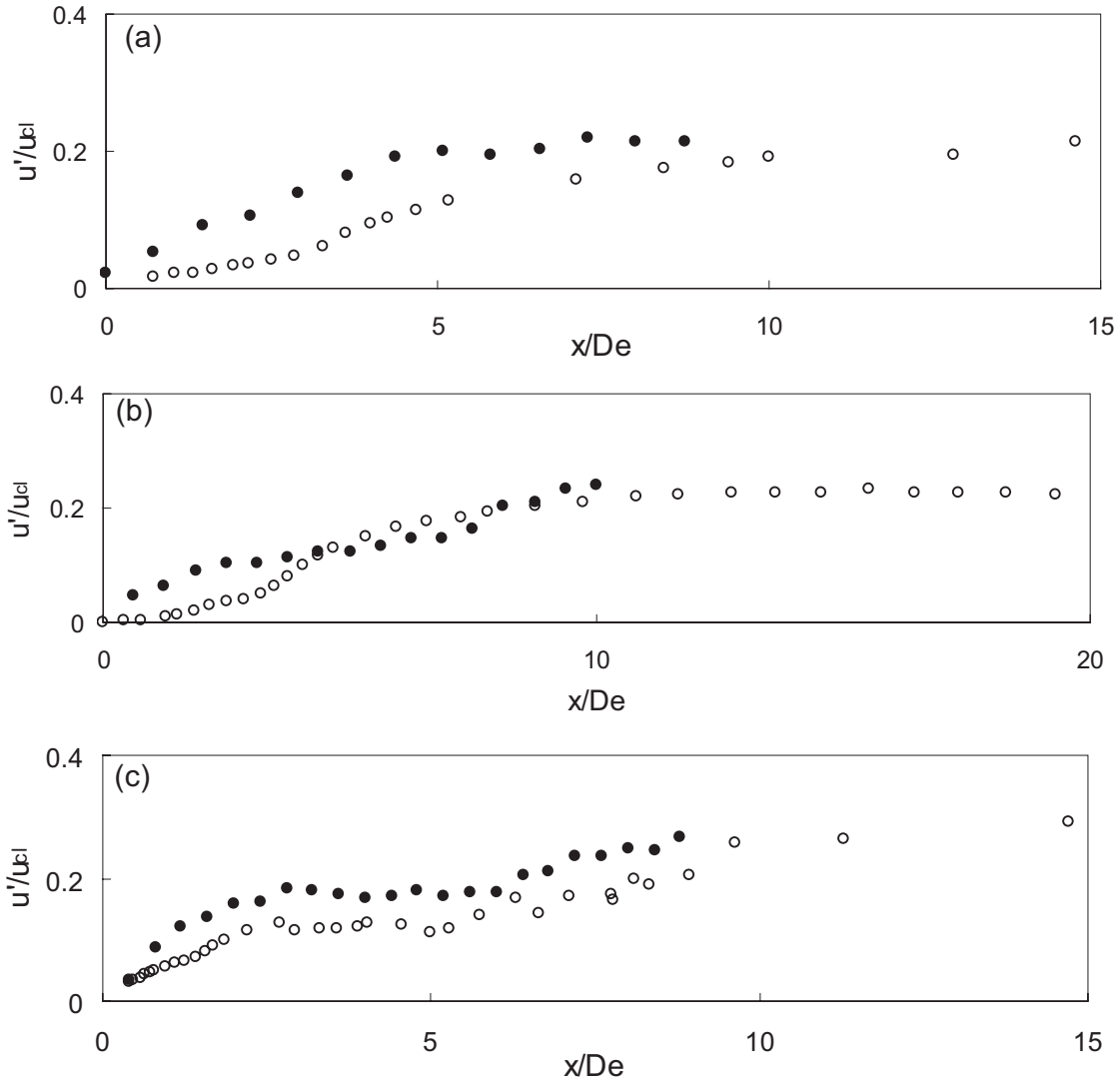

Fig. 43. Turbulent intensity distribution along jet centerline. (a) jet I, •: LES-MRT-LBE simulation result; ○: experimental data from Tsuchiya [106]. (b) jet III, •: LES-MRT-LBE simulation result; ○: experimental data from Quinn [109]; (c) jet IV, •: LES-MRT-LBE simulation result; ○: experimental data from Tsuchiya [106].

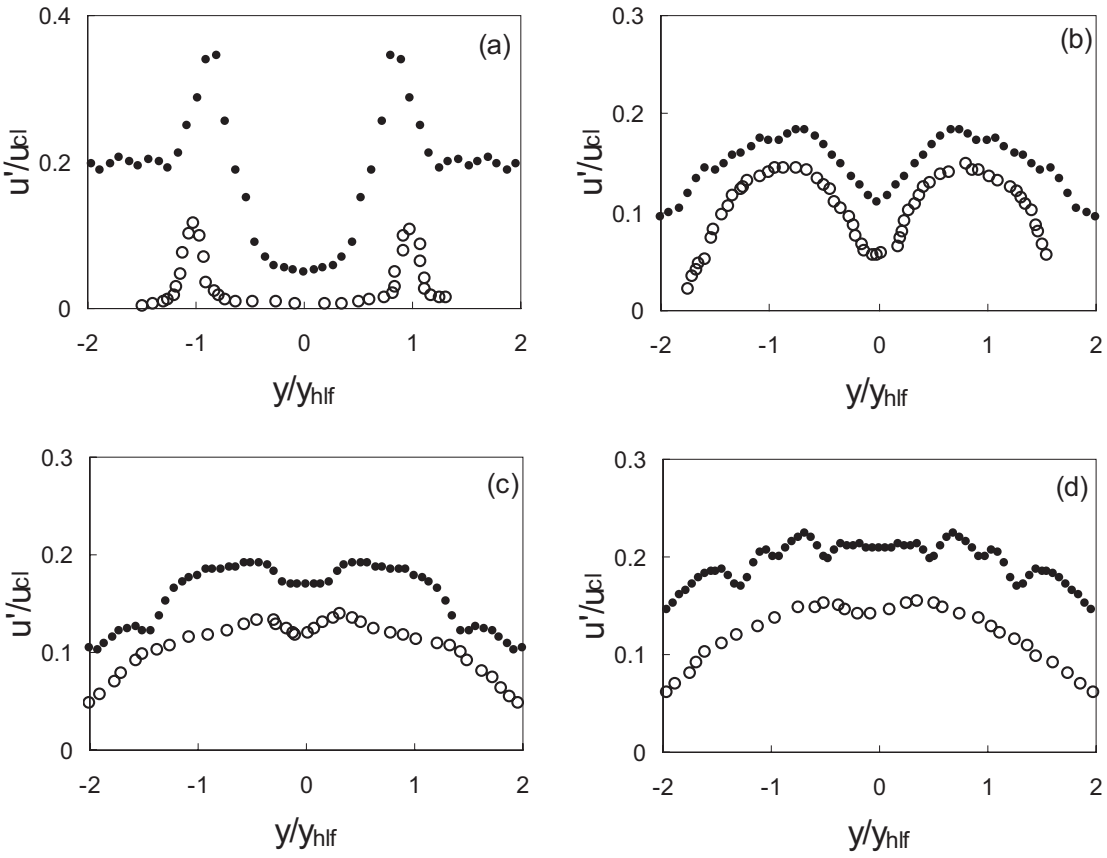

Fig. 44. Spanwise profiles of streamwise turbulence intensity of jet I at different downstream locations along with experimental results for comparisons. (a) x/De=0.28, (b) x/De=2.658, (c) x/De=4.484, and (d) x/De=7.088. •: LES-MRT-LBE simulation result; ○: experimental data from Quinn [97].

are systematically larger than those of experiments. This difference is amenable to a simple explanation. In each case, the turbulence intensity is normalized by the centerline velocity. As can be seen from previous results, the u_{cl} of LES-MRT-LBM tends to be smaller than the experimental values. Therefore, it is natural that the u'/u_{cl} ratio will be larger in LES-MRT-LBM than in experiments.

D. Conclusion

We numerically investigate the near-field turbulent mixing features of low AR rectangular jets using the novel LES-MRT-LBE computational tool. The near-field region is comprised of potential core and characteristic decay regions where mixing is driven by the large coherent structures. All four jet flows are of sufficiently high Reynolds numbers ranging from 35000 to 208000 based on equivalent diameter. Computed flow parameters include MSV, half-velocity width in both spanwise and lateral directions, and streamwise turbulence intensity. The well-known phenomena of RTJ flow, saddle-back velocity profile and axis-switching, are both captured. The decay exponent of MSV on the jet centerline in CD region is also computed. Several comparisons between LES-MRT-LBE and experimental data show quantitative or qualitative agreement in near-field region. It is also found that large AR jet mixes faster than low AR jet. In the case of low AR jet ($AR < 5$), the MSV profiles in spanwise and lateral directions are similar. When $AR > 5$, this similarity is broken: saddle-back velocity profiles occur on spanwise axis (the long axis) but not on lateral axis (short axis). As the jet spreads, low AR jets ($AR = 1.5$ and 2) develop axis-switching from spanwise to lateral axes.

Overall, this work clearly demonstrates that LES-MRT-LBE is a reliable tool to simulate near-field of RTJ flows.

CHAPTER VII

SUMMARY

In this dissertation, we have presented results from applications of lattice Boltzmann method (LBM) to turbulence, mixing and combustion. Both single-relaxation-time (SRT) approach and multiple-relaxation-time (MRT) approach are used and both direct numerical simulation (DNS) and large eddy simulation (LES) are conducted in this work. In order to evaluate and benchmark the efficiency and effectiveness of LBM for turbulent, mixing and reacting flows, we revisit a suite of classical problems:

- LES and DNS of decaying isotropic turbulence;
- DNS of decaying isotropic turbulence with frame rotation;
- Low aspect ratio rectangular turbulent jet flow;
- Non-premixed scalar mixing; and
- Premixed reacting flow.

We perform detailed comparisons with Navier-Stokes calculations and experimental data wherever available. Our inferences are:

- LBM-DNS captures the cascade physics and rotation effects in decaying turbulence very well. The low-wavenumber scaling of the spectra and the final-stage decay exponent obtained from LBM-DNS are in excellent agreement with experimental data and DNS-NS results.
- LBM-LES performs very well in decaying isotropic turbulence (without rotation).

- Comparison with NS-LES using identical closure models and same-order numerical schemes shows the LBM-LES results are somewhat superior.

- Computations of rectangular jet flows show that intricate features such as axis switching and saddle-back profiles are well reproduced by LBM-LES computations.

In conclusion, this work validates the use of LBM for turbulence, mixing, and reaction.

REFERENCES

[1] Tennekes H, Lumley JL. A first course in turbulence. Cambridge, MA: MIT Press; 1972.

[2] Pope SB. Turbulent flows. Cambridge: Cambridge University Press; 2000.

[3] Orszag SA. Numerical simulation of turbulent flows. In: Frost W, Moulden, TH, editors. Handbook of turbulence: fundamentals and applications, volume 1. New York: Plenum Press; 1977. p. 287–8.

[4] Moin P, Mahesh K. Direct numerical simulation: a tool in turbulence research. Annu Rev Fluid Mech 1998;30:539–578.

[5] Modi A. Direct numerical simulation of turbulent flows. Available on Internet (www.anirudh.net/courses/ae525/paper.ps), 1998.

[6] Lesieur M, Métais O. Newtrends in large-eddy simulations of turbulence. Annu Rev Fluid Mech 1996;28:4582.

[7] Moin P. Progress in large eddy simulation of turbulent flows. AIAA Paper 1997:970749.

[8] Speziale CG. Analytical methods for the development of Reynolds-stress closures in turbulence. Annu Rev Fluid Mech 1991;23:107-57.

[9] Ames WF. Numerical methods for partial differential equations. Boston: Academic Press; 1977.

[10] Morton KW, Mayers DF. Numerical solution of partial differential equations. Cambridge: Cambridge University Press; 1994.

[11] Bryan K. A numerical method for the study of the circulation of the world ocean. J Comput Phys 1969;4:347–76.

[12] Zienkiewicz OC, Taylor RL. Finite element method–basic formulation and linear problems (Vol 1). New York: McGraw-Hill; 1989.

[13] Zienkiewicz OC, Taylor RL. Finite element method–solid and fluid mechanics: dynamics and nonlinearity (Vol 2). New York: McGraw-Hill; 1991.

[14] Machenhauer B. The spectral method. In: Global atmospheric research programme (GRAP), editor. Numerical methods used in atmospheric models, Volume II. Geneva: World Meteorological Organization and International Council of Scientific Union; 1979. p.124–275.

[15] Bourke W. Spectral methods in global climate and weather prediction models. In: Schlesinger ME, editor. Physically based modeling and simulation of climate and climate change, part 1. Dordrecht: Kluwer Academic Publishers; 1988. p.169–220,

[16] Courant RK, Friedrichs K, Lewy H. Über die partiellen differentialgleichungen der mathematischen physik. Math Ann 1928;100:32–74.

[17] Philips NA. The general circulation of the stmosphere: a numerical experiment. Quat J Roy Meteor Soc 1956;82:124–64.

[18] Philips NA. An example of nonlinear computational instability. In: The atmosphere and the sea in motion, Rossby memorial volume. New York: Rockefeller Institute Press; 1959. p.501–4.

[19] Kadanoff L. On two levels. Phys Today 1986;39:79.

[20] Frisch U, Hasslacher B, Pomeau Y. Lattice-gas automata for the Navier-Stokes equations. Phys Rev Lett 1986;56:1505–8.

[21] Wolfram S. Cellular automaton fluids 1: basic theory. J Stat Phys 1986;45:471–526.

[22] d'Humiéres D, Lallemand P, Frisch U. Lattice gas model for 3D hydrodynamics. Europhys Lett 1986;2:29197.

[23] McNamara G, Zanetti G. Use of the Boltzmann equation to simulate lattice-gas automata. Phys Rev Lett 1988;61:2332–5.

[24] Chen H, Chen S, Matthaeus HW. Recovery of the Navier-Stokes equation using a lattice Boltzmann method. Phys Rev A 1992;45:R5339–42.

[25] Qian YH, d'Humières D, Lallemand P. Lattice BGK model for Navier-Stokes equation. Europhys Letts 2000;17:479–84.

[26] Chapmann S, Cowling TG. The mathematical theory of non-uniform gases (3rd ed.). London: Cambridge University Press; 1970.

[27] Chen S, Doolen G. Lattice Boltzmann method for fluid flows. Ann Rev Fluid Mech 1998;30:329–64.

[28] Luo LS. The lattice-gas and lattice Boltzmann methods: Past, present, and future. In: Wu JH, Zhu ZJ, editors. International Conference on Applied Computational Fluid Dynamics, Beijing. 2000. p.52–83.

[29] Yu D, Mei R, Luo LS, Shyy W. Viscous flow computations with the method of lattice Boltzmann equation. Prog Aerospace Sci 2003;39:329–67.

[30] Anderson J. Hypersonic and high temperature gas dynamics. New York: McGraw-Hill Inc.; 1989.

[31] Harris S. An introduction to the theory of the Boltzmann equation. New York: Holt Rinehart and Winston INC; 1970.

[32] Luo LS. Lattice-gas automata and lattice Boltzamnn eqautions for two-dimensional hydrodynamics. Ph D dissertation, Georgia Institute of Technology. 1993.

[33] Reichl LE. A modern course in statistical physics. New York: Edward Arnold (Publishing) LTD, 1980

[34] He X, Luo LS. A priori derivation of the lattice Boltzmann equation. Phys Rev E 1997;55:R6333–6.

[35] He X, Luo LS. Theory of the lattice Boltzmann method: from the Boltzmann equation to the lattice Boltzmann equation. Phys Rev E 1997;56:6811–7.

[36] Bhatnagar PL, Gross EP, Krook M. A model for collision processes in gases. I. Small amplitude processes in charged and neutral one-component systems. Phys Rev 1954;94:511–25.

[37] d'Humières D. 1992 Generalized lattice Boltzmann equations, In: Shizgal BD, Weaver DP, editors. Rarefied gas dynamics: theory and simulations. Prog Aeronaut Astronaut 1992;159:450–8.

[38] d'Humières D, Ginzburg I, Krafczyk M, Lallemand P, Luo LS. Multiple-relaxation-time lattice Boltzmann models in three-dimensions. Phi Trans Roy Soc Lon A 2002;360:437–51.

[39] Lallemand P, Luo LS. Theory of the lattice Boltzmann method: dispersion, dissipation, isotropy, Galilean invariance, and stability. Phys Rev E 2000;61:6546–62.

[40] Lallemand P, Luo LS. Theory of the lattice Boltzmann method: acoustic and thermal properties in two and three dimensions. Phy Rev E 2003;68:036706-1–25.

[41] Yu H, Luo LS, Girimaji SS. Scalar mixing and chemical reaction simulations using lattice Boltzmann method. Int J Computat Eng Sci 2002;3:73–87.

[42] Doolen GD, editor. Lattice gas methods for partial differential equations. New York: Addison-Wesley; 1990.

[43] Benzi R, Succi S, Vergassola M. The lattice Boltzmann equation: theory and applications. Phys Rep 1922;222:145–97.

[44] Shan X, He X. Discretization of the velocity space in the solution of the Boltzmann equation. Phys Rev Lett 1998;80:65–8.

[45] Wolf-Gladrow D. Lattice-gas cellular automata and lattice Boltzmann models. Heidelberg: Springer-Verlag; 2000.

[46] Junk M. Kinetic schemes in the case of low Mach numbers. J Comp Phys 1999;151:947–68.

[47] Junk M, Klar A. Discretizations for the incompressible Navier-stokes equations based on the lattice Boltzmann method. SIAM J Sci Comp 2000;22:1–19.

[48] Shan X, Chen H. Lattice Boltzmann model for simulating flows with multiple phases and components. Phys Rev E 1993;47:1815–9.

[49] Shan X, Chen H. Simulation of nonideal gases and liquid-gas phase transitions by the lattice Boltzmann equation. Phys Rev E 1994;49:2941–8.

[50] Shan X. Doolen G. Multicomponent lattice-Boltzmann model with interparticle interaction. J Stat Phys 1995;81:379–93.

[51] Shan X, Doolen G. Diffusion in a multicomponent lattice Boltzmann equation model. Phys Rev E 1996;54:3614–20.

[52] Yu H, Zhao K. A new lattice Boltzmann model for two-phase fluid. Chin Phys lett 1999;16:271–2.

[53] Luo LS, Girimaji SS. Lattice Boltzmann model for binary mixtures. Phys Rev E 2002;66:035301-1–4.

[54] Luo LS, Girimaji SS. Theory of the lattice Boltzmann method: two-fluid model for binary mixtures. Phys Rev E 2003;67:036302-1–11.

[55] Yamamoto K, He X, Doolen GD. Simulation of combustion field with lattice Boltzmann method. J Stat Phys 2002;107:367–83.

[56] Eswaran V, Pope SB. Direct numerical simulations of the turbulent mixing of a passive scalar. Phys Fluids 1988;31:506–20.

[57] Yamaoka I, Tsuji H. 1982 Twentieth symposium (international) combustion. Pittsburgh: The Combustion Institute; 1982.

[58] Ginzburg I, Steiner K. Lattice Boltzmann model for free-surface flow and its application to filling process in casting. J Comput Phys 2003;185:61–99.

[59] Clark TT. A numerical study of the statistics of a two-dimensional Rayleigh-Taylor mixing layer. Phys Fluids 2003;15:2413–23.

[60] Pan C, Hilpert M, Miller C. Lattice Boltzmann simulation of two-phase flow in porous media. Water Resou Resea 2004;40:W01501.

[61] Giraud L, d'Humières D, Lallemand P. 1998 A lattice Boltzmann model for Jeffreys viscoelastic fluid. Europhys Lett 1998;42:625–36.

[62] Lallemand P, d'Hmières D, Luo LS, Rubinstein R. Theory of the lattice Boltzmann method: three-dimensional model for linear viscoelastic fluids. Phys Rev E 2003b;67:021203-1–19.

[63] Ladd AJC, Verberg R. Lattice-Boltzmann simulations of particle-fluid suspensions. J Stat Phys 2001;104:1191–251.

[64] Qi D, Luo LS, Aravamuthan R, Strieder W. Lateral migration and orientation of elliptical particles in Poiseuille flows. J Stat Phys 2002;107:101–20.

[65] Qi D, Luo LS. Rotational and orientational behaviour of a three-dimensional spheroidal particles in Couette flow. J Fluid Mech 2003;477:201–13.

[66] Orszag SA, Patterson GS. Numerical simulation of three-dimensional homogeneous isotopic turbulence. Phys Rev Lett 1972;28:76–9.

[67] Huang MJ, Leonard A. Power-law decay of homogeneous turbulence at low Reynolds numbers. Phys Fluids 1994;6:3765–75.

[68] Mansour NN, Wray AA. Decay of isotropic turbulence at low Reynolds number. Phys Fluids 1994;6:808–14.

[69] Samtaney R, Pullin DI, Kosović B. Direct numerical simulation of decaying compressible turbulence and shocklet statistics. Phys Fluids 2001;13:1415–30.

[70] Ossia S, Lesieur, M. Energy backscatter in large-eddy simulations of three-dimensional incompressible isotropic turbulence. J Turb 2000;1(No 10):1–11.

[71] Chen S, Wang Z, Shan X, Doolen GD. Lattice Boltzmann computational fluid dynamics in three dimensions. J Stat Phys 1992;68:379–400.

[72] Benzi R, Struglia MV, Tripiccione R. Extended self-similarity in numerical simulations of three-dimensional anisotropic turbulence. Phys Rev E 1996;53:R5565–8.

[73] Luo LS, Wang LP, Qi D. Applications of the lattice Boltzmann method to complex and turbulent flows. In: Breuer M, Durst F, Zenger C, editors. High performance scientific and engineering computing, Lecture Notes in Computer Science and Engineering Vol. 21. Berlin: Springer. 2002. p. 123–30.

[74] Mohamed MS, LaRue JC. The decay power law in grid-generated turbulence. J Fluid Mech 1990;219:195–214.

[75] Rotta JC. Turbulente strömungen. Stuttgart: Teubner; 1972.

[76] Loitsyansky LG. Some basic laws for isotopic turbulent flows, Moscow Centr Aero Hydrodyn Inst Rep No, 1939. p. 440–55. [NACA Tech. Memo. 1079 (1939)].

[77] Kolmogorov AN. Decay of isotropic turbulence in incompressible viscous fluids. Dokl Akad Nauk SSSR 1941;31:299–303.

[78] Birkhoff G. Fourier synthesis of homogeneous turbulence. Comm Pure Appl Math 1954;7:19–35.

[79] Saffman PG. The large-scale structure of homogeneous turbulence. J Fluid Mech 1967;27:581–91.

[80] Oberlack M. On the decay exponent of isotropic turbulence. Proc. Appl Math Mech 2002;1:294–311.

[81] Smith MR, Donnelly RJ, Goldenfeld N, Vinen WF. Decay of vorticity in homogeneous turbulence. Phys Rev Lett 1993;71:2583–2586.

[82] He X, Luo LS. Lattice Boltzmann model for the incompressible Navier-Stokes equation. J Stat Phys 1997;88:927–44.

[83] Luo LS. Theory of the lattice Boltzmann method: lattice Boltzmann models for nonideal gases. Phys Rev E 2000;62:4982–96.

[84] Hou S, Sterling J, Chen S, Doolen GD. A lattice Boltzmann subgrid model for high Reynolds number flows. In: Lawniczak AT, Kapral R, editors. Pattern formation and lattice gas automata, Fields Inst Comm Vol.6. Providence: AMS.; 1996. p.151–66.

[85] Smagorinsky J. General circulation experiments with the primitive equations: I.The basic equations. Mon Weather Rev 1963;91:99–164.

[86] Derksen JJ, Van den Akker HEA. Simulation of vortex core precession in a reverse-flow cyclone. AIChE J 2000;46:1317-31.

[87] Krafczyk M, Tölke J, Luo LS. Large-eddy simulations with a multiple-relaxation-time LBE model. Int J Mod Phys B 2003;17:33–9.

[88] Yamazaki Y, Kaneda Y, Rubinsten R. Dynamics of inviscid truncated model of rotating turbulence. J Phys Soc Japan 2002;71:81–92.

[89] Bardina J, Ferziger JH. Effect of rotation on isotropic turbulence: computation and modelling. J Fluid Mech 1985;154:321–33.

[90] Higuera FJ, Jiménez J. Boltzmann approach to lattice gas simulations. Europhys Lett 1989;9:663–668.

[91] Eggels JGM. Direct and Large-eddy simulation of turbulent flow using the lattice-Boltzmann scheme. Int J Heat Fluid Flow 1996;17:307–23. Spinodal decomposition to a lamellar phase: effects of hydrodynamic flow. Phys Rev Lett 1996;78:1695-98.

[92] Somers JA. Direct simulation of fluid flow with cellular automata and the lattice-Boltzmann equation. Appl Sci Res 1993;51:127133.

[93] Derksen JJ, Van den Akker HEA. Large eddy simulations on the flow driven by a Rushton turbine. AIChE J 1999;45:209221.

[94] Lu Z, Liao Y, Qian D, McLauhlin JB, Derksen JJ, Kontomaris K. Large eddy simulations of a stirred tank using the lattice Boltzamnn method on a nonuniform grid. J Comp Phys 2002;181:675–704.

[95] Hartmann H, Derksen JJ, Montavon C, Pearson J, Hamill IS, Van den Akker HEA. Assessment of large eddy and RANS stirred tank simulations by means of LDA. Chem Eng Sci 2004;59:2419-2432.

[96] Ginzburg I, dHumi‘eres D. Multireflection boundary conditions for lattice Boltzmann models. Phys Rev E 2003;68:066614.

[97] Quinn WR, Militzer J. Experimental and numerical study of a turbulent free square jet. Phys Fluids 1988;31:1017-25.

[98] Gutmark EJ, Grinstein FF. Flow control with noncircular jets. Annu Rev Fluid Mech 1999;31:239–72.

[99] Sforza PM, Steiger MH, Trentacoste N. Studies on the three dimensional viscous jets. AIAA J 1966;4:800–6.

[100] Sforza PM. A quasi-axisymmetric approximation for turbulent three-dimensional jets and weaks. AIAA J 1969;7:1380–3.

[101] Masters GF, Fotheringham J. The influencee of aspect ratio on incompressible turbulent flows from rectangular slots. Aeron Quart 1980;31:285–305.

[102] Masters GF. Spanwise velocity distributions in jets from rectangular slots. AIAA J 1981;19:148–52.

[103] Sfeir AA. The velocity and temperature fields of rectangular jets. Int J Heat Mass Transf 1976;19:1289-97

[104] Sfeir AA. Investigation of three-dimensional turbulent rectangular jets. AIAA J 1979;17:1055-60.

[105] Trentacoste N, Sforza PM. Further experimental results for three-dimensional free jets. AIAA J 1967;5:885–90.

[106] Tsuchiya Y, Horikoshi C, Sato T. On the spread of rectangular jets. Exp Fluids 1986;4:197-204.

[107] Tsuchiya Y, Horikoshi C, Sato T, Takahashi M. A study on the spread of rectangular jets. JSME Int J 1989;32:11–8.

[108] Quinn WR. Passive near-field mixing enhancement in rectangular jet flows. AIAA J 1991;4:515-9.

[109] Quinn WR. Turbulent free jet flows issuing from sharp-edged rectangular slots: the influence of slot aspect-ratio. Exp Therm Fluid Sci 1992;5:203-15.

[110] Quinn WR. Development of a large-aspect-ratio rectangular turbulent free jet. AIAA J 1994;32:547–53.

[111] Quinn WR. Turbulent mixing in a free jet issuing from a low aspect ratio contoured rectangular nozzle. Aeronaut J 1995;No. 2110:337–42.

[112] Lozanova M, Stankov P. Experimental investigation on the similarity of a 3D rectangular turbulent jet. Exp Fluid 1998;24:470–8.

[113] Krothapalli A, Baganoff D, Karamcheti K. On the mixing of a rectangular jet. J Fluid Mech 1981;107:201–20.

[114] Brown G, Roshko A. On density effects and large structure in turbulent mixing layers. J Fluid Mech 1974;64:775–84.

[115] Van Der Hegge Zijen GB. Measurements of the velocity distribution in a plane turbulent jet of air. Appl Sci Res A 1958;7:256–92.

[116] Koshigoe S. Tubis A. Wave structures in jets of arbitrary shapes: I. Linear inviscid spatial stability analysis. Phys Fluids 1986;29:3982–91.

[117] Koshigoe S, Tubis A. Wave structures in jets of arbitrary shapes: II. Applications of a generalized shooting method to linear stability analysis. Phys Fluids 1987;30:1715–23.

[118] Tam CKW. The shock-cell structures and screech tone frequencies of rectangular and non-axisymmetric supersonic jets. J Sound Vib 1988;121:135-47.

[119] Tam CKW, Thiess AT. Instability of rectangular jets. J Fluid Mech 1993;248:425–48.

[120] Grinstein FF. Self-induced vortex ring dynamics in subsonic rectangular jets. Phys Fluids 1995;7:2519–21.

[121] Miller RS, Madnia CK, Givi P. Numerical simulation of non-circular jets. Comp Fluid 1995;24:1–25.

[122] Wilson RV, Demuren AO. Numerical simulation of turbulent jets with rectangular cross-section. J Fluids Eng 1998;120:285–290.

[123] Rembold B, Adams NA, Kleiser L. Direct numerical simulation of a transitional rectangular jet. Int J Heat Fluids flow 2002;23:547-53.

[124] Feiz H, Soo JH, Menon S. LES of turbulent jets using the lattice Boltzmann approach. 41st AIAA Aerospace Sciences Meeting. AIAA-03-0780. Reno, Nevada, 06-09 January, 2003.

[125] duPlessis MP, Wang RL, Kahawita R. Investigation of the near-region of a square jet. J Fluids Eng 1974;96:246–51.

[126] Rowlinson JS, Widom B. Molecular theory of capilarity, The international series of monographs on chemistry. Oxford: Clarendon; 1982.

[127] Callen HB. Thermodynamics and an introduction to thermostatistics (2nd ed). New York: Wiley; 1985.

[128] Bird RB, Stewart WE, Lightfoot EN. Transport phenomena. New York: Willey; 1960.

APPENDIX A

DERIVATION OF HYDRODYNAMIC EQUATIONS AND MUTUAL DIFFUSIVITY FOR BINARY SCALAR MIXING MODEL

In order to derive the corresponding hydrodynamic equations and mutual diffusivity for the binary scalar mixing model, we must rewrite the the lattice Boltzmann equation of the binary scalar mixing model in Chapter III as follows:

$$n_\alpha^\sigma(\vec{x}+\vec{e}_\alpha\delta t, t+\delta t) - n_\alpha^\sigma(\vec{x},t) = -\frac{1}{\tau^\sigma}[n_\alpha^\sigma(\vec{x},t) - n_\alpha^{\sigma(eq)}(\vec{x},t)] \tag{A.1}$$

Choose the equilibrium distribution functions to be

$$n_\alpha^{\sigma(eq)} = w_\alpha n^\sigma[1 + \frac{3(\vec{e}_\alpha\cdot\vec{u}^{\sigma(eq)})}{c^2} + \frac{9(\vec{e}_\alpha\cdot\vec{u}^{\sigma(eq)})^2}{2c^4} - \frac{3(u^{\sigma(eq)})^2}{2c^2}] \tag{A.2}$$

where $\vec{u}^{\sigma(eq)}$ is a parameter which will be determined later from the distribution functions of two species and the interaction between them. $c = \delta x/\delta t = 1$ in the lattice units.

The number density, mass density, velocity of the σ-species and the number density, the mass density, velocity of the mixture are calculated by

$$n^\sigma = \sum_\alpha n_\alpha^\sigma \tag{A.3}$$

$$\rho^\sigma = m^\sigma n^\sigma = m^\sigma \sum_\alpha n_\alpha^\sigma \tag{A.4}$$

$$\vec{u}^\sigma = \frac{1}{n^\sigma}\sum_\alpha n_\alpha^\sigma \vec{e}_\alpha \tag{A.5}$$

$$n = \sum_\sigma n^\sigma \tag{A.6}$$

$$\rho = \sum_\sigma \rho^\sigma \tag{A.7}$$

$$\vec{u} = \frac{1}{\rho}\sum_{\sigma}\rho^{\sigma}\vec{u}^{\sigma} \tag{A.8}$$

respectively.

When interaction is absent, both species are ideal gases. In this case, we assume that the velocities $\vec{u}^{\sigma(eq)}$ of two species are all equal a common velocity $\vec{u}'$. Since in this case the total momentum of particles of two species should be conserved by collision operator at each lattice site, it is quite straightforward from Eq. (A.1) to have

$$\vec{u}^{\sigma(eq)} = \vec{u}' = \frac{\sum_{\sigma}\rho^{\sigma}\vec{u}^{\sigma}/\tau^{\sigma}}{\sum_{\sigma}\rho^{\sigma}/\tau^{\sigma}}$$

in which $\rho^{\sigma}\vec{u}^{\sigma} = m^{\sigma}\sum_{\alpha} n_{\alpha}^{\sigma}\vec{e}_{\alpha}$ is species σ's momentum.

Introduce interaction force between two species characterized by interaction strength G_f

$$\vec{F}^{\sigma} = c_s^2 n G_f[\nabla\chi^{\sigma} + (\chi^{\sigma} - \omega^{\sigma})\frac{\nabla\rho}{\rho}] \tag{A.9}$$

with $\chi^{\sigma} = n^{\sigma}/n$ and $\omega^{\sigma} = \rho^{\sigma}/\rho$ respectively. This force causes an extra momentum change to species σ in addition to the momentum exchange caused by conventional collision. To incorporate this momentum change in the dynamics of the distribution functions, one can simply define

$$\rho^{\sigma}\vec{u}^{\sigma(eq)} = \rho^{\sigma}\vec{u}' + \tau^{\sigma}\vec{F}^{\sigma} \tag{A.10}$$

Thus, each species satisfies the mass conservation

$$\sum_{\alpha} n_{\alpha}^{\sigma}(\vec{x} + \vec{e}_{\alpha}, t+1) - \sum_{\alpha} n_{\alpha}^{\sigma}(\vec{x}, t) = 0 \tag{A.11}$$

and the mixture satisfies the momentum conservation

$$\begin{aligned}&\sum_{\sigma} m^{\sigma}\sum_{\alpha} n_{\alpha}^{\sigma}(\vec{x} + \vec{e}_{\alpha}, t+1) - \sum_{\sigma} m^{\sigma}\sum_{\alpha} n_{\alpha}^{\sigma}(\vec{x}, t)\\ &= \sum_{\sigma}\vec{F}^{\sigma} = 0\end{aligned} \tag{A.12}$$

Following the algorithm by Xianwen Shan and Gary Doolen [50, 51], we define the macroscopic velocity of the whole fluid $\vec{u}$ as the average of the momentum values of species σ before and after collision summed over two species as follows.

The momentum of species σ before collision

$$m^\sigma \sum_\alpha n_\alpha^\sigma \vec{e}_\alpha = m^\sigma n^\sigma \vec{u}^\sigma = \rho^\sigma \vec{u}^\sigma \tag{A.13}$$

while the momentum after collision

$$(1 - \frac{1}{\tau^\sigma}) m^\sigma \sum_\alpha n_\alpha^\sigma \vec{e}_\alpha + \frac{m^\sigma}{\tau^\sigma} \sum_\alpha n_\alpha^{\sigma(eq)} \vec{e}_\alpha = \rho^\sigma \vec{u}^\sigma - \frac{\rho^\sigma}{\tau^\sigma} \vec{u}^\sigma + \frac{m^\sigma}{\tau^\sigma} n^\sigma n^\sigma \vec{u}^{\sigma(eq)} \tag{A.14}$$

so that

$$\rho \vec{u} = \frac{1}{2} \sum_\sigma (\rho^\sigma \vec{u}^\sigma + \rho^\sigma \vec{u}^\sigma - \frac{\rho^\sigma}{\tau^\sigma} \vec{u}^\sigma + \frac{m^\sigma}{\tau^\sigma} n^\sigma n^\sigma \vec{u}^{\sigma(eq)}) = \rho^\sigma \vec{u}^\sigma + \frac{1}{2} \vec{F}^\sigma \tag{A.15}$$

by noticing Eq. (A.10).

We now follow the Chapman-Enskog technique of successive approximation [126, 127] to obtain the macroscopic fluid equations of the this model.

Expand the left-hand side of Eq. (A.1) in a Taylor series up to the 2nd order to get

$$(\partial_t + \vec{e}_\alpha \cdot \nabla) n_\alpha^\sigma + \frac{1}{2} (\partial_t + \vec{e}_\alpha \cdot \nabla)^2 n_\alpha^\sigma = - \frac{[n_\alpha^\sigma(\vec{x}, t) - (n_\alpha^{\sigma(eq)}(\vec{x}, t)]}{\tau^\sigma} \tag{A.16}$$

Introduce a small parameter ϵ(which is the Knudsen number), and expand

$$n_\alpha^\sigma = n_\alpha^{\sigma(0)} + \epsilon n_\alpha^{\sigma(1)} + \cdots, \quad \partial_t = \epsilon \partial_{t0} + \epsilon^2 \partial_{t1} + \cdots \tag{A.17}$$

and remember $\nabla \to \epsilon \nabla$. Since now the collision operator depends upon the spatial derivatives of particle number, we chose the leading order distribution functions to

be the equilibrium distribution about the fluid velocity $\vec{u}$, namely,

$$n_\alpha^{\sigma(0)} = w_\alpha n^{\sigma(0)}[1 + \frac{3(\vec{e}_\alpha \cdot \vec{u})}{c^2} + \frac{9(\vec{e}_\alpha \cdot \vec{u})^2}{2c^4} - \frac{3u^2}{2c^2}] \tag{A.18}$$

to obtain a set of macroscopic equations in terms of the correct fluid variables without changing the conservation relations. The lattice Boltzmann equation is then satisfied at the next order when terms that depend on spatial derivatives are included. Since

$$\sum_\alpha n_\alpha^{\sigma(0)} = n^\sigma, \quad \sum_\sigma m^\sigma \sum_\alpha n_\alpha^{\sigma(0)} \vec{e}_\alpha = \rho\vec{u} \tag{A.19}$$

we get

$$\sum_\alpha n_\alpha^{\sigma(1)} = n^\sigma, \quad \sum_\sigma m^\sigma \sum_\alpha n_\alpha^{\sigma(1)} \vec{e}_\alpha = -\frac{1}{2}\sum_\sigma \vec{F}^\sigma \tag{A.20}$$

Expanding the left-hand side of Eq. (A.16) by (A.17), we have

$n_\alpha^\sigma(\vec{x} + \vec{e}_\alpha, t+1) - n_\alpha^\sigma(\vec{x}, t)$

$$\simeq \epsilon[(\partial_{t0} + \vec{e}_\alpha \cdot \nabla) n_\alpha^{\sigma(0)}] + \epsilon^2[(\partial_{t0} + \vec{e}_\alpha \cdot \nabla) n_\alpha^{\sigma(1)} + \partial_{t1} n_\alpha^{\sigma(0)} + \frac{1}{2}(\partial_{t0} + \vec{e}_\alpha \cdot \nabla)^2 n_\alpha^{\sigma(0)}] \tag{A.21}$$

By substituting above equation into the conversation relations (A.11) and (A.12) and collecting the first order of ϵ, we obtain

$$\partial_{t0}\rho^\sigma + \nabla \cdot (\rho^\sigma \vec{u}) = 0, \quad \sigma = 1, 2 \tag{A.22}$$

$$\partial_{t0}(\rho\vec{u}) + c_s^2 \nabla\rho \vec{+} \nabla \cdot \rho\vec{u}\vec{u} = \sum_\sigma \vec{F}^\sigma \tag{A.23}$$

From Eq. (A.22), Eq. (A.23) can be written in the form

$$(\partial_{t0} + \vec{u} \cdot \nabla)\vec{u} = -\frac{1}{\rho}\nabla P \tag{A.24}$$

where p is the pressure given by

$$p = c_s^2 \rho + \sum_\sigma \vec{F}^\sigma \tag{A.25}$$

The terms of the 2nd order of ϵ in the expansion of the mass-conversation relation yield the following equation for each species

$$\partial_{t1}\rho^\sigma + m^\sigma \nabla \cdot \sum_\alpha n_\alpha^{\sigma(1)} \vec{e}_\alpha + \frac{m^\sigma}{2} \nabla \cdot (\partial_{t0} \sum_\alpha n_\alpha^{\sigma(0)} \vec{e}_\alpha + \nabla \cdot \sum_\alpha n_\alpha^{\sigma(0)} \vec{e}_\alpha \vec{e}_\alpha) = 0 \quad \text{(A.26)}$$

Noticing Eq. (A.22), we can evaluate the third term of Eq. (A.26)

$$m^\sigma (\partial_{t0} \sum_\alpha n_\alpha^{\sigma(0)} \vec{e}_\alpha + \nabla \cdot \sum_\alpha n_\alpha^{\sigma(0)} \vec{e}_\alpha \vec{e}_\alpha) = -\omega^\sigma \nabla p + c_s^2 \nabla \rho^\sigma \quad \text{(A.27)}$$

In order to calculate the 2nd term of Eq. (A.26), we substitute the expansions of Eqs. (A.17) into the lattice Boltzmann equation (A.1) and obtain

$$\partial_{t0} \sum_\alpha n_\alpha^{\sigma(0)} \vec{e}_\alpha + \nabla \cdot \sum_\alpha n_\alpha^{\sigma(0)} \vec{e}_\alpha \vec{e}_\alpha = -\frac{1}{\tau^\sigma} [\rho^\sigma (\vec{u} - \vec{u}') + \sum_\alpha m^\sigma n_\alpha^{\sigma(1)} \vec{e}_\alpha] + \vec{F}^\sigma \quad \text{(A.28)}$$

Multiplied by τ^σ and summed over all the components, above equation becomes

$$\rho(\vec{u} - \vec{u}') = \sum_\sigma \tau^\sigma \vec{F}^\sigma + \frac{1}{2} \sum_\sigma \vec{F}^\sigma + \sum_\sigma \tau^\sigma \omega^\sigma \nabla p - c_s^2 \sum_\sigma \tau^\sigma \nabla \rho^\sigma \quad \text{(A.29)}$$

$\sum_\alpha m^\sigma n_\alpha^{\sigma(1)} \vec{e}_\alpha$ in Eq. (A.28) can then be solved by substituting Eqs. (A.29) and (A.27) into Eq. (A.28). Combining Eq. (A.26) with the first order equation (A.22), we obtain the following equation at the second order

$$\frac{\partial \rho^\sigma}{\partial t} + \nabla \cdot (\rho^\sigma \vec{u}) = -\tau^\sigma \nabla \cdot \vec{F}^\sigma + (\tau^\sigma - \frac{1}{2}) \nabla \cdot [c_s^2 \nabla \rho^\sigma - \omega^\sigma \nabla p] + \nabla \cdot \omega^\sigma [\sum_k (\tau^k + \frac{1}{2}) \vec{F}^k$$

$$+ \nabla p \sum_k \tau^k \omega^k - c_s^2 \sum_k \tau^k \nabla \rho^k] \quad \text{(A.30)}$$

The continuity equation of the whole fluid at the 2nd order is obtained by summing over two species of the above equation

$$\frac{\partial \rho}{\partial t} + \nabla \cdot (\rho \vec{u}) = 0 \quad \text{(A.31)}$$

It is known that diffusion occurs among species when the velocities of the species differ. Mathematically, the diffusion of the constituents is described by a local velocity of the fluid mixture which is obtained by averaging the velocities of the constituents through mass, mole, or volume [128]. Here we use the mass fluxes of the species in our calculation following the treatment presented by Chapman and Cowling [26]. Again, we average mass fluxes before and after collisions to get the overall mass flux because of the momentum change of each species

$$\rho^\sigma \vec{u}^\sigma = \frac{m^\sigma}{2}[\sum_\alpha n_\alpha^\sigma \vec{e}_\alpha + (1 - \frac{1}{\tau^\sigma}) \sum_\alpha n_\alpha^\sigma \vec{e}_\alpha + \frac{1}{\tau^\sigma} \sum_\alpha n_\alpha^{\sigma(eq)} \vec{e}_\alpha] \tag{A.32}$$

By applying the same Chapman-Enskog technique above, after tedious but straightforward manipulations [50, 51], the relative mass flux of species σ is obtained

$$\rho^\sigma(\vec{u} - \vec{u}^\sigma) = -\tau^\sigma \vec{F}^\sigma + (\tau^\sigma - \frac{1}{2})[c_s^2 \nabla \rho^\sigma - \omega^\sigma \nabla p] + \omega^\sigma [\sum_k (\tau^k + \frac{1}{2}) \vec{F}^k$$

$$+ \nabla p \sum_k \tau^k \omega^k - c_s^2 \sum_k \tau^k \nabla \rho^k] \tag{A.33}$$

The relative velocity $\vec{u}^\sigma - \vec{u}$ on the left side of the above equation causes the motion of species σ. It is noted that the right-hand side terms of Eq. (A.30) are exactly what the divergence operator acts on in the right-hand side of above equation. Therefore, we can simply rewrite Eq. (A.30) as the continuity equation of species σ

$$\frac{\partial \rho^\sigma}{\partial t} + \nabla \cdot (\rho^\sigma \vec{u}^\sigma) = 0 \tag{A.34}$$

which demonstrates that each species satisfies its own continuity equation at 2nd order. Following the convention in the diffusion literature, we define the mass flux of species σ as $\vec{j}^\sigma = \rho^\sigma(\vec{u} - \vec{u}^\sigma)$. As a result, Eq. (A.30) can be simply expressed as

$$(\partial_t + \vec{u} \cdot \nabla)\rho^\sigma + \nabla \cdot \vec{u} = -\nabla \cdot \vec{j}^\sigma \tag{A.35}$$

By assuming the incompressibility of the fluid, i.e. $\nabla \cdot \vec{u} = 0$. Setting the same molecular mass ($m^\sigma = m$) and relaxation time ($\tau^\sigma = \tau$), we obtain the following advection-diffusion equation

$$(\partial_t + \vec{u} \cdot \nabla)\rho^\sigma = -\nabla \cdot c_s^2 \rho(\tau n G_f - \tau + \frac{1}{2})\nabla\chi^\sigma \tag{A.36}$$

The diffusion coefficient in the mixture is

$$D = -c_s^2 \rho(\tau n G_f - \tau + \frac{1}{2}) \tag{A.37}$$

APPENDIX B

PHYSICAL PARAMETERS USED IN THE REACTING FLOW SIMULATION

- Reaction coefficient $\kappa_{ov} = 9.9 \times 10^7 [m^3 \cdot mol^{-1} \cdot s^{-1}]$
- Universal gas constant $R = 8.315 [J \cdot mol^{-1} \cdot K^{-1}]$
- Effective activation energy $E = 30 [kcal \cdot mol^{-1}] = 1.26 \times 10^5 [J \cdot mol^{-1}]$
- Heat of overall reaction $Q = 2.05 \times 10^6 [J \cdot mol^{-1}]$
- Density of pre-mixed mixture $\rho = 1.2 [kg \cdot m^{-3}]$
- Heat capacity $c_p = 29.1 [J \cdot mol^{-1} \cdot K^{-1}] = 10^3 [J \cdot kg^{-1} \cdot K^{-1}]$
- Kinetic viscosity $\nu = 1.6 \times 10^{-5} [m^2 \cdot s^{-1}]$
- Thermal diffusivity $\kappa = 2.2 \times 10^{-5} [m^2 \cdot s^{-1}]$
- Diffusivity

$$D_{C_3H_8} = 1.1 \times 10^{-5} [m^2 \cdot s^{-1}], \quad D_{O_2} = 2.1 \times 10^{-5} [m^2 \cdot s^{-1}]$$
$$D_{CO_2} = 1.6 \times 10^{-5} [m^2 \cdot s^{-1}], \quad D_{H_2O} = 2.2 \times 10^{-5} [m^2 \cdot s^{-1}]$$

- Mass weight

$$M_{C_3H_8} = 4.4 \times 10^{-2} [kg/mol], \quad M_{O_2} = 3.2 \times 10^{-2} [kg/mol]$$
$$M_{CO_2} = 4.4 \times 10^{-2} [kg/mol], \quad M_{H_2O} = 1.8 \times 10^{-2} [kg/mol]$$

- Equivalent ratio

$$\phi = \frac{Y_{C_3H_8}/Y_{O_2}}{0.276} = 0.6$$

- Length of the 1-D channel $L = 16.7[mm]$
- Physical velocity $u_p = 1.0[m \cdot s^{-1}]$

APPENDIX C

STRAIN-RATE TENSOR OF D3Q19 MRT-LBE MODEL

In MRT-LBE, it is known that the strain rate tensor can be computed directly from the nonequilibrium moments. Following is a general derivation[a] of strain rate tensor in D3Q19 MRT-LBE model (not limited to LES) so that no any following quantity is filtered.

The MRT-LBE can be written as

$$|f(\vec{x}+\vec{e}_\alpha\delta t, t+\delta t)\rangle - |f(\vec{x},t)\rangle = -M^{-1}\hat{S}[|m(\vec{x},t)\rangle - |m^{(eq)}(\vec{x},t)\rangle] \tag{C.1}$$

Taylor expanding the first term on the left-hand side up to the first order in δt, the above equation becomes

$$\delta t D_t|f(\vec{x},t)\rangle = -M^{-1}\hat{S}[|m(\vec{x},t)\rangle - |m^{(eq)}(\vec{x},t)\rangle], \tag{C.2}$$

where

$$D_t = diag(\partial_t, \partial_t + \vec{e}_1\cdot\nabla, \ldots, \partial_t + \vec{e}_{18}\cdot\nabla).$$

Therefore,

$$|m(\vec{x},t)\rangle - |m^{(eq)}(\vec{x},t)\rangle = -\delta t\hat{\Lambda}MD_tM^{-1}|m(\vec{x},t)\rangle \tag{C.3}$$

where

$$\hat{\Lambda} = diag(0, \frac{1}{s_1}, \frac{1}{s_2}, 0, \frac{1}{s_4}, 0, \frac{1}{s_4}, 0, \frac{1}{s_4}, \frac{1}{s_9}, \frac{1}{s_2}, \frac{1}{s_9}, \frac{1}{s_2}, \frac{1}{s_9}, \frac{1}{s_9}, \frac{1}{s_9}, \frac{1}{s_{16}}, \frac{1}{s_{16}}, \frac{1}{s_{16}}).$$

Up to the first order in the Champman-Enskog expansion

$$|m(\vec{x},t)\rangle \simeq |m^{(0)}(\vec{x},t)\rangle + |m^{(1)}(\vec{x},t)\rangle$$

[a]Based on a private note from Dr. Li-Shi Luo.

and notice

$$|m^{(0)}(\vec{x},t)\rangle = |m^{(eq)}(\vec{x},t)\rangle$$

we have

$$|m^{(1)}(\vec{x},t)\rangle = -\delta t\hat{\Lambda}MD_tM^{-1}|m^{(0)}(\vec{x},t)\rangle \tag{C.4}$$

Neglect the nonlinear and other higher terms (in view of the Chapman-Enskog analysis) and get the following 12 non-zero non-equilibrium moments

$$m_1^{(1)} \simeq \frac{38(\partial_x j_x + \partial_y j_y + \partial_z j_z)}{3s_1}\delta t, \tag{C.5}$$

$$m_2^{(1)} \simeq \frac{(3\omega_\varepsilon + 2)(\partial_x j_x + \partial_y j_y + \partial_z j_z)}{3s_1}\delta t, \tag{C.6}$$

$$m_4^{(1)} \simeq \frac{42\partial_t j_x + (44 - 10\omega_\varepsilon)\partial_x \rho}{63s_4}\delta t, \tag{C.7}$$

$$m_6^{(1)} \simeq= \frac{42\partial_t j_y + (44 - 10\omega_\varepsilon)\partial_y \rho}{63s_4}\delta t, \tag{C.8}$$

$$m_8^{(1)} \simeq= \frac{42\partial_t j_z + (44 - 10\omega_\varepsilon)\partial_z \rho}{63s_4}\delta t, \tag{C.9}$$

$$m_9^{(1)} \simeq -\frac{4\partial_x j_x - 2\partial_y j_y - 2\partial_z j_z}{3s_9}\delta t, \tag{C.10}$$

$$m_{10}^{(1)} \simeq \frac{2\partial_x j_x - \partial_y j_y - \partial_z j_z}{3s_2}\delta t, \tag{C.11}$$

$$m_{11}^{(1)} \simeq -\frac{2\partial_y j_y - 2\partial_z j_z}{3s_9}\delta t, \tag{C.12}$$

$$m_{12}^{(1)} \simeq \frac{\partial_y j_y - \partial_z j_z}{3s_2}\delta t, \tag{C.13}$$

$$m_{13}^{(1)} \simeq -\frac{\partial_x j_y + \partial_y j_x}{3s_9}\delta t, \tag{C.14}$$

$$m_{14}^{(1)} \simeq -\frac{\partial_y j_z + \partial_z j_y}{3s_9}\delta t, \tag{C.15}$$

$$m_{15}^{(1)} \simeq -\frac{\partial_x j_z + \partial_z j_x}{3s_9}\delta t. \tag{C.16}$$

The 6 strain-rate tensor components $S_{ij} = (\partial_i u_j + \partial_j u_i)/2$ can be computed from Eqs. (C.5), (C.10), (C.12), and (C.14) – (C.16) straightforwardly as follows.

$$S_{xx} = -\frac{s_1 m_1^{(1)}}{38\rho_0 \delta t} - \frac{s_9 m_9^{(1)}}{2\rho_0 \delta t}, \tag{C.17}$$

$$S_{yy} = -\frac{s_1 m_1^{(1)}}{38\rho_0 \delta t} + \frac{s_9 m_9^{(1)}}{4\rho_0 \delta t} - \frac{3 s_9 m_{11}^{(1)}}{4\rho_0 \delta t}, \tag{C.18}$$

$$S_{zz} = -\frac{s_1 m_1^{(1)}}{38\rho_0 \delta t} + \frac{s_9 m_9^{(1)}}{4\rho_0 \delta t} + \frac{3 s_9 m_{11}^{(1)}}{4\rho_0 \delta t}, \tag{C.19}$$

$$S_{xy} = -\frac{3 s_9 m_{13}^{(1)}}{2\rho_0 \delta t}, \tag{C.20}$$

$$S_{yz} = -\frac{3 s_9 m_{14}^{(1)}}{2\rho_0 \delta t}, \tag{C.21}$$

$$S_{xz} = -\frac{3 s_9 m_{15}^{(1)}}{2\rho_0 \delta t}. \tag{C.22}$$

APPENDIX D

EFFICIENT IMPLEMENTATION OF COLLISION TERMS

Due to the transformation between the velocity space and the moment space each time step, the MRT-LBE model has apparently lower computational efficiency than the counterpart of the SRT-LBE model. Therefore, it's very important to apply optimization technique in coding the collision term. Following is the implementation tips of D3Q19 MRT-LBE model. The tips are subject to $\omega_\varepsilon = \omega_{xx} = 0$, $s_2 = s_{10}$, and $s_9 = s_{13}$ as reference [38] suggested.

(i) Avoid matrix calculation in the transformations between velocity space $\mathbb{V}$ and moment space $\mathbb{M}$.

Noticing the inverse transformation matrix M^{-1} and the diagonal collision matrix in Eq. (5.1) are both constant, the matrix multiplication $M^{-1}\hat{S}$ should be computed before the iteration as follows:

$$
\begin{bmatrix}
0 & c_1 & c_4 & 0 & 0 & 0 & 0 & 0 & 0 & 0 & 0 & 0 & 0 & 0 & 0 & 0 & 0 & 0 & 0 \\
0 & c_2 & c_5 & 0 & c_7 & 0 & 0 & 0 & 0 & c_9 & c_{10} & 0 & 0 & 0 & 0 & 0 & 0 & 0 & 0 \\
0 & c_2 & c_5 & 0 & c_7 & 0 & 0 & 0 & 0 & c_9 & -c_{10} & 0 & 0 & 0 & 0 & 0 & 0 & 0 & 0 \\
0 & -c_2 & -c_5 & 0 & 0 & 0 & -c_7 & 0 & 0 & -c_{11} & c_{12} & c_{13} & -c_{15} & 0 & 0 & 0 & 0 & 0 & 0 \\
0 & -c_2 & -c_5 & 0 & 0 & 0 & c_7 & 0 & 0 & -c_{11} & c_{12} & c_{13} & -c_{15} & 0 & 0 & 0 & 0 & 0 & 0 \\
0 & -c_2 & -c_5 & 0 & 0 & 0 & 0 & 0 & -c_7 & -c_{11} & c_{12} & -c_{13} & c_{15} & 0 & 0 & 0 & 0 & 0 & 0 \\
0 & -c_2 & -c_5 & 0 & 0 & 0 & 0 & 0 & c_7 & -c_{11} & c_{12} & -c_{13} & c_{15} & 0 & 0 & 0 & 0 & 0 & 0 \\
0 & c_3 & c_6 & 0 & c_8 & 0 & c_8 & 0 & 0 & c_{11} & c_{14} & c_{13} & c_{16} & c_{17} & 0 & 0 & c_{18} & -c_{18} & 0 \\
0 & c_3 & c_6 & 0 & -c_8 & 0 & c_8 & 0 & 0 & c_{11} & c_{14} & c_{13} & c_{16} & -c_{17} & 0 & 0 & -c_{18} & -c_{18} & 0 \\
0 & c_3 & c_6 & 0 & c_8 & 0 & -c_8 & 0 & 0 & c_{11} & c_{14} & c_{13} & c_{16} & -c_{17} & 0 & 0 & c_{18} & c_{18} & 0 \\
0 & c_3 & c_6 & 0 & -c_8 & 0 & -c_8 & 0 & 0 & c_{11} & c_{14} & c_{13} & c_{16} & c_{17} & 0 & 0 & -c_{18} & c_{18} & 0 \\
0 & c_3 & c_6 & 0 & c_8 & 0 & 0 & 0 & c_8 & c_{11} & c_{14} & -c_{13} & -c_{16} & 0 & 0 & c_{17} & -c_{18} & 0 & c_{18} \\
0 & c_3 & c_6 & 0 & -c_8 & 0 & 0 & 0 & c_8 & c_{11} & c_{14} & -c_{13} & -c_{16} & 0 & 0 & -c_{17} & c_{18} & 0 & c_{18} \\
0 & c_3 & c_6 & 0 & c_8 & 0 & 0 & 0 & -c_8 & c_{11} & c_{14} & -c_{13} & -c_{16} & 0 & 0 & -c_{17} & -c_{18} & 0 & -c_{18} \\
0 & c_3 & c_6 & 0 & -c_8 & 0 & 0 & 0 & -c_8 & c_{11} & c_{14} & -c_{13} & -c_{16} & 0 & 0 & c_{17} & c_{18} & 0 & -c_{18} \\
0 & c_3 & c_6 & 0 & 0 & 0 & c_8 & 0 & c_8 & -c_9 & -c_{12} & 0 & 0 & 0 & c_{17} & 0 & 0 & c_{18} & -c_{18} \\
0 & c_3 & c_6 & 0 & 0 & 0 & -c_8 & 0 & c_8 & -c_9 & -c_{12} & 0 & 0 & 0 & -c_{17} & 0 & 0 & -c_{18} & -c_{18} \\
0 & c_3 & c_6 & 0 & 0 & 0 & c_8 & 0 & -c_8 & -c_9 & -c_{12} & 0 & 0 & 0 & -c_{17} & 0 & 0 & c_{18} & c_{18} \\
0 & c_3 & c_6 & 0 & 0 & 0 & -c_8 & 0 & -c_8 & -c_9 & -c_{12} & 0 & 0 & 0 & c_{17} & 0 & 0 & -c_{18} & c_{18}.
\end{bmatrix}
$$

where

$$
\begin{aligned}
&c_1 \equiv \frac{5s_1}{399}, \quad c_2 \equiv \frac{11s_1}{2394}, \quad c_3 \equiv \frac{4s_1}{1197}, \quad c_4 \equiv \frac{s_2}{21}, \\
&c_5 \equiv \frac{s_2}{63}, \quad c_6 \equiv \frac{s_2}{252}, \quad c_7 \equiv \frac{s_4}{10}, \quad c_8 \equiv \frac{s_4}{40}, \\
&c_9 \equiv \frac{s_9}{18}, \quad c_{10} \equiv \frac{s_2}{18}, \qquad c_{11} \equiv \frac{s_9}{36}, \quad c_{12} \equiv \frac{s_2}{36},
\end{aligned}
$$

$$c_{13} \equiv \frac{s_9}{12}, \quad c_{14} \equiv \frac{s_2}{72}, \quad c_{15} \equiv \frac{s_2}{12}, \quad c_{16} \equiv \frac{s_2}{24},$$
$$c_{17} \equiv \frac{s_9}{4}, \quad c_{18} \equiv \frac{s_{16}}{8}.$$

(ii) Avoid using LOOP to reduce computation time since there are many null components in $\hat{S}$ and non-equilibrium moments.

Null terms are $s_0 = s_3 = s_5 = s_7 = 0$, $m_0^{(1)} = m_3^{(1)} = m_5^{(1)} = m_7^{(1)} = 0$, and $m_{10}^{(eq)} = m_{12}^{(eq)} = m_{16}^{(eq)} = m_{17}^{(eq)} = m_{18}^{(eq)} = 0$. Instead, express collision terms on a direction basis. Notice that in all c_is, $i = 1 - 18$, only those in Eq. (D.1) are updated each time step for LES and others should be pre-computed before iteration, notate $m_\alpha^{(1)} = m_\alpha - m_\alpha^{(eq)}$, the collision terms in Eq. (5.1) are computed as follows:

$$\begin{aligned}
\bar{\Omega}_0 &= c_1 m_1^{(1)} - c_4 m_2^{(1)}, \\
\bar{\Omega}_1 &= c_2 m_1^{(1)} + c_5 m_2^{(1)} + c_7 m_4^{(1)} - c_9 m_9^{(1)} + c_{10} m_{10}, \\
\bar{\Omega}_2 &= c_2 m_1^{(1)} + c_5 m_2^{(1)} - c_7 m_4^{(1)} - c_9 m_9^{(1)} + c_{10} m_{10}, \\
\bar{\Omega}_3 &= c_2 m_1^{(1)} + c_5 m_2^{(1)} + c_7 m_6^{(1)} + c_{11} m_9^{(1)} - c_{12} m_{10} - c_{13} m_{11}^{(1)} + c_{15} m_{12}, \\
\bar{\Omega}_4 &= c_2 m_1^{(1)} + c_5 m_2^{(1)} - c_7 m_6^{(1)} + c_{11} m_9^{(1)} - c_{12} m_{10} - c_{13} m_{11}^{(1)} + c_{15} m_{12}, \\
\bar{\Omega}_5 &= c_2 m_1^{(1)} + c_5 m_2^{(1)} + c_7 m_8^{(1)} + c_{11} m_9^{(1)} - c_{12} m_{10} + c_{13} m_{11}^{(1)} - c_{15} m_{12}, \\
\bar{\Omega}_6 &= c_2 m_1^{(1)} + c_5 m_2^{(1)} - c_7 m_8^{(1)} + c_{11} m_9^{(1)} - c_{12} m_{10} + c_{13} m_{11}^{(1)} - c_{15} m_{12}, \\
\bar{\Omega}_7 &= -c_3 m_1^{(1)} - c_6 m_2^{(1)} - c_8 m_4^{(1)} - c_8 m_6^{(1)} - c_{11} m_9^{(1)} - c_{14} m_{10} - c_{13} m_{11}^{(1)} \\
&\quad - c_{16} m_{12} - c_{17} m_{13}^{(1)} - c_{18} m_{16} + c_{18} m_{17}, \\
\bar{\Omega}_8 &= -c_3 m_1^{(1)} - c_6 m_2^{(1)} + c_8 m_4^{(1)} - c_8 m_6^{(1)} - c_{11} m_9^{(1)} - c_{14} m_{10} - c_{13} m_{11}^{(1)} \\
&\quad - c_{16} m_{12} + c_{17} m_{13}^{(1)} + c_{18} m_{16} + c_{18} m_{17}, \\
\bar{\Omega}_9 &= -c_3 m_1^{(1)} - c_6 m_2^{(1)} - c_8 m_4^{(1)} + c_8 m_6^{(1)} - c_{11} m_9^{(1)} - c_{14} m_{10} - c_{13} m_{11}^{(1)} \\
&\quad - c_{16} m_{12} + c_{17} m_{13}^{(1)} - c_{18} m_{16} - c_{18} m_{17}, \\
\bar{\Omega}_{10} &= -c_3 m_1^{(1)} - c_6 m_2^{(1)} + c_8 m_4^{(1)} + c_8 m_6^{(1)} - c_{11} m_9^{(1)} - c_{14} m_{10} - c_{13} m_{11}^{(1)}
\end{aligned}$$

$$
\begin{aligned}
& -c_{16}m_{12} - c_{17}m_{13}^{(1)} + c_{18}m_{16} - c_{18}m_{17}, \\
\bar{\Omega}_{11} &= -c_3 m_1^{(1)} - c_6 m_2^{(1)} - c_8 m_4^{(1)} - c_8 m_8^{(1)} - c_{11} m_9^{(1)} - c_{14} m_{10} + c_{13} m_{11}^{(1)} \\
& +c_{16}m_{12} - c_{17}m_{15}^{(1)} + c_{18}m_{16} - c_{18}m_{18}, \\
\bar{\Omega}_{12} &= -c_3 m_1^{(1)} - c_6 m_2^{(1)} + c_8 m_4^{(1)} - c_8 m_8^{(1)} - c_{11} m_9^{(1)} - c_{14} m_{10} + c_{13} m_{11}^{(1)} \\
& +c_{16}m_{12} + c_{17}m_{15}^{(1)} - c_{18}m_{16} - c_{18}m_{18}, \\
\bar{\Omega}_{13} &= -c_3 m_1^{(1)} - c_6 m_2^{(1)} - c_8 m_4^{(1)} + c_8 m_8^{(1)} - c_{11} m_9^{(1)} - c_{14} m_{10} + c_{13} m_{11}^{(1)} \\
& +c_{16}m_{12} + c_{17}m_{15}^{(1)} + c_{18}m_{16} + c_{18}m_{18}, \\
\bar{\Omega}_{14} &= -c_3 m_1^{(1)} - c_6 m_2^{(1)} + c_8 m_4^{(1)} + c_8 m_8^{(1)} - c_{11} m_9^{(1)} - c_{14} m_{10} + c_{13} m_{11}^{(1)} \\
& +c_{16}m_{12} - c_{17}m_{15}^{(1)} - c_{18}m_{16} + c_{18}m_{18}, \\
\bar{\Omega}_{15} &= -c_3 m_1^{(1)} - c_6 m_2^{(1)} - c_8 m_6^{(1)} - c_8 m_8^{(1)} + c_9 m_9^{(1)} + c_{12} m_{10} - c_{17} m_{(14)}^{(1)} \\
& -c_{18}m_{17} + c_{18}m_{18}, \\
\bar{\Omega}_{16} &= -c_3 m_1^{(1)} - c_6 m_2^{(1)} + c_8 m_6^{(1)} - c_8 m_8^{(1)} + c_9 m_9^{(1)} + c_{12} m_{10} + c_{17} m_{(14)}^{(1)} \\
& +c_{18}m_{17} + c_{18}m_{18}, \\
\bar{\Omega}_{17} &= -c_3 m_1^{(1)} - c_6 m_2^{(1)} - c_8 m_6^{(1)} + c_8 m_8^{(1)} + c_9 m_9^{(1)} + c_{12} m_{10} + c_{17} m_{(14)}^{(1)} \\
& -c_{18}m_{17} - c_{18}m_{18}, \\
\bar{\Omega}_{18} &= -c_3 m_1^{(1)} - c_6 m_2^{(1)} + c_8 m_6^{(1)} + c_8 m_8^{(1)} + c_9 m_9^{(1)} + c_{12} m_{10} - c_{17} m_{(14)}^{(1)} \\
& +c_{18}m_{17} - c_{18}m_{18}.
\end{aligned}
$$

Define

$$
\begin{aligned}
& a_1 \equiv c_1 m_1^{(1)}, \quad a_2 \equiv c_4 m_2^{(1)}, \quad a_3 \equiv c_2 m_1^{(1)}, \quad a_4 \equiv c_5 m_2^{(1)}, \\
& a_5 \equiv c_7 m_4^{(1)}, \quad a_6 \equiv c_9 m_9^{(1)}, \quad a_7 \equiv c_7 m_6^{(1)}, \quad a_8 \equiv c_{11} m_9^{(1)}, \\
& a_9 \equiv c_{10} m_{10}, \quad a_{10} \equiv c_{12} m_{10}, \quad a_{11} \equiv c_{13} m_{11}^{(1)}, \quad a_{12} \equiv c_{15} m_{12},
\end{aligned}
$$

$$a_{13} \equiv c_3 m_1^{(1)}, \quad a_{14} \equiv c_6 m_2^{(1)}, \quad a_{15} \equiv c_7 m_8^{(1)}, \quad a_{16} \equiv c_8 m_4^{(1)},$$
$$a_{17} \equiv c_8 m_6^{(1)}, \quad a_{18} \equiv c_{14} m_{10}, \quad a_{19} \equiv c_{16} m_{12}, \quad a_{20} \equiv c_{17} m_{13}^{(1)},$$
$$a_{21} \equiv c_{18} m_{16}, \quad a_{22} \equiv c_{18} m_{17}, \quad a_{23} \equiv c_8 m_8^{(1)}, \quad a_{24} \equiv c_{17} m_{15}^{(1)},$$
$$a_{25} \equiv c_{18} m_{18}, \quad a_{26} \equiv c_{17} m_{14}^{(1)},$$

above collision term expression can be further simplified as

$$\begin{aligned}
\bar{\Omega}_0 &= a_1 - a_2, \\
\bar{\Omega}_1 &= a_3 + a_4 + a_5 - a_6 + a_9, \\
\bar{\Omega}_2 &= a_3 + a_4 - a_5 - a_6 + a_9, \\
\bar{\Omega}_3 &= a_3 + a_4 + a_7 + a_8 - a_{10} - a_{11} + a_{12}, \\
\bar{\Omega}_4 &= a_3 + a_4 - a_7 + a_8 - a_{10} - a_{11} + a_{12}, \\
\bar{\Omega}_5 &= a_3 + a_4 + a_{15} + a_8 - a_{10} + a_{11} - a_{12}, \\
\bar{\Omega}_6 &= a_3 + a_4 - a_{15} + a_8 - a_{10} + a_{11} - a_{12}, \\
\bar{\Omega}_7 &= -a_{13} - a_{14} - a_{16} - a_{17} - a_8 - a_{18} - a_{11} - a_{19} - a_{20} - a_{21} + a_{22}, \\
\bar{\Omega}_8 &= -a_{13} - a_{14} + a_{16} - a_{17} - a_8 - a_{18} - a_{11} - a_{19} + a_{20} + a_{21} + a_{22}, \\
\bar{\Omega}_9 &= -a_{13} - a_{14} - a_{16} + a_{17} - a_8 - a_{18} - a_{11} - a_{19} + a_{20} - a_{21} - a_{22}, \\
\bar{\Omega}_{10} &= -a_{13} - a_{14} + a_{16} + a_{17} - a_8 - a_{18} - a_{11} - a_{19} - a_{20} + a_{21} - a_{22}, \\
\bar{\Omega}_{11} &= -a_{13} - a_{14} - a_{16} - a_{23} - a_8 - a_{18} + a_{11} + a_{19} - a_{24} + a_{21} - a_{25}, \\
\bar{\Omega}_{12} &= -a_{13} - a_{14} + a_{16} - a_{23} - a_8 - a_{18} + a_{11} + a_{19} + a_{24} - a_{21} - a_{25}, \\
\bar{\Omega}_{13} &= -a_{13} - a_{14} - a_{16} + a_{23} - a_8 - a_{18} + a_{11} + a_{19} + a_{24} + a_{21} + a_{25}, \\
\bar{\Omega}_{14} &= -a_{13} - a_{14} + a_{16} + a_{23} - a_8 - a_{18} + a_{11} + a_{19} - a_{24} - a_{21} + a_{25}, \\
\bar{\Omega}_{15} &= -a_{13} - a_{14} - a_{17} - a_{23} + a_6 + a_{10} - a_{26} - a_{22} + a_{25}, \\
\bar{\Omega}_{16} &= -a_{13} - a_{14} + a_{17} - a_{23} + a_6 + a_{10} + a_{26} + a_{22} + a_{25},
\end{aligned}$$

$$\bar{\Omega}_{17} = -a_{13} - a_{14} - a_{17} + a_{23} + a_6 + a_{10} + a_{26} - a_{22} - a_{25},$$

$$\bar{\Omega}_{18} = -a_{13} - a_{14} + a_{17} + a_{23} + a_6 + a_{10} - a_{26} + a_{22} - a_{25}.$$

VITA

Huidan Yu
Aerospace Engineering Department, Texas A&M University,
College Station, TX 77840–3141
Tel: 9798457541 Fax: 9798456051(h)

EDUCATION

Ph.D. Aerospace Engineering, Texas A&M University, USA, December 2004
Ph.D. Physics, Peking University, China, July 2001
B.S. Physics, Zhejiang Normal University, China, July 1984

EMPLOYMENT

Research Assistant
Texas A&M University, Sep 2001 - Dec. 2004
Postdoctoral Research Associate
Texas A&M University, Apr 2001 - Sep 2001
Research Assistant
The Pennsylvania State University, Jan 2000 - Apr 2001
Lecturer, Instructor, Associate Professor, Professor
Zhejiang Normal University, China, July 1984 - Jan. 2002

SELECTED PUBLICATIONS

1. Yu H, Luo LS, Girimaji SS. Scalar mixing and reaction simulations using lattice Boltzmann method. Inter J Comput Eng Sci 2002;156:73–87.

2. Yu H, Zhao K. Rossby vortex simulation on paraboloidal coordinate system using lattice Boltzmann method. Phys Rev E 2001;64:056703.

3. Yu H, Zhao K. Lattice Boltzmann method for compressible flows with high Mach number. Phy Rev E 2000;61:3867.

4. Yu H, Han Z. Numerical simulation of two-dimensional viscous fingering by the conformal mapping method, Phys Rev E 1998;58:6873.

5. Zhao K, Yu H. Nonsingular Saffman-Taylor finger. Comm Non Sci Num Sim 1997;5;28.

6. Yu H. Similarities reductions of the 2+1 dimensional high degree CDGSK equation. Comm Non Sci Num Sim 1996;1:28.

7. Yu H, Zhang J. Similarity solutions of the super KdV equation. Appl Math Mech 1995;16:901.

8. Yu H, Zhang J, Xv Y. Nother's theory for non-holonomic dynamic systems relative to non-inertial reference. Appl Math Mech 1993;14:527.